Summer 2019

The Role of the Southern Ocean on Global Ocean Circulation and Climate

Brady Scott Ferster

THE ROLE OF THE SOUTHERN OCEAN ON GLOBAL OCEAN CIRCULATION AND CLIMATE

by

Brady Scott Ferster

Bachelor of Science
Pennsylvania State University, 2016

Submitted in Partial Fulfillment of the Requirements

For the Degree of Doctor of Philosophy in

Marine Science

College of Arts and Sciences

University of South Carolina

2019

Accepted by:

Subrahmanyam Bulusu, Major Professor

Venkat Lakshmi, Committee Member

Alexander Yankovsky, Committee Member

Anthony Arguez, Committee Member

Cheryl L. Addy, Vice Provost and Dean of the Graduate School

DEDICATION

This dissertation is dedicated in memory of Robert Ferster for all of the monetary backing throughout my academic career as well as my mother, father, sister, and brother for all of their emotional and intellectual support throughout this academic and personal journey.

ACKNOWLEDGEMENTS

This project was supported in part by the NASA South Carolina Space Grant Graduate Research Assistantship. This work would not have been possible without the extensive help from many people. My sincerest gratitude is extended to my major professor, Prof. Subrahmanyam Bulusu, whose patience, guidance, and generosity helped deliver me through this demanding academic path. I would like to thank my respected committee members: Prof. Venkat Lakshmi, Dr. Alexander Yankovsky, and Dr. Anthony Arguez who significantly contributed in the guidance and construction of this dissertation. A special thanks goes to Dr. Ebenezer Nyadjro and Dr. Joseph D'Addezio whom helped get me started and adjusted to the doctoral program. I would also like to thank Dr. Alison Macdonald, Dr. Ichiro Fukumori, Dr. Ebenezer Nyadjro, and Dr. Anthony Arguez for their significant contributions towards chapters of this dissertation.

ABSTRACT

The Southern Ocean (SO) is a unique and highly dynamic region with strong temperature and salinity gradients. A comparison between satellite-derived salinity and observations indicates strong differences along coastal boundaries, areas of low temperature, and regions of strong currents. Although differences throughout much of the SO are shown to be negligible, resolution and smoothing in the products create large biases in horizontal gradients and errors in estimating the water cycle. The three-dimensional movement of water within the SO plays an important role in the global Meridional Overturning Circulation (MOC), where the Southern Hemisphere westerlies drive both zonal and meridional transports and strong vertical movements of local water masses. Using the Estimating the Circulation and Climate of the Ocean (ECCO) estimates of ocean circulation, recent trends in the lower cell of the MOC (1992-2015) show increased overturning within the South Atlantic and decreased overturning within the Indian and Pacific basins, increasing the net SO heat transports and storage.

The path of the Antarctic Circumpolar Current (ACC) is mainly dictated by bathymetry, but recent variability indicates a northward shift in the central South Pacific ACC fronts. The movement and location of the ACC is highly correlated to salinity and temperature shifts up to 100 m depth and moderately correlated to depths of 1000 m. The location of the ACC is weakly-to-moderately correlated with the Antarctic and Southern Oscillations. These large-scale teleconnections are further driving surface cooling in the

central South Pacific and warming in the subtropics and mid-latitudes of the Southern Hemisphere. Satellite-derived sea surface temperatures (SSTs) are highly correlated with both the Antarctic and Southern Oscillations during 1982-2016, particularly during the austral summer months when the oscillations tend to be the strongest. Changes in the westerlies are correlated with sea level and heat content anomalies and anti-correlated to SST in the high latitudes. The magnitude of the westerlies has recently increased throughout the ACC region, driving the increase in mid-latitude and decrease in the central South Pacific SST, heat content, and sea level anomalies. These analyses conclude that atmospheric variability is significantly contributing to recent changes in circulation and surface properties.

TABLE OF CONTENTS

LIST OF TABLES

LIST OF FIGURES

CHAPTER 1

INTRODUCTION

Ocean-atmosphere interactions in the Southern Hemisphere drive high energy dynamics and strong seasonality. Differences in the surface radiative budget throughout the Southern Ocean (SO) are enhanced through these ocean and atmospheric dynamics, with a large portion of the energy being redistributed by the surface ocean currents and upwelling waters. The SO also importantly regulates the Earth's climate. The upwelling of deep waters and the formation of bottom waters directly influences the transports of heat, moisture, and gases around the globe. As the waters come in contact with the surface or sink, the exchange of carbon dioxide and oxygen are fundamental not only to the localized biological activity, but additionally to humans. The SO is a large sink of carbon dioxide, particularly in storing anthropogenic-sourced carbon from the atmosphere (Sabine et al., 2004).

The SO has two key components contributing to global ocean circulation: the Antarctic Circumpolar Current (ACC) and the meridional overturning circulations. The ACC is an eastward flowing pattern of narrow fronts and jets, perturbing strong eddy fluxes (Figure 1.1). Orsi et al. (1995) identified three fronts of the ACC: the Subantarctic Front (SAF), Polar Front (PF), and the southern ACC front. Each of the three fronts coincides with different water mass boundaries and maximum velocities. On shorter timescales (< 1 year) the ACC variability is largely driven through the westerlies, while on longer

timescales (> 1 year) the variability is thought to be restored by eddy saturation, or rather "eddy compensation" (Hallberg and Gnanadesikan, 2001; Meredith and Hogg, 2006; Hogg et al., 2015). Although a complete theory on eddy saturation is yet to be established, long-term increase in the westerlies would increase baroclinic instability and therefore be insensitive to changes due to the resulting eddies. As a result, the effort to monitor the ACC has increased over the past several decades through current meter moorings and inverse methods. The zonal flow of the ACC is largely uninterrupted by land barriers, connecting the Atlantic, Indian, and Pacific Ocean basins, which typically serve as boundaries to monitor the ACC. Places like the Drake Passage, a bottleneck boundary between the Pacific and Atlantic basins, serve as a key location to monitor the zonal transports of the ACC through both increased shipboard and mooring measurements of the region.

The SO additionally consists of double-celled overturning circulations (Figure 1.2), fundamental to the global scale Meridional Overturning Circulation (MOC). The strong eastward geostrophic component of the ACC is further associated with the steep sloping isopycnals, driving the upwelling of different density surfaces (i.e. water masses) to the surface. These different water masses are typically referred to as the Circumpolar Deep Waters (CDW) and are separated at the southern-most location of the PF into the Upper Circumpolar Deep Water (UCDW) and Lower Circumpolar Deep Water (LCDW). The upper cell of the SO overturning circulation consists of the northward flowing Antarctic Intermediate Water (AAIW) and Subantarctic Mode Water (SAMW) and southward flowing UCDW. The lower cell contains the poleward flowing LCDW and North Atlantic Deep Waters (NADW) and the equatorward transports of the Antarctic Bottom Water (AABW). The cells of the overturning circulation are important not only for the storage of

energy and carbon dioxide and storage of oxygen, but also replenish the nutrients and organic carbon available for biological activity within the surface waters.

The fronts of the ACC separate waters of different densities, and therefore can have sharp gradients along the jets and eddies. However, the vast majority of the SO has a relatively small horizontal salinity gradient; that is, much of the SO is thought to have small salinity variability spatially outside of the ACC. Due to the lack of consistent spatial and temporal sampling in the SO, largely in part due to the harsh austral winter conditions, a true time-mean estimate of surface salinity and the salinity gradients globally have large uncertainty (Levitus et al., 1994; Johnson et al., 2002). Since the start of the 21st century, the global sampling effort has significantly increased, particularly with the effort of Argo floats, but is still currently under-sampled in a vast majority of the high latitude SO (Lyman and Johnson, 2008; Lyman and Johnson 2014). Therefore, satellite-derived salinity is of utmost importance to the scientific community, offering high spatial and temporal coverage of sea surface salinity (SSS) since 2010. Despite the increased presence of remotely sensed SSS, few analyses compare the various salinity missions amongst the other products as well as to observational data. In an effort to support the continued need for satellite-derived salinity and observational data, the SSS products need to be compared in these high latitude regions to display the differences in products and the seasonal variability of SSS.

The ACC fronts are not only important for monitoring salinity and water mass properties at the surface, but also play a role in the SO overturning circulation. The ACC is where the CDW upwell to the surface and separates the two overturning cells. Due to the lack of observational data, there are few variability and time-mean estimates of the SO MOC outside of state-estimate and inverse methods. In Mazloff et al. (2010), the SO

overturning circulation is approximated to be 17 ± 12 Sv (Sv = 106 m3 s-1) in the upper cell and 13 ± 6 Sv in the lower cell at 32 °S. Zonal transports of the ACC are additionally difficult to estimate from pure observations outside of the bottleneck points. Estimates at the Drake Passage indicate mean zonal transports between 120-155 Sv (Macdonald and Wunsch, 1996; Ganachaud and Wunsch, 2000; Mazloff et al., 2010; etc.). Most of these studies, however, lack the temporal resolution to estimate the true variability and a time-mean of one decade. These zonal and meridional transports are essential in helping regulate the Earth's climate, distributing heat and nutrients from the mid-latitudes to the surface of the SO and zonally between the three basins.

Albeit important to circulation and climate studies, identifying the location of the ACC fronts have proved difficult, even with the efforts of satellites. The ACC is made of strong eddies and jets, constantly fluctuating on spatial scales of tens–to–thousands of meters. On longer timescales, the ACC fronts are insensitive to changes in the strength of the westerlies and the frequency of the Antarctic Oscillation (AAO) driven through the baroclinic instability. The insensitivity of the ACC strength and sloping isopycnals have been shown in both model (Meredith and Hogg, 2006; Meredith et al., 2012; Farneti et al., 2015) and observational (Böning et al., 2008; Hogg et al., 2015) analyses. The non-linear insensitivity on longer timescales of volume transports and the westerlies further motivate the need to increase observations and better understand the variability of heat and salt transports on longer timescales. The tilted isopycnals bring mid-waters to the surface along the ACC. Changes in the position of the ACC are largely understood to be driving mid-depth warming (Gille, 2002; Gille, 2008) and freshening (Durack and Wijffels, 2010) in the high latitudes of the SH (Figure 1.3). Monitoring the heat, salt, and freshwater fluxes

of the SO have potential major implications for global circulation and climate, as the SO works to distribute mass and heat through the oceans. Changes in the location of upwelling waters could therefore impact global circulation and climate.

Southern Hemisphere atmospheric variability is strongly influenced through large-scale, low-frequency patterns, which play a fundamental role in the weather and climate (Turner, 2004; Hendon et al., 2006; Hendon et al., 2014). Two main patterns of atmospheric variability that influence the SO are the AAO and the Southern Oscillation. These large-scale patterns are seen to influence yearly variability in surface circulation (Hall and Visbeck, 2002; Sen Gupta and England, 2006) and carbon uptake (Lovenduski and Gruber, 2005; Lenton and Matear, 2007; Waugh et al., 2013). Moreover, both oscillations have strong influences on sea surface temperature (SST), sea-ice, and atmospheric temperatures along Antarctica (Mo, 2000; Fogt and Bromwich, 2006; Welhouse et al., 2016; Cerrone et al., 2017). Fogt and Bromwich (2006) describe the strengthened influence of the AAO and Southern Oscillation during in phase periods, indicating a strong relationship between the atmospheric circulation and related ocean dynamics. Although these oscillations are understood to be driving the variability in SST, analyses either use the spatio-temporal sparse observational data over a short time or a model, and have not yet fully been explored using the approximate 35-years' worth of satellite-derived SST values.

The long temporal timescales of the satellite-derived products are not only ideal for investigating the effects of teleconnections, but can be used to analyze the trends and interannual variability. Beyond SSS and SST, there have also been significant changes observed through both remotely-sensed and observational data in ocean heat content

(OHC) (Willis et al., 2004; Roemmich et al., 2015), mean sea level (Rye et al., 2014), and sea ice extent (Purich et al., 2016; Kwok et al., 2016). As the westerlies are thought to be intensifying and shifting poleward, an investigation of the surface winds, sea level anomalies (SLA), SST, and OHC allows for an in–depth examination on the current state of the SO climate and circulation. With over 25-years' worth of SLA, SST, and surface winds and nearly a decade of consistent gravity anomalies, a thorough investigation into changes in the storage of heat and mass within the SO. Each surface winds, SLA, SST, and OHC can be used for the first time to explore the ocean variability and analyze the amount responsible due to changes in the surface winds. As a result, regional–scale changes in winds could influence the thermodynamic and dynamic forcings to the SO.

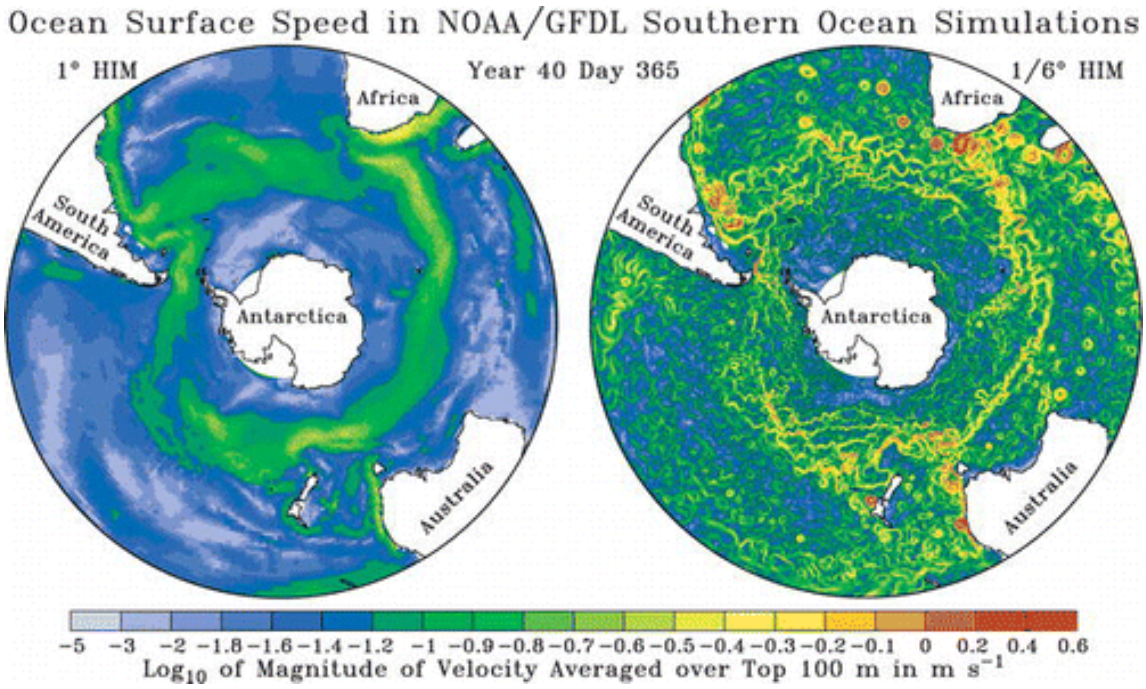

Figure 1.1. The instantaneous surface current speed after 40 years in 1° and 1/6° resolution models. (Taken from Hallberg and Gnanadesikan, 2001).

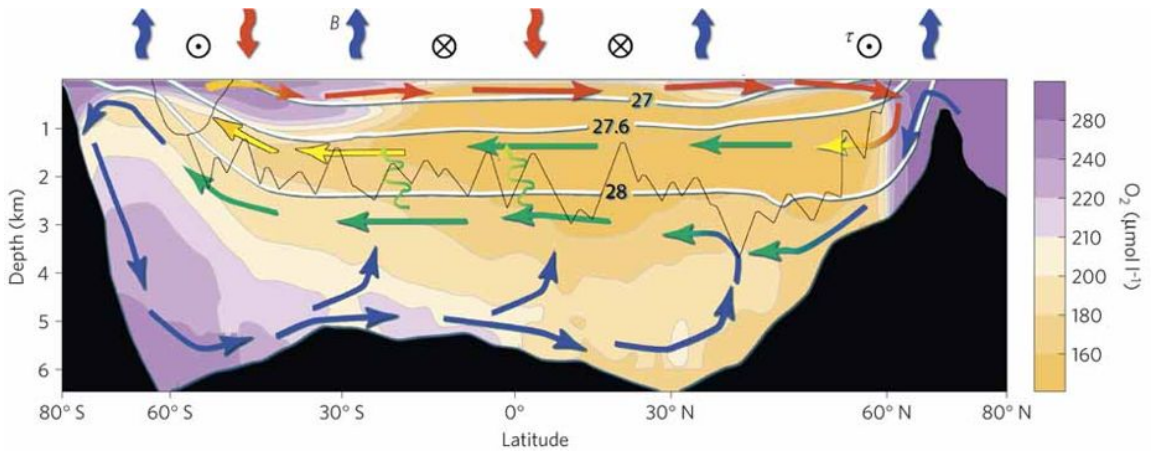

Figure 1.2: Zonally averaged oxygen distribution. Old waters are depicted through low oxygen (yellow) and ventilated waters are high concentrations (purple). The neutral density surface 27.6 kg m^{-3} divides the two overturning cells. The colored arrows indicate the different water masses: mode and intermediate waters (red), upper deep waters (yellow), lower deep waters (green), and bottom waters (blue). Additionally, air–sea heat exchange (red or blue) patterns are shown and zonal surface wind stress (⊙: eastward). (Taken from Marshall and Speer, 2012).

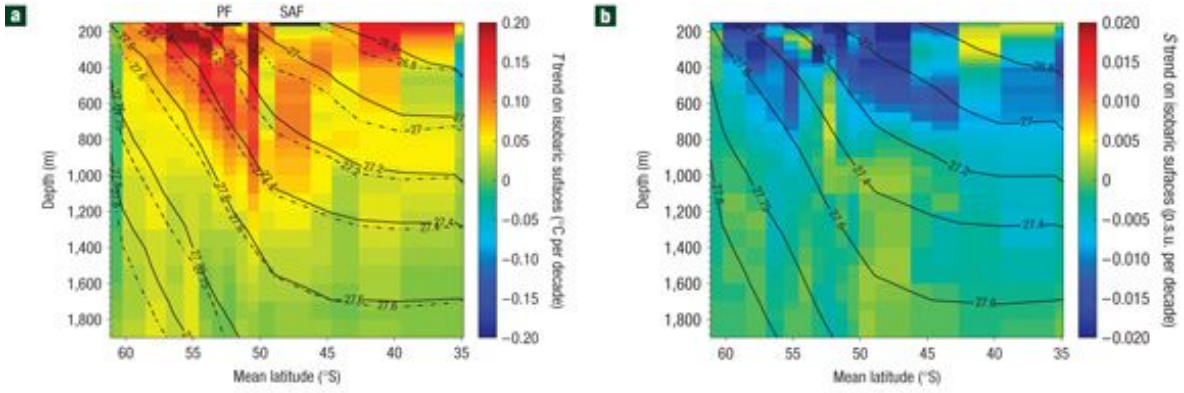

Figure 1.3: Zonally averaged changes in temperature (a) and salinity (b) across the ACC averaged on isobaric surfaces. Black contours are the mean climatological isopycnal surfaces and the dashed contours are the change over two decades. (Adopted from Böning et al., 2008).

CHAPTER 2

A COMPARISON OF SATELLITE-DERIVED SEA SURFACE SALINITY AND SALT FLUXES IN THE SOUTHERN OCEAN[1]

[1]Ferster, B. S. and B. Subrahmanyam (2018). A Comparison of Satellite-derived Sea Surface Salinity and Salt Fluxes in the Southern Ocean, J. Remote Sensing in Earth Systems Sciences; doi:10.1007/s41976-018-0001-5.

Abstract

Sea surface salinity (SSS) derived from the multi–satellite missions, NASA's Aquarius/SAC–D and Soil Moisture Active and Passive (SMAP), and ESA's Soil Moisture and Ocean Salinity (SMOS) are compared and used to estimate horizontal advective salt fluxes in the Southern Ocean (SO). In comparison with an Argo product, all three satellites estimate similar SSS in the Southern Hemisphere mid–latitudes (30°S–45°S) with low variability among the products. At high latitudes, there are temporal patterns of bias (relative to Argo) in Aquarius during Austral summer and in SMOS during Austral winter. Differences in the satellite products and Argo exist along coastal boundaries, low temperatures, and strong currents. Satellite–derived salinity indicates low temporal–mean standard deviations with Aquarius (0.215) and moderate standard deviations with SMOS (0.294) and SMAP (0.325) against Argo in the SO. Differences in satellite–derived zonal and meridional SSS gradients are large, standard deviation values are 2.52 and 1.49 $x10^{-6}$ psu m^{-1} respectively, and similarly located within the sub-tropical salinity maxima, Antarctic Circumpolar Current, and coastal zones. Differences in the horizontal advective fluxes are on average small, but large variability greater than 275 mm $month^{-1}$ indicates errors of similar magnitude to the estimated Argo flux. Based on these results, the use of satellite–derived salinity may prove to be a useful resource for observing salinity and horizontal salt fluxes, outside the inaccuracies associated with the high latitudes and coastal currents between the various remotely sensed products, and could significantly influence the results depending on the product.

2.1. Introduction

Salinity is an essential variable used to quantify density and the state of the ocean. Monitoring the Southern Ocean (SO) salinity is important due to its strong influence on density stratification, ocean circulation, water cycle, and biological productivity (Toggweiler and Samuels 1995; Sarmiento et al. 1998; Gille 2002; McNeil and Matear 2008; Dong et al. 2008; Montes–Hugo et al. 2009; Liu and Curry 2010). The SO is heavily influenced by the Southern Hemisphere Westerlies and the Antarctic Circumpolar Current (ACC), driving exchange between the Atlantic, Pacific, and Indian Ocean basins. As a result, the SO is dominated by zonal advective (geostrophic transport) processes and diffusive (Ekman transport) properties in the meridional component. Strong eddies interact within the SO on the spatial scales of tens–to–thousands of meters, driving regional changes in surface mixed layer and deep water formation (Rintoul and Naveira Garabato 2013; Sheen et al. 2014; Meyer et al. 2015).

The introduction of the Argo float program significantly increased and improved the sampling of the SO (Lyman and Johnson 2008). There are currently over 3800 active Argo floats throughout the global ocean, although still lacking extensive spatial coverage in the SO compared to other regions, typically covering a 3º x 3º area. This limitation of spatial resolution alone acts as a basis for the need to use satellite–derived salinity in monitoring the SO. Current projects, such as the Southern Ocean Carbon and Climate Observations and Modeling (SOCCOM) (https://soccom.princeton.edu/), have goals of increasing the number of floats within the SO, to account for the limited spatial and temporal coverage. Argo floats (and most in–situ profilers) generally quantify surface measurements at a depth of 5–10 m (bulk surface measurement) compared to the surface

1–2 cm (skin) of satellite–derived estimates. Moon and Song (2014) and Song et al. (2015) discuss differences between bulk and skin measurements that exist in regions of high stratification and describe the skin layer as having higher seasonal variability than bulk measurements. Despite measuring at different depths, differences have been shown to be marginal outside the tropics (Henocq et al., 2010; Boutin et al., 2013; Drucker and Riser, 2014; Boutin et al., 2016).

Satellite–derived salinity estimations in the SO are heavily influenced by the strong winds and low sea surface temperatures of the high latitude Southern Hemisphere (Reul et al. 2012; Dinnat et al. 2014; Yin et al. 2014; Le Vine et al. 2015). Despite the potential inaccuracies of satellites and differences within the satellite salinity products, the increased temporal and spatial scales and measuring the top few centimeters of the ocean surface have made satellite–derived salinity a useful quantity for air–sea interaction studies. In recent years, satellite–derived salinity has been incorporated with the balance of evaporation (E) and precipitation (P), documenting the strong relationship between the ocean water cycle and near surface salinity (Johnson et al. 2002; Yu 2011). Johnson et al. (2002) compared the salinity advection to atmospheric freshwater forcing using in–situ and climatology products, but only for the tropical Pacific region. Both (Johnson et al. 2002; Yu 2011) stressed the importance of surface salinity estimates for ocean processes, hydrological forcing, and model simulations.

Satellite–derived sea surface salinity (SSS) data have recently been used to improve seasonal climate predictions and ocean state estimates (Köhl et al. 2014; Vinogradova et al. 2014; Toyoda et al. 2015; Hackert et al. 2014; Fukumori et al. 2017). As SSS begins to be incorporated into such forecasts, re–analyses, or state estimates, the accuracy and

precision of salinity has become more significant. Satellite–derived salinity plays an important role in the spatial and temporal scales in monitoring salinity and salt fluxes in the global circulation, and developing the need to compare satellite–derived products in the SO. In the recent state estimate of ECCO version 4 run 3, the use of Aquarius has been incorporated between 2011 and 2013, although limiting the use of high latitude data (Fukumori et al. 2017). Furthermore, Vinogradova et al. (2014) compared satellite–derived salinity to both in–situ synthesized and model data globally. However, more recent versions of the satellite products have been released since their comparison.

The SO is known to have limited observations in an eddy–dominated system; therefore, the objective of this paper is to statistically compare the satellite–derived salinity with an in–situ Argo product. Through comparing SSS, the goal of this analysis is to emphasize the significance of finite differences in SSS as well as the influence on horizontal advective flux estimations with the most current versions of satellite–derived SSS. Advective fluxes are important to balance the hydrological cycle (Johnson et al. 2002), and are directly related to the salinity gradient and surface current velocity. We hypothesize that satellite–derived level 3 (L3) monthly salinity can confidently be used at similar spatial and temporal resolutions to that of in–situ data collected for the SO, with expected accuracy below the 0.2 psu standard set by the NASA missions, although originally set for the low–latitudes. We further anticipate to find small differences in the satellite–derived products and SSS gradients. Potential implications of this analysis are to enable effective utilization of satellite–derived SSS within model and reanalysis–based products to obtain a more accurate representation of the ocean state.

To test the hypothesis, a comparison is made between the respective satellite–derived SSS measurements, as well as between the satellite-derived SSS and Argo product. The purpose of the analysis is to test for low mean differences and standard deviations (SDs) in relation to in–situ based products between May 2010 and December 2016. By investigating the reliability and worth of L3 satellite salinity products, we examine differences in the salinity gradient. Salinity gradients are then used with the surface currents to estimate the horizontal advection of salt (Johnson et al. 2002).

2.2. Materials and Methods

2.2.1. Satellite and Observational Data

In this study, SSS from the European Space Agency (ESA) Soil Moisture and Ocean Salinity (SMOS), mission is used. SMOS has previously been found to exhibit bias: significant freshening in coastal areas, over–estimation of salinity in high southern latitudes and near the sea ice due to low temperatures, and in the presence of strong winds (Reul et al. 2012; Dinnat et al. 2014; Yin et al. 2014). In this study, the operational version 2.0 L3 unbiased binned product from the Barcelona Expert Centre (BEC) (Olmedo et al. 2016) at monthly 1°×1° resolution is used. This product is computed from the SMOS ESA version 6.22 SSS and empirically debiased using climatology to correct for land–sea contamination (Olmedo et al. 2016). This SMOS product should allow for reduced errors commonly found within the high latitudes and areas with strong surface currents (i.e. Malvinas Current region). SMOS data from May 2010 through December 2016 is used in this study.

Aquarius/SAC–D (Satélite de Aplicaciones Científicas–D), a joint NASA and the Argentinean Space Agency (CONAE) mission, provided nearly 4 years of continuous SSS data before ending on June 7, 2015. The current version of the Aquarius dataset, version

5.0, has a global root–mean-square error under 0.2 psu (Kao et al. 2017) (i.e. a mission objective), but limited peer–reviewed papers have been published on version 5.0. The previous version of the Aquarius dataset is known to be positively biased with respect to in–situ products in high latitudes and negatively biased in low latitudes (Le Vine et al. 2015; Lagerloef et al. 2015). In this study, we use Aquarius v5.0 L3 monthly 1° × 1° resolution binned product from September 2011 to May 2015 (duration of data collection for Aquarius). The dataset was retrieved from NASA's Jet Propulsion Laboratory, Physical Oceanography Distributed Active Archive Center (PO.DAAC).

NASA's Soil Moisture Active Passive (SMAP) is an Earth Satellite mission that primarily measures and maps soil moisture. The SMAP mission provides continuity in SSS estimates as the data is generated using the same core algorithm as Aquarius, and also distributed in a similar manner. To correct for surface roughness, other satellites on similar paths provide the surface wind speeds from the Remote System Sensing (RSS) WindSat and the Special Sensor Microwave Imager/Sounder (SSMIS) F17 (Wentz and Le Vine 2012; Wentz et al. 2013; Meissner and Wentz 2016). SMAP provides uninterrupted data continuity between the Aquarius–SMAP missions, improved spatial resolution (resolve mesoscale eddies, fronts, subduction and upwelling zones) near coastal zones (Meissner and Wentz 2016; Meissner et al. 2015). SMAP gridded resolution results in a 0.25° × 0.25° product, but further increases noise within the data. Monthly averaged products are available through JPL/NASA PODACC. Version 2.0 has been improved from the beta–version by significantly lower high latitude (zonal) and seasonal biases along the southern hemisphere continents (Meissner and Wentz 2016). For this study, the monthly averaged

L3 product was binned into 1° × 1° resolution to compare with that of Argo, SMOS, and Aquarius from May 2015 through December 2016.

Temporal and spatial scale variations are essential in the study of the ocean. The SO can have large SSS gradients along the ACC, seen in Figure 2.1. The small–scale variability (i.e. eddies, coastal processes) can be accounted for through SMAP in the original 0.25° × 0.25° gridded resolution format. Previous work has shown SMOS to have very similar estimations to Aquarius (Dinnat et al. 2014). However, SMOS regionally derives overall higher SSS in cold waters due to differences in dielectric constant models and dependence on latitude and temperature compared to Aquarius (Dinnat et al. 2014).

An Argo data product is obtained from the Asia–Pacific Data Research Center (APDRC) of the International Pacific Research Centre (IPRC). The specific APDRC Argo data product used in this study is the gridded monthly mean product on standard levels from January 2010 until December 2016. The Argo product is interpolated and smoothed in a 1° × 1° grid as far as 62.5°S in monthly format, with limited horizontal resolution and lower sampling frequency than that of satellite–derived products. This particular product from the APDRC is created through binned quality controlled salinity measurements, interpolated into a monthly grid (0 to 5m depth). This version of APDRC Argo product is hereon referred to as Argo.

2.2.2. Mean Difference and Variability

In order to statistically analyze the remotely–sensed L3 data, spatial and temporal comparisons are made using the defined SO region south of 30°S. The regions of interest are the entire SO and the Southern Hemisphere mid–latitude region within the SO (30°S–45°S), which allows for our estimate of the SO with limited bias from the low sea surface

temperatures and strong winds. Comparisons are made between the monthly products by estimating the differences and the standard deviation (SD) of the differences. This would allow for bias (error) to be determined and the variability in the differences of the products. In terms of variability, we used the 0.2 psu standard set by the Aquarius mission, although the mission goal is for the low–latitudes. To compare the satellites with in–situ data products, SMOS is compared from May 2010 to December 2016, Aquarius from September 2011 until May 2015, and SMAP from April 2015 until December 2016. To inter–compare satellite–derived products, Aquarius and SMOS are compared for the duration of the Aquarius product, September 2011 until May 2015, and SMAP and SMOS are compared between April 2015 and December 2016.

Seasonal comparisons are the months taken from (Ren et al. 2011). Therefore, in this study, austral summertime months are defined as January, February, and March; while austral winter months are defined as July, August, and September. Seasonal differences in salinity and horizontal salt fluxes represent a near maxima and minima for sea ice extent and yearly salinity variations (Ren et al. 2011). Although a seasonal comparison is made, there are still very limited in–situ observations available within the high latitudes of the SO, stressing the importance of satellite–derived estimations.

2.2.3. Salinity Gradients and Estimation of Horizontal Salt Fluxes

The salinity products used within the analysis do not estimate the ocean surface current velocities. In estimating the horizontal advective salt flux, the differences between the results would be the finite differences in salinity. Therefore, we will make a comparison of the salinity gradients and the horizontal salt advection. Estimations of the zonal and meridional gradients of salinity are computed individually using Aquarius, SMOS, and

SMAP. Ocean Surface Current Analysis Real–time (OSCAR) (Bonjean and Lagerloef 2002) currents are used to infer the zonal and meridional surface currents (m s^{-1}) between 2010 and 2017.

The surface gradients are calculated similar to (Johnson et al. 2002). The salinity gradient (***gradSSS***) is decomposed into the zonal (***x***), meridional (***y***), and vertical (***z***) coordinates and ***a***, ***b***, and ***c*** are unit vectors in the zonal, meridional, and vertical directions respectively. The salinity gradient is in units of x10^{-6} psu m^{-1}.

$$\text{gradSSS} = \nabla SSS = \frac{\partial SSS}{\partial x}\mathbf{a} + \frac{\partial SSS}{\partial y}\mathbf{b} + \frac{\partial SSS}{\partial z}\mathbf{c} \quad (2.1)$$

To compare the importance of SSS, the salinity gradients are applied to the steady–state balance between the atmospheric forcing (E – P), advection of salt is described similar to (Johnson et al. 2002).

$$E - P \cong U \cdot \nabla SSS = \frac{H_0}{S_0}\left[U\frac{\partial SSS}{\partial x} + V\frac{\partial SSS}{\partial y} + W\frac{\partial SSS}{\partial z}\right] \quad (2.2)$$

For simplicity, H_0 is the surface layer depth of 32.5 m (depth of valid satellite–derived surface currents) and S_0 is the mean salinity of 35 psu, the same values as in (Johnson et al. 2002). ***U*** is the velocity vector. Velocities and coordinates are defined with ***U*** and ***x*** as the zonal, ***V*** and ***y*** are the meridional, and ***W*** and ***z*** the vertical components. In this analysis, we focus only on the horizontal salt advection (A_h; i.e. the zonal and meridional components), as the vertical component is relatively small (Johnson et al. 2002).

$$A_h = \frac{H_0}{S_0}\left[U\frac{\partial SSS}{\partial x} + V\frac{\partial SSS}{\partial y}\right] \quad (2.3)$$

The units used for advection are presented in mm $month^{-1}$.

2.3. Results

2.3.1. Comparison of Satellite–derived salinity Products with Argo

Spatial averages of mean differences and SDs can be found in Table 2.1 and Figures 2.2 and 2.3. The spatio–temporal mean difference with respect to Argo in the entire SO for Aquarius is –0.025 psu and 0.001 psu for SMOS, with mid–latitude discrepancies of –0.052 psu (Aquarius) and –0.056 psu (SMOS) respectively. SMOS has positive bias with Argo in the high latitude and negative bias in the mid–latitudes that negate in the spatial mean. SMAP differs from the other satellites by having a near ubiquitous negative bias (Figure 2.2c, –0.150 psu) in the SO. The negative bias of SMAP is between –0.10 to –0.25 psu for the SO (Figure 2.3a). This consistent bias is important to note as SMAP has similar variability by latitude as SMOS and Aquarius (Figure 2.3b). Between all three satellites, the largest SDs occur near the Drake Passage and Malvinas current. The lowest spatio–temporal mean SD (30°S–62.5°S) is from Aquarius (0.215 psu). Spatially–averaged SDs in SMOS are 0.294 psu and 0.325 psu in SMAP.

The lowest variability (Figure 2.2 d–f, Figure 2.3b) occurs in all three satellites within the Southern Hemisphere mid–latitude region (30°S–45°S), with much of the variability below 0.2 psu, the low–latitude mission goal of Aquarius. Within the high latitudes, the variability increases along the ACC, sea–ice, and Drake Passage region. These regions are typically under–sampled with Argo floats for 1° resolution and have sharp salinity gradients.

The zonally averaged mean difference values shown in Figure 2.3a display the low value of discrepancies for Aquarius and SMOS between 30°S–45°S, with values on

average below 0.1 psu. Poleward of 45°S, the magnitude of mean difference within Aquarius and SMAP increase in magnitude, whereas SMOS increases in magnitude to a lesser extent due to offset of spatial positive/negative biases. The zonally averaged SD values further show the low variance within the Southern Hemisphere mid–latitude region. For much of the SO, Aquarius has the lowest zonally averaged variation, below 0.2 psu to approximately 52°S.

To compare the satellites in a temporal–scale comparison, the latitudinal distribution of monthly–mean differences and SD (Figure 2.4) are analyzed for the SO. Fluctuating variability indicates seasonal biases in SMOS and Aquarius. There is a consistent austral summer bias in Aquarius and an austral winter bias in SMOS. There is potentially an austral winter bias in SMAP, but a longer temporal scale would be required. Figure 2.4 further shows the low variability within the mid–latitude region of the SO, with values below 0.2 psu in both Aquarius and SMOS south of 50°S. Although the values are averaged by latitude, the low variability in Aquarius and SMOS is indicated by much of the SO with low standard deviation, but all three satellites still show large variability to the Argo product in the high latitudes. These biases in the satellite products are likely caused by a combination of the surface roughness, low surface temperatures, and salinity–derivation methods (Reul et al. 2012; Dinnat et al. 2014; Yin et al. 2014; Lagerloef et al 2015; Meissner and Wentz 2015; Kao et al. 2017), and are further discussed in section 4.1 of the *Discussion*.

2.3.2. Comparison between Satellite–Derived Salinity products

To visually compare the satellite–derived salinity against another, mean differences between monthly Aquarius, SMOS, and SMAP for all corresponding data points from September 2011 until December 2016 have been plotted to compare the satellites spatially (Figure 2.5) and temporally (Figure 2.6). Statistical values of the difference and variability are found in Table 2.2. Differences between Aquarius and SMOS (Figure 2.5a–b, Figure 2.6a–b) exhibit strong seasonal bias, as there is increased variability in Aquarius during Austral Summer and in SMOS during Austral Winter. Despite the seasonal biases, the mean differences are similar to the comparisons with the in–situ data. However, the variability between Aquarius and SMOS is greater in the SO (0.284) than compared to Argo. Similar variability exists between SMAP and SMOS, having strong SO of 0.342. The differences between SMAP and SMOS are increasing in magnitude and variability dramatically increased towards the end of 2016. The differences between SMAP and SMOS are not analyzed beyond December 2016, but further analysis should investigate the disparity between the two products. The largest mean difference and variability between the satellite–derived salinity exists in the in the high latitude, similar to the Argo product.

Although the satellites derive similar regional mean differences to in–situ observations, there is increased variability between the satellite–derived SSS. Comparing the values in Figures 2.5 and 2.6 to the Argo product comparisons in Figures 2.2 and 2.4, differences in Aquarius minus SMOS and SMAP minus SMOS are much larger than differences to the Argo product. Differences and SDs from Aquarius minus SMOS and SMAP minus SMOS are larger than compared to Argo, with mean differences larger in magnitude and SDs well above the 0.2 psu bar.

2.3.3. Comparison of Salinity Gradients and Horizontal Fluxes

Differences between Aquarius and SMOS (Figure 2.7c) zonal gradients are similarly co–located within regions of high SSS variability. The mean (SD) zonal gradient difference between Aquarius and SMOS is 0.123 $x10^{-6}$ psu m^{-1} (2.52 $x10^{-6}$ psu m^{-1}) in the SO. Differences in SMAP and SMOS (Figure 2.7g) zonal gradients are on average larger than that of Aquarius and SMOS, with a greater area of high variability (Figure 2.7h). The mean (SD) zonal gradient difference between SMAP and SMOS for the SO is 0.006 $x10^{-6}$ psu m^{-1} (3.00 $x10^{-6}$ psu m^{-1}). In both comparisons, large differences are located along coastal boundaries and sea–ice extent, regions known to produce errors in satellite–derived SSS. Differences between the satellites are further driven by the area of swath coverage and the amount of smoothing within the L3 products. The gradients reveal the increased smoothing in SMOS (Figure 2.7b, 7f) compared to Aquarius (Figure 2.7a) and SMAP (Figure 2.7e). Similar results are found within the meridional gradients, although there is less variability between the differences in meridional gradients (Figure 2.8) than zonal. The mean (SD) meridional gradient difference between Aquarius and SMOS is –0.182 $x10^{-6}$ psu m^{-1} (1.49 $x10^{-6}$ psu m^{-1}) and between SMAP and SMOS is 0.037 $x10^{-6}$ psu m^{-1} (1.76 $x10^{-6}$ psu m^{-1}) in the SO.

To quantitatively show how satellite–derived SSS play a role in the discrepancies in horizontal advective salt flux estimates, we compared with horizontal advective salt fluxes estimated from Argo (Figure 2.9 and Table 2.3). The comparison is made for all four products between 2010 and 2016. Since the same OSCAR currents are used in each calculation, the resulting difference in advection is due to the discrepancies in zonal and meridional salinity gradients. The monthly averaged horizontal advection is estimated

through Argo (Figure 2.9a). The scale of advection (mm month^{-1}) is the same as (Johnson et al. 2002), a typical scale to compare salinity and the atmospheric freshwater forcing. In the SO, the largest advection occurs along strong coastal currents and the ACC. The Malvinas and Agulhas regions, two regions of large advection, are also noted to have large variability between in–situ and satellite–derived salinity (Figures 2.2 and 5). In comparison of the horizontal advective fluxes, the largest differences occur within the ACC, Agulhas, and Malvinas regions, all regions of high variability. Moreover, the differences are as large as the mean fluxes. The mean SO (SD) difference between Argo and Aquarius is 9.64 mm month^{-1} (346.2 mm month^{-1}), 1.61 mm month^{-1} (276.6 mm month^{-1}) with SMOS, and 0.74 mm month^{-1} (417.5 mm month^{-1}) with SMAP.

2.4. Discussion

2.4.1. Satellite–derived salinity

Aquarius and SMOS have positive biases between 45°S–60°S and SMAP has a negative bias in the SO, likely resulting from the influence of low sea surface temperatures and strong Westerlies. The L–band radiometer at low sea surface temperatures have previously been noted to have low sensitivity in the high latitudes (Lee 2016). Previous SMOS products discussed SDs between 0.4 to 0.5 psu for the different basins of the Southern Ocean (Boutin et al. 2012), values much larger than that of the current unbiased SMOS product (Olmedo et al 2016). Our analysis indicates that the monthly SO SD differences is below previous estimates, but regionally has mean differences and standard deviations greater than 0.5 psu. Previous analyses found SDs of Aquarius and SMAP to Argo to be 0.25 psu or less globally, but as high as 0.5 psu in the higher latitudes (Lagerloef

et al 2005; Meissner and Wentz 2015; Kao et al. 2017). Similar to their findings, these calculations show a time–mean SO (global) SD of 0.215 (0.195) psu for Aquarius V5 and 0.325 (0.226) psu for SMAP V2, but regionally has mean differences and SDs larger than 0.5 psu for both Aquarius and SMAP. Similar to Kao et al (2017) and Lee (2016), the greatest discrepancies and variability compared with Argo and the Aquarius data product (Figure 2.2) are within the Malvinas, Agulhas retroflection region, and the southern extent of sampling; all regions with sharp surface salinity gradients or are heavily under–sampled. This is a common signature found within all three L3 products compared with the Argo product, and not just Aquarius.

Both SMOS and Aquarius experience strong interannual variability. The increased austral summer bias in Aquarius and austral winter SMOS are likely related to the low sea surface temperature, a result from the accuracy of brightness temperature measurements in the high latitudes. Both Aquarius and SMOS seasonal biases are evident within high latitudes. The largest differences and variability occur at the high latitudes and the ACC region. There is no clear seasonal pattern observed in SMAP due to the short temporal period, but could potentially have a similar high latitude seasonal bias of SMOS (Figure 2.4).

The resulting inter–comparison of satellite–derived SSS indicates disagreement between the satellites along the sea ice extent, the continents, and regions of the ACC. The differences in satellite–derived salinity supports the strong variability in regions of strong winds, low sea surface temperatures, and coastal regimes, similar to what is indicated in the comparison with the Argo product. Differences between the satellites could result from bias in algorithms. For example, SMOS has previously been described to have freshening

in coastal regions due to contamination from land surfaces, over estimation in high latitudes due to the methods in dielectric constant, and errors associated with surface roughness (Reul et al. 2012; Dinnat et al. 2014; Yin et al. 2014) and Aquarius to be positively biased in high latitudes (Lagerloef et al 2015; Meissner and Wentz 2015; Kao et al. 2017).

The differences between respective satellite–derived salinity is greater than the differences to Argo, with SDs between Aquarius and SMOS nearly twice as much as compared with Argo. This increased mean difference and larger variability in the entire SO indicates the high degree of variability within the surface centimeters, but mainly the large variability in the remotely sensed products. The comparisons of satellite–derived salinity indicate large variability between products in the high latitudes and the ACC region of the Southern Hemisphere, despite newer releases of the satellite–derived products better accounting for high latitude biases. Not only is there large variability in the high latitudes when compared with Argo, but larger variability exists between the satellites. It is important to consider the vast differences in the derived products based on the ability to alter models, re–analyses, or estimated hydrological balances.

2.4.2. Salinity Gradients and Horizontal Fluxes

The variability between SSS gradients have the ability to significantly influence the results of SO analyses on the hydrologic cycle (Johnson et al 2002; Yu 2011). The zonal SSS gradients plotted in Figure 2.7 further show the similarities and differences between the satellites. Large gradients greater than 1.0 $x10^{-6}$ psu m^{-1} exist near coastal boundaries and within strong current regions such as the ACC, Agulhas, and Malvinas. Gradients are relatively small within the open ocean for each of the satellite–derived product. In previous

analyses, there are larger salinity gradients and variability in the SO meridional gradient component than the zonal (Yu 2011). The meridional gradients are greatest along the ACC and near the sub-tropical maxima regions, greater than 2.0 $x10^{-6}$ psu m^{-1}. Here, the meridional gradients (Figure 2.8) are nearly two times greater than the zonal gradients (Figure 2.7) in satellite–derived products, but differences between the zonal and meridional gradients in satellite products are large. The mean difference in the SO zonal gradients between Aquarius and SMOS is 0.123 psu m^{-1} and 0.006 psu m^{-1} between SMAP and SMOS; however, the SDs are 2.52 $x10^{-6}$ psu m^{-1} and 3.00 $x10^{-6}$ psu m^{-1} respectively. The mean difference in the SO meridional gradients between Aquarius and SMOS is –0.182 $x10^{-6}$ psu m^{-1} and 0.037 $x10^{-6}$ psu m^{-1} between SMAP and SMOS; however, the SDs are 1.49 $x10^{-6}$ psu m^{-1} and 1.76 $x10^{-6}$ psu m^{-1} respectively. The zonal SSS gradient is shown to exhibit relatively large variability in gradient differences compared to the meridional gradient in each comparison of Aquarius, SMOS, and SMAP. Therefore, estimations of SSS and the associated gradients are of utmost importance, as differences in the satellite products are on the same magnitude as the gradients.

Horizontal advection estimated through Argo and differences with the satellites indicate the largest discrepancies are in the high latitude and coastal currents, both areas described to have large differences between salinity products. Outside of the very high latitudes and coastal regions, the main driving force between oceanic and atmospheric forcing are the balance in salinity advection and net precipitation (Yu 2011). The monthly SD for the Argo product horizontal advective flux is 87.2 mm $month^{-1}$ in the SO. The mean difference in the satellite-derived products with respect to Argo for the SO are all less than 2 mm $month^{-1}$ for SMOS and SMAP, but larger than 9.6 mm $month^{-1}$ with Aquarius.

SMOS further has a relatively low standard deviations of the monthly differences, 276.6 mm month^{-1}, but has larger variability in Aquarius and SMAP. SMOS indicates the lowest differences and variability to that of Argo derived fluxes, but could further be a result of smoothing within the products. The SMOS product is smoothed more than the other satellite-derived products, which could result in more similar gradients to that of the smoothed in–situ product.

From the comparison in Figure 2.9, the variability in SSS alone is enough to derive differences on the same order of magnitude as the horizontal advection, without including the vertical flux component or runoff from land. As a result, the spatial resolution, smoothing, and satellite–derived SSS algorithm all can strongly influence hydrologic balance calculations, especially south of 45°S. The SO is known to have limited temporal resolution with in–situ observations, especially in austral winter months. The need to reduce the differences in salinity and horizontal salt fluxes between satellites products alone would help our understanding of the hydrologic cycle.

2.5. Conclusions

To conclude, this paper emphasizes the use of satellite–derived salinity data to better understand the SO and its interacting air–sea processes. With modern remote sensing techniques, the ability to spatially and temporally monitor SSS has been greatly enhanced compared to in–situ techniques. Using Aquarius, SMOS, and SMAP salinity measurements, we find seasonal patterns of salinity discrepancies. In order to support the hypothesis, statistical analyses prove all three satellites to have low mean difference and variability in the Southern Hemisphere mid–latitudes, below a 0.2 psu limit. Although in

all three satellites, there are increasing differences and variability south of 50°S. This analysis found the temporal variability between the APDRC Argo product and Aquarius v5 to be 0.215 (0.195) in the SO (globally), 0.294 (0.265) with SMOS, and 0.325 (0.226) with SMAP. In comparison with an Argo product in the Southern Hemisphere mid–latitudes, all three satellites averaged standard deviations below 0.2 psu.

Spatial distributions show the strong high latitude positive bias of Aquarius and SMOS and the negative Aquarius bias along sea–ice. SMOS is found to have a low mean difference within the SO, but further spatial comparison reveals the negating of negative/positive biases. Comparatively, SMAP has a ubiquitous negative bias to the Argo product for the SO, except for the Drake Passage. Additionally, the largest differences and variability is found in the Drake Passage region with all three satellites. A temporal analysis further showed the seasonal high latitude bias, increasing austral summer variability in Aquarius and austral winter variability in SMOS. In comparison of the satellite–derived salinity, the differences and variability are greater than that of the variability with in–situ observations.

In the estimations of horizontal advective fluxes, the zonal SSS gradient indicates that differences in satellite–derived products are the same order of magnitude as the zonal gradients. The zonal (meridional) gradient SD between Aquarius and SMOS is estimated to be 2.52 psu m^{-1} (1.49 psu m^{-1}) and between SMAP and SMOS is 3.00 psu m^{-1} (1.76 psu m^{-1}). The estimation of meridional gradient indicates differences in satellite–derived techniques differ slightly, being an order of magnitude less than the meridional gradient and lower variability. The horizontal advection is estimated in all Argo, Aquarius, SMOS, and SMAP products for a single month. The results indicate advective fluxes estimated in

all products strongly vary in the SO, particularly poleward of the ACC and along coastal regions. The mean differences in SO horizontal advective fluxes are on average small with SMOS and SMAP, less than 2.0 mm $month^{-1}$, but only SMOS has variability below 300.0 mm $month^{-1}$ in the SO.

These results are important to consider as differences in salinity are influenced by sampling depths, under–sampling of Argo in high latitudes, satellite footprint, data smoothing, and grid size. Moreover, the use of L–band derived techniques are known to be strongly biased in low temperatures, but yet the high latitudes are important to monitor to better understand global cycles and climate variability. Using various satellite products could provide a useful tool to analyze and monitor the hydrological cycle, but differences in the products and smoothing could significantly skew the results. Although satellite–derived SSS has improved throughout the SO, the large variability between remotely sensed techniques indicates the importance to further improve spatial and temporal scales, that can lead to ground–breaking advances in global climate, circulation, and hydrological cycles.

Table 2.1. The mean temporal difference and standard deviation (psu) between satellite–derived salinity and Argo. The values noted are taken from Figure 2.2. In comparison with the Argo product, global values refer to the area between 62.5ºN and 62.5ºS.

Satellite	Mean Difference (psu)			Standard Deviation (psu)		
	62.5ºN–62.5ºS	30ºS–62.5ºS	30ºS–45ºS	62.5ºN–62.5ºS	30ºS–62.5ºS	30ºS–45ºS
Aquarius	–0.040	–0.025	–0.052	0.195	0.215	0.134
SMOS	–0.010	0.001	–0.056	0.265	0.294	0.148
SMAP	–0.062	–0.150	–0.157	0.226	0.325	0.176

Table 2.2. The mean temporal difference and standard deviation (psu) between satellite–derived salinity products. The values noted are taken from Figure 2.5.

Satellite	Mean Difference (psu)			Standard Deviation (psu)		
	Global	30°S–62.5°S	30°S–45°S	Global	30°S–62.5°S	30°S–45°S
Aquarius – SMOS	–0.083	–0.078	–0.010	0.362	0.284	0.180
SMAP – SMOS	–0.096	–0.216	–0.115	0.388	0.342	0.236

Table 2.3. The mean temporal difference and standard deviation (psu) between satellite–derived and Argo horizontal advective fluxes. The values noted are taken from Figure 2.9. In comparison with the Argo product, global values refer to the area between 62.5ºN and 62.5ºS.

Satellite	Mean Difference (mm month^{-1})			Standard Deviation (mm month^{-1})		
	62.5ºN–62.5ºS	30ºS–62.5ºS	30ºS–45ºS	62.5ºN–62.5ºS	30ºS–62.5ºS	30ºS–45ºS
Aquarius	4.85	9.64	11.34	451.7	346.2	304.8
SMOS	1.85	1.61	0.50	275.7	276.6	253.0
SMAP	3.60	0.74	–0.46	416.0	417.5	330.9

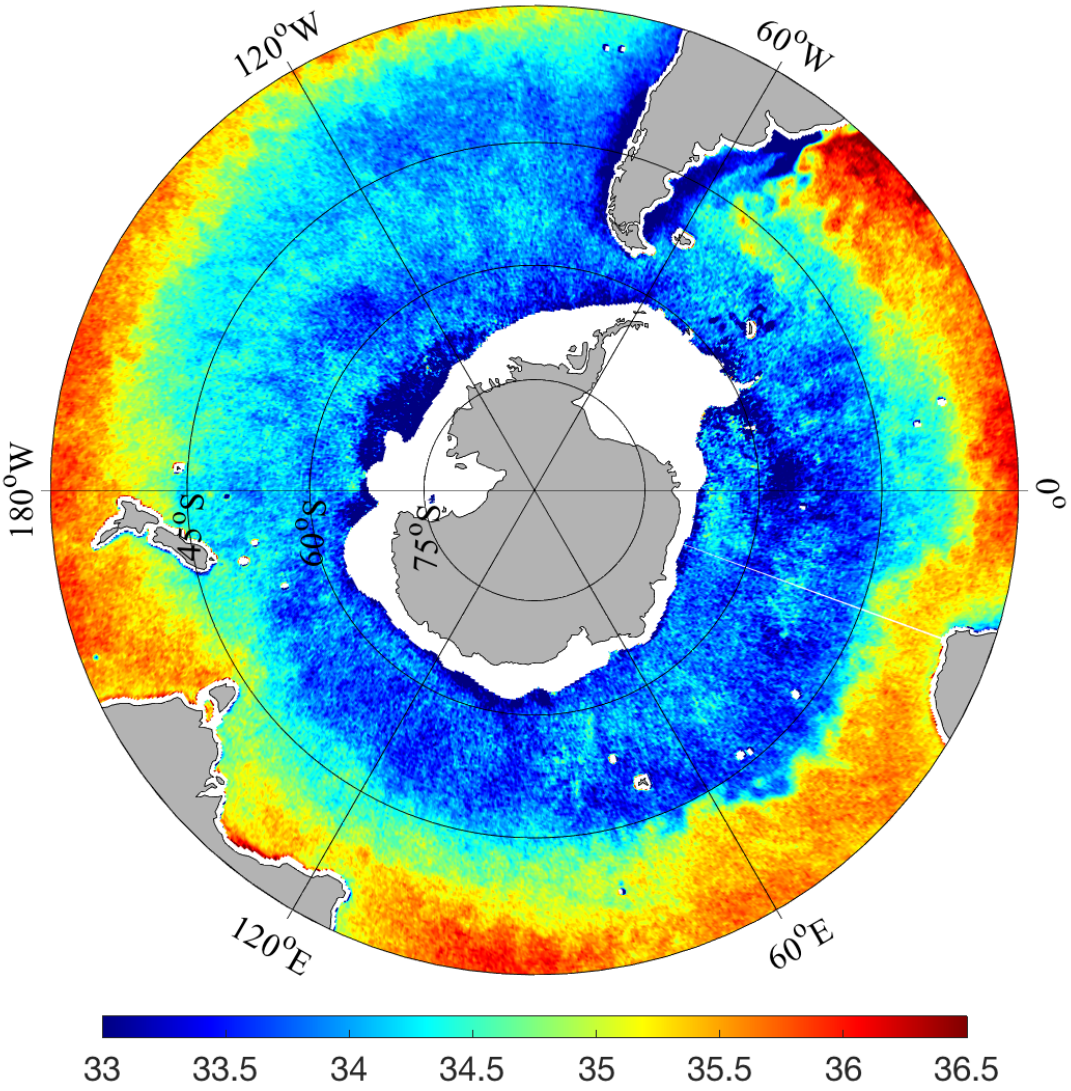

Figure 2.1. Monthly mean sea surface salinity during January 2016 from SMAP level 3 product at 0.25° resolution, encompassing latitudes south of 30°S.

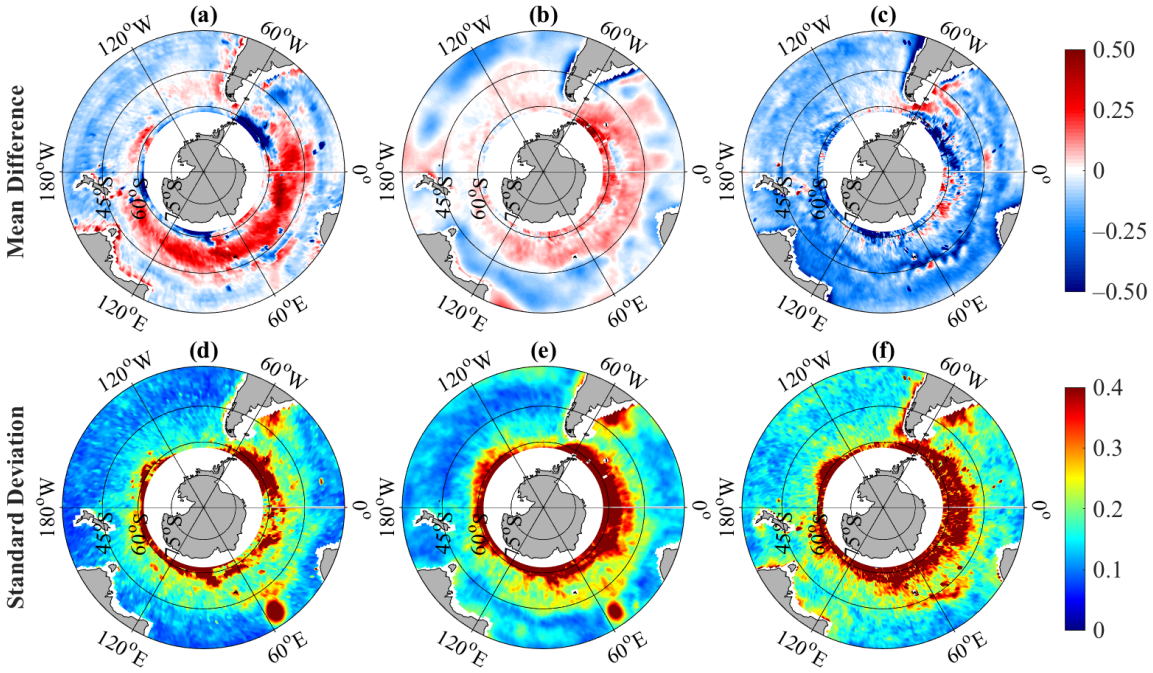

Figure 2.2. Mean differences (a – c) and standard deviations (SDs) of SSS differences (d – f) between satellite–derived salinity and Argo (psu). Aquarius (a, d) is compared from September 2011 to May 2015, SMOS (b, e) May 2010 through December 2016, and SMAP (c, f) April 2015 through December 2016. Corresponding mean values are in Table 2.1 and units for salinity are in psu.

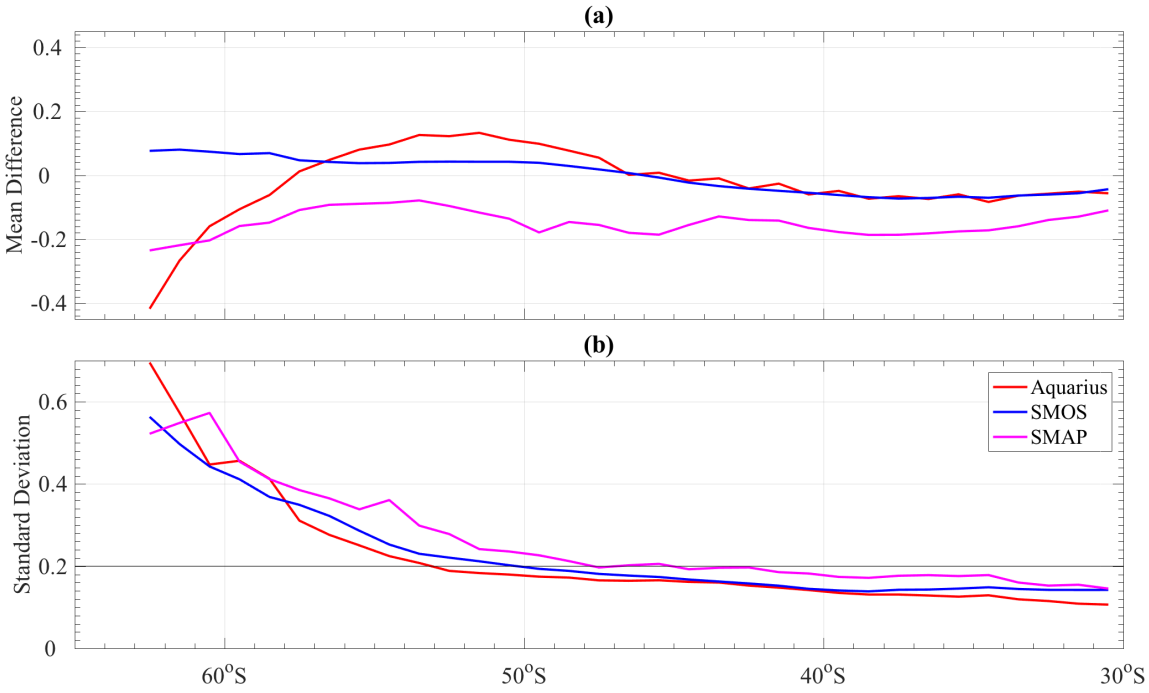

Figure 2.3. Zonal averages of mean difference (a) and standard deviation (SD) (b) between satellite–derived salinity and Argo surface salinity (psu) in 1° resolution. Differences between (red) Aquarius and Argo are from September 2011 to May 2015, (blue) SMOS and Argo are May 2010 through December 2016, and (magenta) SMAP and Argo are from April 2015 through December 2016. All data points are for corresponding spatial locations within the domain of Figure 2.1.

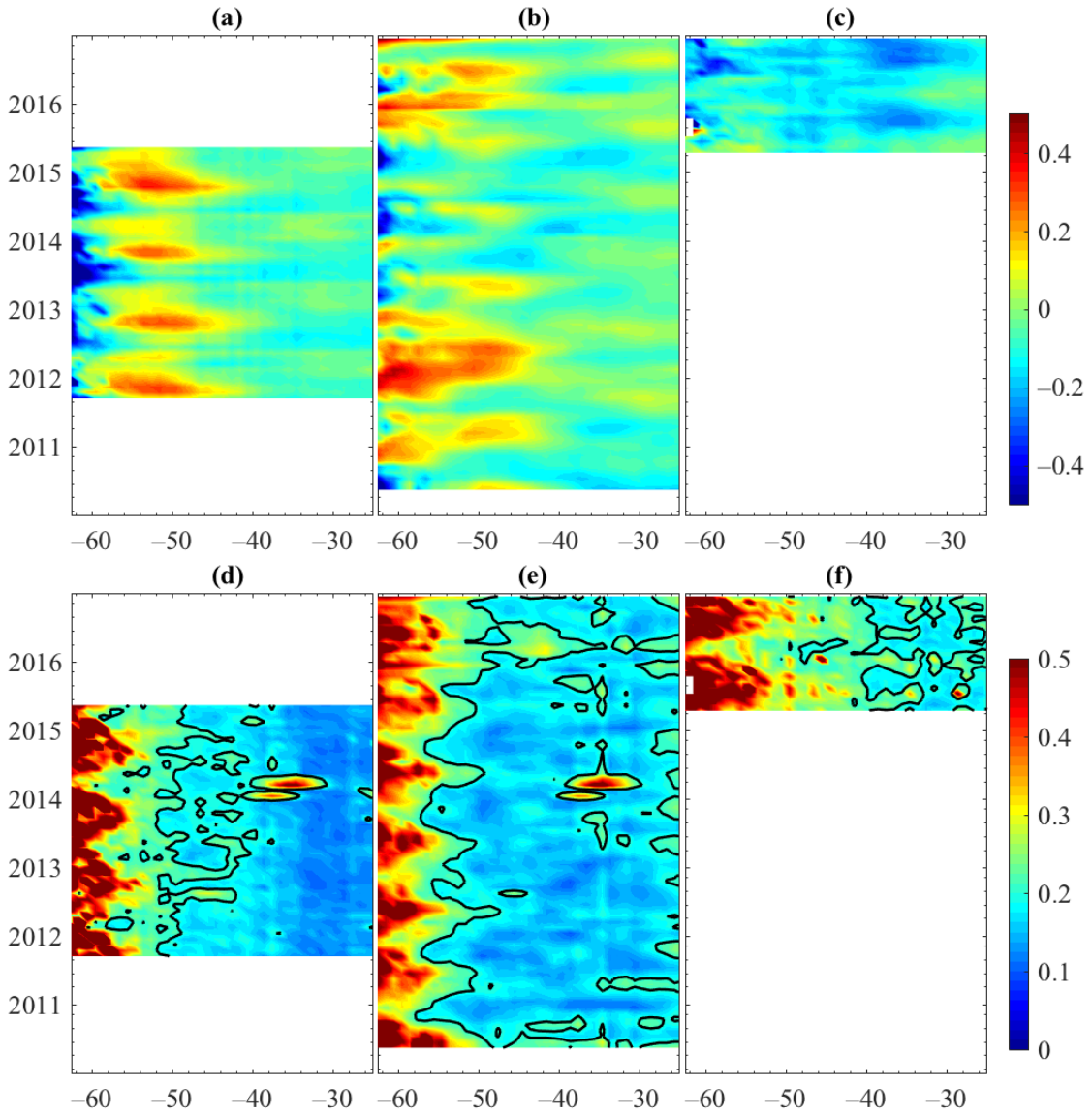

Figure 2.4. Comparison of salinity derived from Aquarius (a, d), SMOS (b, e), and SMAP (c, f) to the Argo product from 2010 through 2016. Each mean difference satellite minus Argo (a–c) and standard deviations (SDs) (d–f) are averaged over latitude. Aquarius is compared from September 2011 to May 2015, SMOS during May 2010 through December 2016, and SMAP during April 2015 through December 2016. Units are in psu.

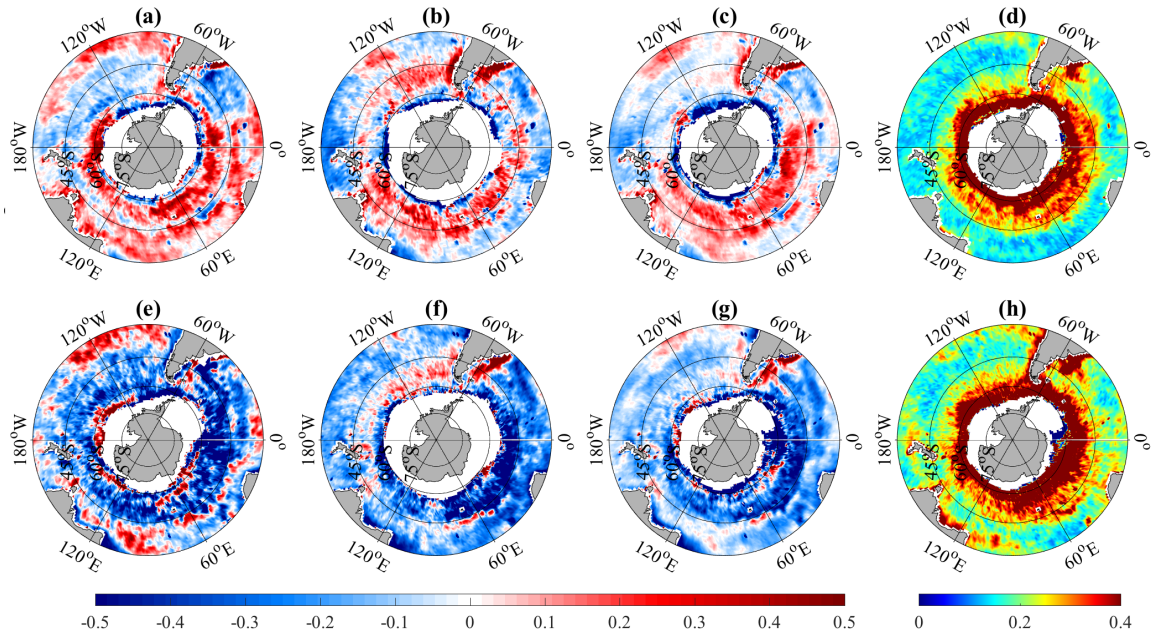

Figure 2.5. Mean sea surface salinity (SSS) (psu) differences (a, b, and c) and standard deviation (SD) (d) between Aquarius minus SMOS from September 2011 to May 2015 and similarly SMAP minus SMOS (e–h) from April 2015 to December 2016. (a) and (e) is the austral summer, (b) and (f) the austral winter, and (c) and (g) the temporal comparisons between the satellites.

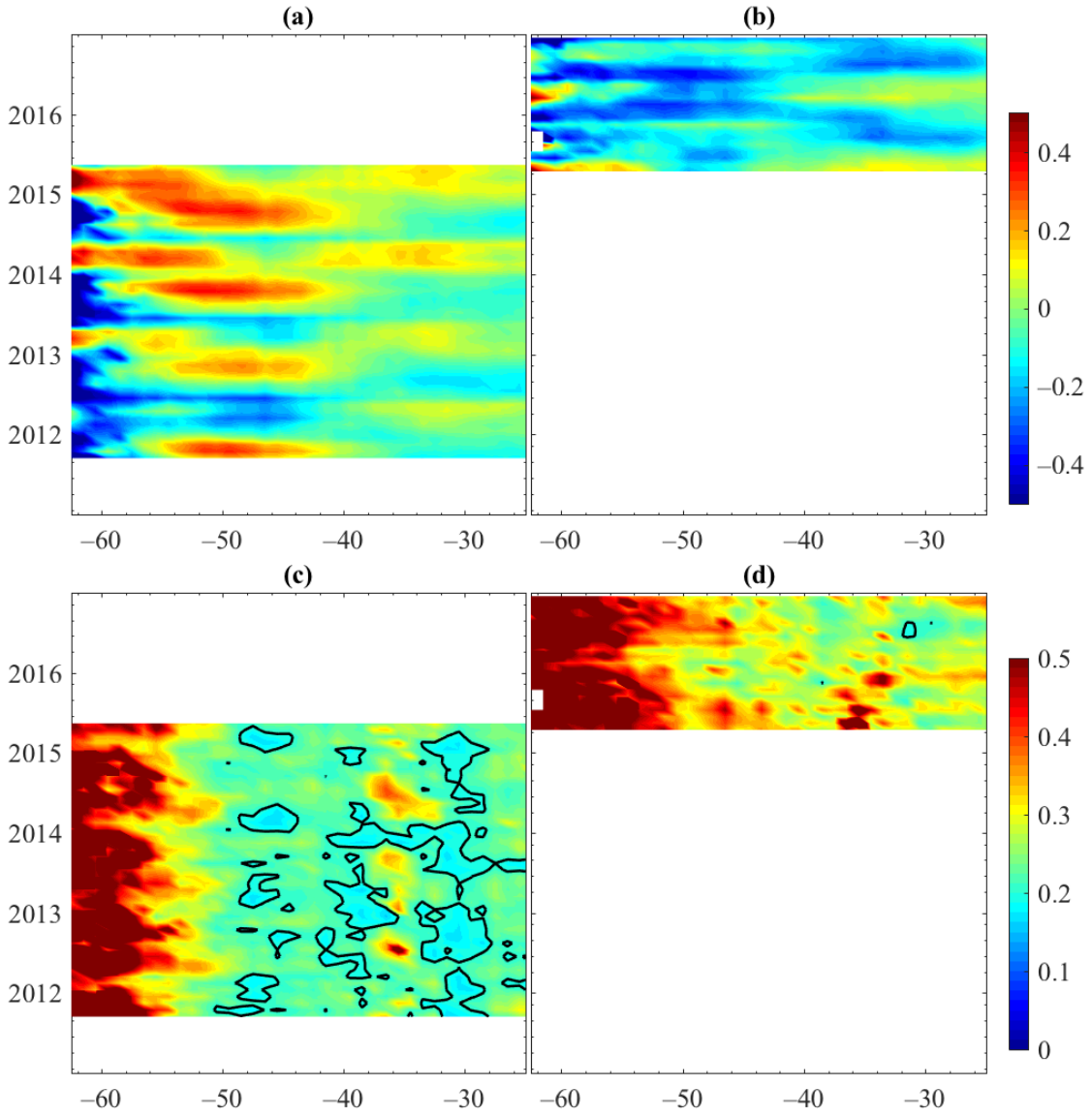

Figure 2.6. Comparison of Aquarius minus SMOS salinity (a, c) and SMAP minus SMOS salinity (b, d) between 2011 and 2016. Each mean difference between these satellite products (a–b) and standard deviations (SD) (c–d) are averaged by latitude. Aquarius minus SMOS is compared from September 2011 to May 2015 and SMAP minus SMOS compared from April 2015 to December 2016. Units are in psu.

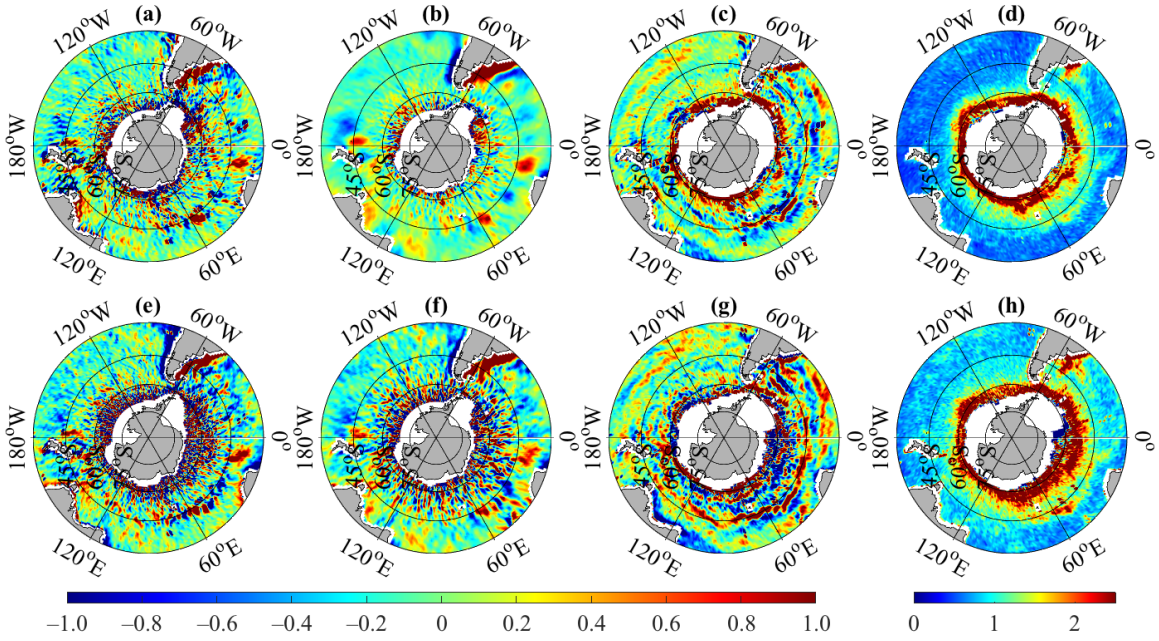

Figure 2.7. Temporal mean zonal surface salinity gradient (x10^{-6} psu m^{-1}) for Aquarius (a), SMOS (b, f), and SMAP (e). Differences in the mean zonal salinity gradient between Aquarius and SMOS (c) and SMAP and SMOS (g) and the standard deviations (SDs) between Aquarius and SMOS (d) and SMAP and SMOS (h). The duplication of SMOS shows the average zonal flux taken during Aquarius time period (b) and that of SMAP (f).

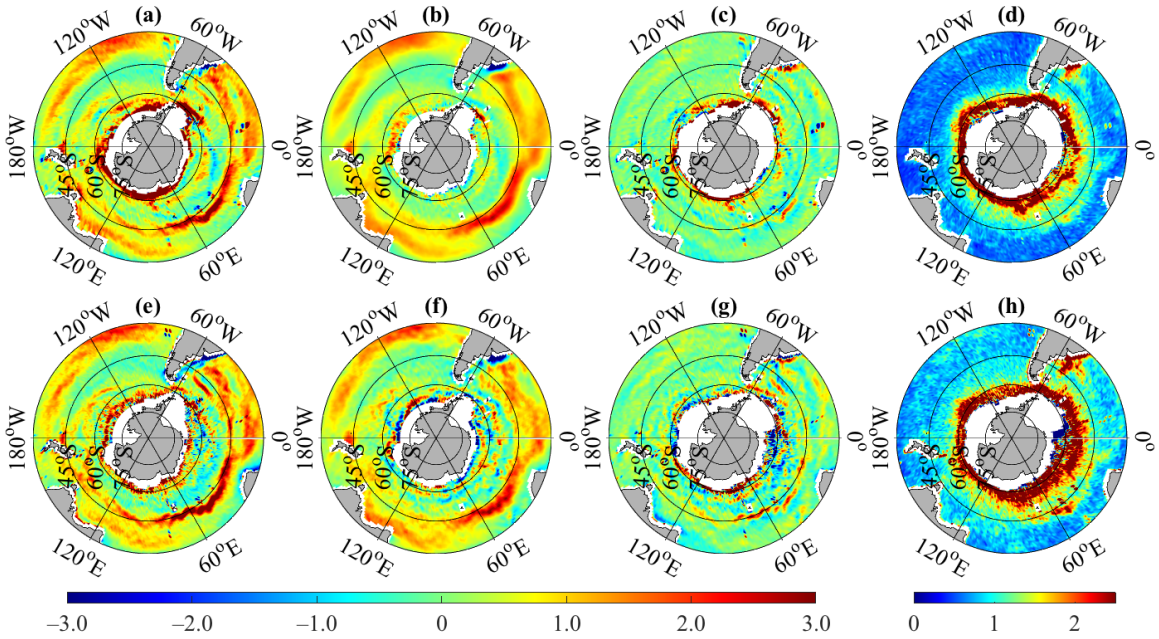

Figure 2.8. Temporal mean meridional surface salinity gradient (x10^{-6} psu m^{-1}) for Aquarius (a), SMOS (b, f), and SMAP (e). Differences in the mean meridional salinity gradient between Aquarius and SMOS (c) and SMAP and SMOS (g) and the standard deviations (SD) between Aquarius and SMOS (d) and SMAP and SMOS (h). The duplication of SMOS shows the average meridional flux taken during Aquarius time period (b) and that of SMAP (f).

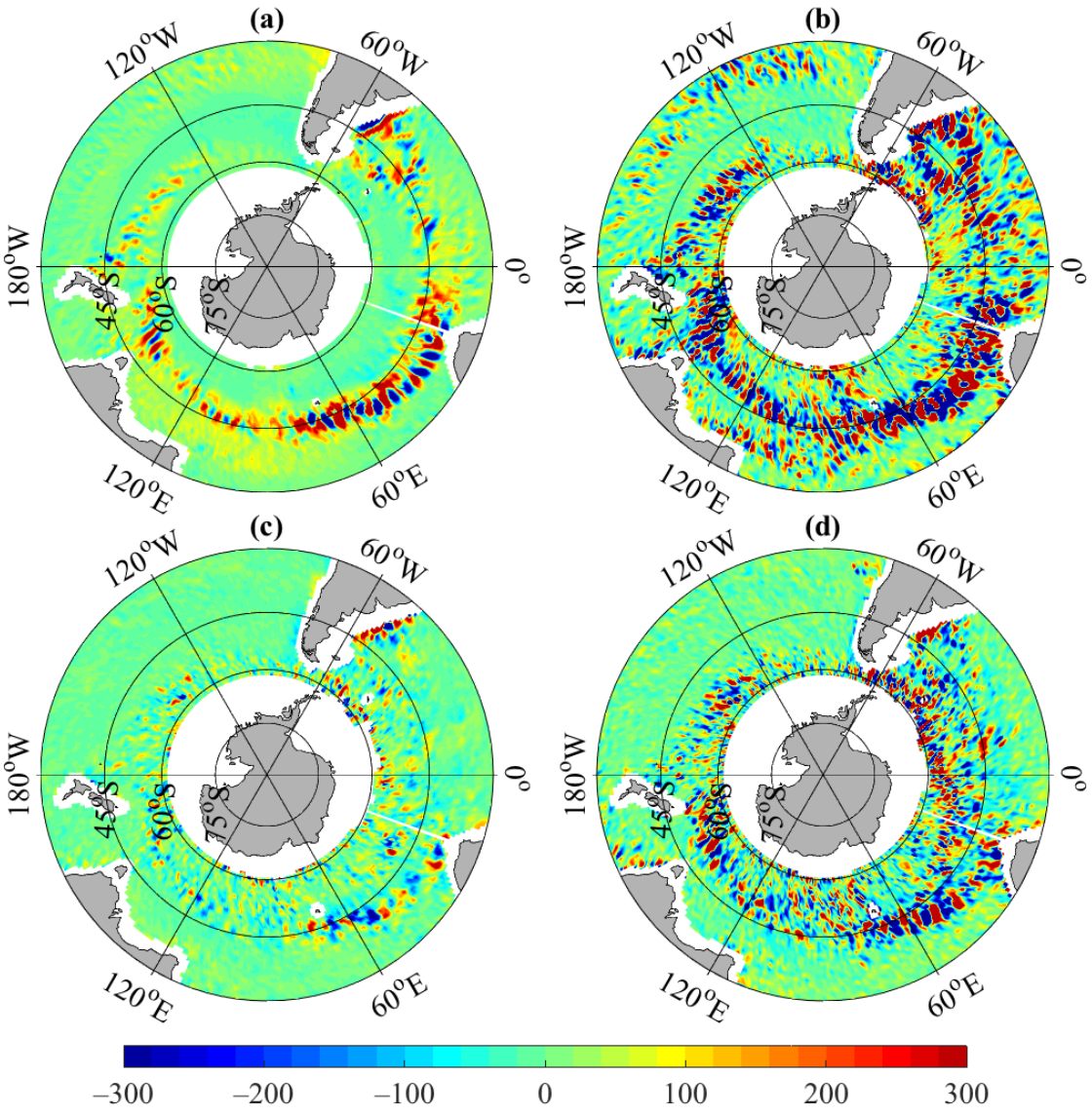

Figure 2.9. Mean difference in horizontal surface salt advection (mm month^{-1}). Argo monthly mean horizontal surface salt advection (a) between 2010 and 2016 (mm month^{-1}). Differences between Aquarius (b), SMOS (c), and SMAP (d) minus Argo horizontal surface salt advection. Aquarius is compared from September 2011 to May 2015, SMOS is from May 2010 through December 2016, and SMAP is compared April 2015 through December 2016. Corresponding values are in Table 2.

CHAPTER 3

VARIABILITY OF SOUTHERN OCEAN TRANSPORTS[2]

[2]Ferster, B. S., B. Subrahmanyam, I. Fukumori, and E. S. Nyadjro (2018). Variability of Southern Ocean Transports, Journal of Physical Oceanography, 48(11), doi:10.1175/JPO-D-18-0055.1.

Abstract

The Southern Ocean (SO) is capable of transporting vast amounts of salt, heat, and nutrients, which allows it to influence and regulate global climate. The variability of depth- and density-integrated volume transports in the SO is studied using Estimating the Circulation and Climate of the Ocean (ECCO) version 4 release 3 (1992-2015) ocean state estimate. The estimate has a net eastward transport of 150.6 ± 5.5 Sv, 162.6 ± 7.4 Sv, and 148.2 ± 5.4 Sv between the Atlantic-Indian, Indian-Pacific, and Pacific-Atlantic basins, respectively. The time-mean meridional volume transport across 30° S in the Atlantic is estimated to be -1.4 ± 0.6 Sv, -14.4 ± 3.5 Sv in the Indian basin, and 15.5 ± 4.1 Sv in the Pacific, where negative values are southward. Trends in net volume transport between the basins are statistically insignificant. Within the water column, however, the middle and lower branches of the Meridional Overturning Circulation have trends of −0.289 Sv decade^{-1} and 0.248 Sv decade^{-1} in the Atlantic basin. The Indian and Pacific basins have decreasing trends in their lower overturning cells. These results indicate increased overturning circulation within the lower branch in the South Atlantic and decreased lower branch circulation within the Indian and Pacific basins, and have implications on the thermohaline-driven circulation. Using ECCO, we estimate a southward potential temperature transport of –176.2 ± 197.2 °C Sv and salinity transport of –1.71 ± 22.4 psu Sv into the SO, and indicate potential temperature transport is increasing by –15.0 ± 13.2 °C Sv decade^{-1}.

3.1. Introduction

The Southern Ocean (SO) is a major driving force in global climate and is an essential component in the global-scale meridional overturning circulation's (MOC)

distribution of heat, mass, and freshwater. Strong westerly winds drive the Antarctic Circumpolar Current (ACC) across the three major ocean basins (Rintoul and Naveira Garabato, 2013), and interact with eddies and jets to transfer energy and momentum from the ocean surface to the ocean floor (Moore et al., 2000; Thompson, 2010; Mitsudera et al., 2018). These westerlies drive the strong zonal transports of the ACC, but also result in the meridional Ekman-driven transport and upwelling along the sloping isopycnals. Ekman transport is important to global climate and budgets (i.e. heat, and carbon) indirectly via the contribution to sloping isopycnals (Toggweiler and Samuels, 1995; Marshall and Speer, 2012; Talley, 2013; Rintoul and Naveira Garabato, 2013). Together, the ACC, MOC, and polar gyres offer a three-dimensional passageway for global ocean circulation.

The MOC consists of two dominant counter-rotating cells separated by a neutral density surface of 27.6 kg m^{-3} (Marshall and Speer, 2012). The upper cell of the MOC consists of northward flowing Antarctic Intermediate and Subantarctic Mode Waters and southward flowing Circumpolar Deep Waters (CDW). The bottom cell consists largely of the northward flowing Antarctic Bottom Waters (AABW) and CDW returning southward. These MOC cells have been studied in recent model- and state estimate-based studies to better understand the mechanisms and forcings of interannual variations (Lumpkin and Speer, 2007; Cabanes et al., 2007; Wunsch and Heimbach, 2009; Talley, 2013; Mazloff et al., 2013; Bishop et al., 2016). The global MOC is described in more detail within Marshall and Speer (2012) and Talley (2013).

The dominant mode of atmospheric variability in the Southern Hemisphere is the Antarctic Oscillation (AAO). Positive phases of the AAO induce a southward shift and increase in magnitude of the westerly winds. In recent decades, the AAO has been shown

to display increasing tendencies of positive phases in model-based (Cai et al., 2003) and reanalysis (Thompson and Solomon, 2002) studies, and is thought to be driven through changes in the Antarctic ozone hole (Thompson et al., 2011). The shift in westerlies and increasing AAO tendencies are linked to the restructuring of the ACC fronts (Dong et al. 2006; Downes et al., 2011), driving the ACC southward (Hall and Visbeck, 2002; Sen Gupta and England, 2006). In the works of Sokolov and Rintoul (2009a, b), sea surface height is used to indicate a shift in the ACC southward by 0.6° between 1992 and 2007. In the work of Farneti et al. (2015), using Coordinated Ocean-Ice Reference Experiment Phase II (CORE-II) simulations, zonal transports in the SO are positively correlated to the AAO between 1958 and 2007. Additional model (Meredith and Hogg, 2006) and observational (Böning et al., 2008; Hogg et al., 2015) analyses discuss the influence and strength of the ACC as a result of the AAO. These analyses indicate the need to better account for eddy-variability in both fine and coarse resolution ocean models, as only small trends are found in ACC transport over multiple decades in response to increased westerlies.

While the CORE-II simulations cover multiple decades (1948-2009), more recent state estimates covering shorter periods have used improved model physics and *in situ* data to model the state of the ocean (Mazloff et al., 2010; Forget et al., 2015; Forget et al., 2016; Fukumori et al., 2017; Verdy and Mazloff, 2017). The recent state estimate of the Consortium for "Estimating the Circulation and Climate of the Ocean", version 4 release 3 (ECCO V4r3, hereon referred to as ECCO; Fukumori et al., 2017) models the time period 1992-2015. ECCO is a general circulation model (GCM) product and could further indicate changes in SO transports and the state of the climate. Although other state estimates, such

as the Southern Ocean State Estimate (SOSE) (Mazloff et al., 2010; Verdy and Mazloff, 2017), include finer eddy-permitting resolutions, ECCO has a longer temporal and spatial (global) extent. ECCO has been shown to adequately resolve large-scale ocean circulation and is consistent with observations (Forget et al, 2015; ECCO 2017a, b; Fukumori et al., 2017).

The objective of this paper is to analyze the magnitude and trends in subtropical MOC and the inter-basin zonal transports using ECCO. In order to examine the state of the SO MOC, meridional transports and trends are analyzed within the different water masses, based on density. The null hypothesis is that there are no significant trends in either the zonal or meridional depth- and density integrated volume transports throughout the 1992-2015 period. Potential temperature and salt transports are further analyzed within the SO, with the null hypothesis that there are no significant trends between 1992 and 2015. Previous works have shown regional temperature and salinity changes within the SO (Gille, 2002; Gille, 2008; Durack and Wijffels, 2010), in which the ECCO transports could be used to explain the changes in ocean state variables. The analyses described in this paper investigate the strength of the ACC and MOC over a 24-year period, with important results with respect to ocean heat content, sea-ice concentrations, and air-sea exchange studies.

3.2. Data and Methods

3.2.1. ECCO Ocean State Estimate

The ocean state estimates of the ECCO Consortium provide a convenient means by which to study ocean circulations and its temporal variations. ECCO is directed at making the best possible estimates by combining state-of-the-art ocean circulation models with

nearly complete global ocean data sets in a physically and statistically consistent manner (Wunsch et al., 2009). ECCO's ocean description is more complete than that of observations alone, as no observing system measures the complete state of the ocean in terms of variables (e.g., 3-dimensional time-varying velocity) and spatiotemporal extent (viz., all corners of the ocean from the surface to the bottom throughout the analysis period). The ECCO estimate is closer to observations than model simulations that are unconstrained by such measurements. In addition, unlike many other data assimilation products, the ECCO estimate is physically consistent in both state and its temporal evolution owing to the nature of its model-data synthesis. For instance, property budgets can be closed in terms of explicit physical processes. Here, we take advantage of these characteristics to explore the SO using the latest estimate of the ECCO Consortium.

The Consortium's latest product (Fukumori et al., 2017) spans the period from 1992 to 2015 and integrates nearly all extant ocean observations during this time with a coupled ocean-sea ice model based on the MIT general circulation model (MITgcm). The ECCO estimate has a nominal 1-degree horizontal grid spacing with 50 vertical layers ranging in thickness from 10 m near the surface to 456 m near the bottom at 6134 m depth. The model uses a so-called latitude-longitude-cap (LLC) grid that consists of a latitude-longitude grid outside of the Arctic domain, where instead a separate Cartesian coordinate system ("cap") is used to avoid the singularity of the former (See Forget et al., 2015 for details). The ECCO product additionally employs 3-dimensional, time-invariant mixing coefficients, further detailed in Forget et al. (2015).

In situ measurements are relatively limited in the high latitudes of the SO but have significantly improved under the Argo program and increased sampling (Lyman and

Johnson, 2014). The sparseness of the observations is mitigated by ECCO's dynamical system, which carries data information spatially and temporally across the modeled domain. ECCO has an average spatial resolution of 62 km south of 30°S (Forget et al, 2015), is atmospherically forced by ERA-Interim reanalysis (Dee et al., 2011), and includes an updated sea-ice model (Losch et al., 2010). ECCO additionally includes satellite-derived sea-surface salinity and ocean bottom pressure. This release of ECCO represents the first multi-decadal ocean state estimate that is truly global, including the Arctic. Basic descriptions of the estimate's property distribution can be found in reports by the ECCO Consortium (2017a, b) and Forget et al. (2015).

3.2.2 Estimation of Depth-integrated Volume, Salinity, and Potential Temperature Transports

Depth-integrated volume transports are calculated using ECCO within the region south of 30°S. The Atlantic-Indian exchange is defined at 20° E, the Indian-Pacific at 145° E, and the Pacific-Atlantic at 70° W. The meridional boundary of transports is defined at 30° S. For these analyses, the ACC region is defined as 45º S to 60º S, the mid-latitude area is 30º S to 45º S, and the high latitudes are poleward of 60º S.

Using equations previously established (Ganachaud et al., 2000; Stammer et al, 2003; Talley, 2008; Nyadjro et al., 2011), meridional volume transport (F_v) in Sv (10^6 m^3 s^{-1}) is represented as

$$F_v = \int_{-H}^{z_o} \int_0^L v(x,z)dx\,dz \qquad (3.1)$$

where x and z are the zonal and vertical coordinates respectively, H is the water column thickness from the sea surface to ocean bottom (maximum depth of 6134 m), z_o is

the ocean surface, and L is the zonal expanse (m) of the ocean section. v (u) is the meridional (zonal) oceanic velocity in m s^{-1} and is perpendicular to the zonal (meridional) transect. A positive meridional component thus represents a northward velocity. For zonal volume transports, the meridional velocity v in equation (3.1) is replaced with u (the zonal velocity) and the corresponding integral dy. The zonal component is positive for eastward velocity. In estimation of transports, the residual velocity v (u) is the sum of the ECCO-output resolved and bolus velocities, where the bolus component accounts for unresolved eddies. To account for bathymetry, ECCO provides a relative grid thickness factor, which is applied when necessary to account for cells that do not occupy the full nominal thickness.

Both salinity and potential temperature fluxes are integrated to calculate transports from the surface to the ocean bottom (maximum depth of 6134 m) over the 50 depth-layers, accounting for the varying layer thicknesses. In its entirety, volume, salinity, and heat budgets can be evaluated for conservation using the methods depicted in Piecuch (2017). In this analysis, we are using advective and diffusive transports to analyze changes in depth-integrated horizontal net transports. The net salinity and potential temperature transports are the sum of advective and diffusive fluxes that are available individually as ECCO output.

3.2.3. Estimation of Neutral Density

Neutral density (γ^n) is not an ECCO output but was calculated according to the methods of Jackett and McDougall (1997). The advantage over potential density or density anomaly is that neutral density allows for increased accuracy of analysis of isopycnals within the deep ocean. This method is a better characterization of the water masses in the region, such as the CDW, North Atlantic Deep Waters (NADW), and AABW. Neutral

density is estimated for each (x, y, z) grid along depth-layers as a function of time and is used to differentiate the upper and lower cells of the MOC. Monthly residual transports are binned based on the range $\gamma^n \leq 27.72$, $27.72 < \gamma^n \leq 28.11$, and $28.11 < \gamma^n$ (Ganachaud and Wunsch, 2000) that define the three branches of the MOC. These neutral density surfaces represent the Antarctic Intermediate and Subantarctic Mode Waters, CDW, and the AABW for the upper and lower cells of the meridional circulation (Ganachaud and Wunsch, 2000). Comparing transport in density-space, rather than in depth better represents the mean- and eddy-driven components of the MOC and differentiates whether there are significant changes in circulation.

3.2.4. Anomalies and Regression

To estimate anomalies, monthly-mean climatology from ECCO version 4 release 3 (1992-2015) is removed from the monthly record, effectively removing seasonality. The 288-monthly anomalies are used in a least squares linear regression fit (Watson, 1967; Dytham, 2011) to estimate the trends in horizontal transports from 1992 through 2015. To test the hypothesis of no change in transport, an alpha of 0.05 is used to indicate if the regression is significant at the 95% confidence level. Any p-value larger than the alpha level indicates that a trend is not significantly different from zero and thus does not provide evidence to support that a trend exists. Lilliefors Test (Lilliefors, 1967) and Cook's Distance (Cook, 1977) are used to test each horizontal transport for normality and influential data points (leverage) respectively. To test for autocorrelation, Durbin-Watson values are calculated (Durbin and Watson, 1950). The critical values for the Durbin-Watson statistic are 1 and 3, in which most transports show signs of slight positive autocorrelation (between 1 and 2). To account for the slight positive autocorrelation and

few monthly anomalies with large leverage, an additional regression is computed using a non-parametric approach, Sen's slope (Sen, 1968), which is insensitive to outliers and derived using the median. In each instance, both parametric and non-parametric methods produce similar slopes and significance, despite slight autocorrelation and anomalies of large residuals. We discuss our results in terms of the least-squares linear regression statistics, but have included the non-parametric values in the tables due to the potential influence of outliers. The slopes of the least squares linear regression are additionally referred to in units per decade (decade^{-1}). For the regressions that are shown to be significantly different from zero, confidence intervals for the slopes are plus or minus the standard error multiplied by the critical t-value (1.96).

3.3. Results and Discussion

3.3.1. Depth-integrated Volume Transports

ECCO resolves a significant amount of the ocean's variability (shown in Figure 3.1), even for eddy-dominated regions like the SO (Forget et al., 2015; Forget et al., 2016; Fukumori et al., 2017; ECCO Consortium, 2017b). Depth-integrated residual volume transports from the surface to ocean bottom are explored and compared to previous model and *in situ* studies. As we are not balancing budgets (discussed in detail by Piecuch, 2017), only the horizontal transports are analyzed. Within all three basins, the mid-latitude (30º S to 45º S) trends oppose the zonal transports (Figure 3.1). The trends indicate that westward transport is decreasing in the Indian basin and that eastward transport is decreasing in the Pacific and Atlantic basins at the mid-latitudes.

Zonal transports within the ACC (45º S - 45º S) and SO (south of 30º S) are influenced by shifts in the sub-tropical and polar gyres (Wang et al., 2011). Net eastward

zonal transports are significantly decreasing in the central South Atlantic mid-latitude gyre (30º S - 45º S). This is likely influenced by the acceleration and southward shift of the Sub-Tropical Atlantic gyre (Vianna and Menezes, 2011). Similarly, the South Pacific gyre is intensifying and shifting southward (Roemmich and Gilson, 2007; Roemmich et al., 2016). In the Indian basin, ECCO also indicates both meridional boundary currents and zonal basin transports decreasing over time. The opposing trends in the mid-latitude gyre of the Indian basin illustrate deceased horizontal transports that could be a result from a weakening subtropical Indian Ocean gyre, which has previously been shown to decrease seasonally (Ffield et al., 1997). ECCO however shows there are no meridional depth-integrated transport trends in the mid-latitudes and large high latitude variability and trends.

Opposing trends in the north-south extent of the ACC demonstrate narrowing of zonal transports, corroborated in model-based analyses due to the poleward shift in sub-tropical gyres (Wang et al., 2011) and shift in the AAO (Farneti et al., 2015). Both zonal and meridional changes along the Agulhas current denote an opposing trend to the transports, which has been previously described as broadening in the Agulhas (Beal and Elipot, 2016). The meridional depth-integrated transport trends depict changes along the ACC and boundary currents, with significant intensifying Malvinas, Benguela, and East Australian currents.

Figure 3.2 depicts the 24-year time-mean depth- and density-integrated transports and standard deviations across each of the basin boundaries based on monthly means. Within Figure 3.2, positive values depict eastward (zonal) or northward (meridional) transports, while negative values indicate westward or southward transports respectively. ECCO has very similar time-mean transports and variability to other model-based

(Stammer et al., 2003; Mazloff et al., 2010) and observational state estimate studies (MacDonald and Wunsch, 1996; Ganachaud and Wunsch, 2000). The ECCO results are very similar to Mazloff et al. (2010) due to the strong similarities in underlying dynamics and model-physics. Each of the basin transports are directly estimated across the 30° S latitude border and summed along the respective basins' longitude, and net meridional transports from the basins are approximately zero.

In estimating with ECCO, the results are discussed in terms of the horizontal depth-integrated volume transport time-mean and standard deviation from 1992 through 2015. We estimate that the meridional transport through the Bering Strait is 0.9 ± 0.5 Sv and the zonal transport of the Indonesian Throughflow region is -14.0 ± 5.0 Sv. Within ECCO (Figure 3.2), the Atlantic time-mean meridional transport is estimated to be approximately -1.4 ± 0.6 Sv southward. The Indian Ocean provides the SO basins with a net southward transport of -14.4 ± 3.5 Sv, while the Pacific basin has a net northward transport of 15.5 ± 4.1 Sv. The ECCO product has a time-mean net meridional southward transport of -0.30 ± 0.56 Sv at 30° S. Although the entire hydrological cycle is not analyzed (i.e. precipitation, evaporation, and runoff), these meridional transport estimates are similar to Ganachaud and Wunsch (2000) and Stammer et al. (2003). Ganachaud and Wunsch (2000) estimated time-mean meridional transport of -1 Sv in the Atlantic, -16 Sv in the Indian, and 17 Sv in the Pacific basins. Stammer et al. (2003) estimated transports of 0 ± 1.9 Sv in the Atlantic, -11.5 ± 5 Sv in the Indian, and 11.5 ± 4 Sv in the Pacific basins. The variability within ECCO basin transports is indicated within Figures 3.2 and 3.3.

Zonal volume transports estimated from ECCO are similar to those of MacDonald and Wunsch, (1996), Ganachaud and Wunsch (2000), and Mazloff et al. (2010) in

magnitude and variability within the entirety of the region of study. The ECCO time-mean and standard deviation of residual transport within the Drake Passage is calculated to be 148.2 ± 5.4 Sv from 1992-2015. The ECCO time-mean estimate of Drake Passage transports are similar to previous estimates; 153 ± 5 Sv of Mazloff et al. (2010), 142 ± 5 Sv (MacDonald and Wunsch, 1996), and 140 ± 6 Sv (Ganachaud and Wunsch, 2000), but are based on different time periods and depth of integration. ECCO estimated larger transports than an observational study approximation of 134 ± 11 Sv (Cunningham et al., 2003) and model study estimates of 134.9 ± 1 Sv (Sloyan and Rintoul, 2001) and 124 ± 5 Sv (Stammer et al., 2003). ECCO differs from previous Drake Passage estimates based on the depth of integration, resolution, and the temporal-period analyzed. With strong model similarities between ECCO and Mazloff et al. (2010), ECCO estimates the mean Drake Passage transport to be 147.8 ± 5.3 Sv over the same time period (2005-2010). The Mazloff et al. (2010) estimate is greater than that of the ECCO time-mean estimate, but is within one standard deviation. The ECCO Consortium (2017b) found the climatological estimate of mean Drake Passage transport to be 146 Sv (years 1994-2013), where in this analysis ECCO estimated 146.6 ± 5.7 Sv between 1994-2013.

The Drake Passage estimates by ECCO are far below the more recent observational study of 173.3 ± 10.7 Sv (Donohue et al., 2016), suggesting bias in model physics, spatial-temporal differences, or errors associated with observations. Donohue et al. (2016) determined the 2007-2011 mean barotropic transport to be 45.6 Sv and baroclinic transport of 127.7 Sv, totaling 173.3 Sv, which is greater than the maximum ECCO derived transport. The ECCO 2007-2011 mean Drake Passage transport is 146.8 ± 5.5 Sv, outside of three standard deviations from the Donohue et al. (2016) approximation. The Indian-Pacific

passage (referred by the SR3 sampling line) additionally estimated transports similar to previous studies (Ganachaud and Wunsch, 2000; Mazloff et al.,2010). The ECCO estimated SR3 line of 162.6 ± 7.4 Sv is between Ganachaud and Wunsch (2000) estimate of 157 ± 10 Sv and Mazloff et al. (2010) estimate of 164 ± 6 Sv. Over the same time period (2005-2010) as Mazloff et al. (2010), ECCO estimates 161.9 ± 8.1 Sv for the SR3 line. ECCO estimates the time-mean Atlantic-Indian basin exchange to be 150.6 ± 5.5 Sv. To compare with the model-study by Stammer et al. (2003), ECCO estimates the 1993 to 2000 Atlantic-Indian exchange to be 151.7 ± 5.1, greater than their 124 ± 6 Sv approximation.

To analyze the trends of the SO horizontal depth-integrated residual volume transports (Figure 3.3), monthly climatology is removed at each time-step from the transect lines depicted in Figure 3.2. These anomalies reveal a noisy and high frequency pattern (blue), which has been smoothed using a 12-month running mean (black). For meridional and zonal transports, the corresponding statistics using monthly anomalies from Figure 3.3 are found in Table 3.1. Few *in situ* analyses have utilized long-term depth-integrated transports for the SO due to the lack of surface-to-bottom estimations.

Using the ECCO state estimate as a tool, there are no trends significantly different from zero within the depth-integrated zonal and meridional transports at the defined basin boundaries indicated in Figure 3.2. This indicates the trends are statistically insignificant in the SO mean-flow basin transports from 1992 to 2015 (Table 3.1). In the Atlantic, the least squares linear regression slope at 95% confidence interval is 0.0751 ± 0.0947 Sv decade^{-1} ($p = 0.119$), the Indian basin slope is −0.137 ± 0.380 Sv decade^{-1} ($p = 0.479$), and the Pacific basin is 0.215 ± 0.399 Sv decade^{-1} ($p = 0.291$). While regressions indicate similar-facing trends in the Pacific and Indian basins, and an opposing trend in the Atlantic

basin, the p-values are greater than 0.05 and thus the slopes are not significantly different from zero. The statistical analyses therefore present no evidence of a change in the Atlantic MOC or Indo-Pacific transports. Although the trends are approximately zero, the largest variability in the meridional transports exists in the Indian and Pacific basins. This variability is shown through the standard deviations within Figure 3.2 and the standard errors from Table 3.1. Moreover, the Atlantic basin exhibits the lowest variability of meridional transports across 30º S.

In the SO, the ACC dominates zonal transports, with a mean eastward flow. The Drake-Passage, Atlantic-Indian, and Indian-Pacific exchange indicate rates of −0.492 ± 0.778 Sv decade^{-1} ($p = 0.215$), −0.522 ± 0.790 Sv decade^{-1} ($p = 0.195$), and −0.366 ± 0.828 Sv decade^{-1} ($p = 0.385$) respectively. While analyses indicate negative trends (Table 3.1), the p-values indicate the slopes are statistically insignificant and thus present no evidence to support that zonal transports are decreasing with time. The results from Figure 3.3 further indicate that all three zonal basin exchanges have similar variability, shown through the standard errors (Table 3.1).

The time-mean MOC stream function (Figure 3.4a) displays the strong Ekman-driven transport within the SO peaking near 50°S. Each of the overturning cells transports roughly 15 Sv in the meridional component, at the 27.72 kg m^{-3} and 28.11 kg m^{-3} surfaces at 30ºS. The large monthly-variability in the MOC on depth-coordinates (Figure 3.4b) supports using density-coordinates in analysis of volume transports in the SO, further described in Lee and Coward (2003). Near 30º S, the stream function exhibits large variability within the surface to over 3000 m depth, while depths over 4500 m display minimal variability. Comparing the transports of the SO along density coordinates reduces

variability, as the meridional transports are largely associated with isopycnals rather than depth. Within the density-coordinate MOC, there are three distinct branches of overturning separated by the 27.72 kg m^{-3} and 28.11 kg m^{-3} surfaces. Working in density coordinates allows for a more thorough analysis into changes within the water column. To better comprehend and analyze the SO transports, a similar comparison of depth-integrated transports is applied to density-coordinates for the meridional component.

3.3.2. Density-integrated Volume Transports

In comparison of neutral density-integrated transports, ECCO provides similar results to that of both Ganachaud and Wunsch (2000) and Mazloff et al. (2010). Within ECCO (Figure 3.2), the Atlantic basin time-mean northward transport in the top branch is 13.9 ± 2.4 Sv and 1.8 ± 1.5 Sv in the bottom, while southward transport in the middle branch is −17.1 ± 1.4 Sv. In the Pacific basin, the top branch time-mean has a northward transport of 14.1 ± 7.5 Sv and 8.6 ± 3.4 Sv in the bottom, while the middle transports southward at −7.2 ± 3.1 Sv. The Indian basin has southward transports of −14.4 ± 4.0 Sv in the top branch and −4.0 ± 1.7 Sv in the middle, with northward transports of 4.0 ± 4.2 Sv in the bottom.

To account for a temporal variability, Figure 3.5 depicts the meridional climatological monthly anomalies (1992 to 2015), with statistical values in Table 3.2. The Indian, Atlantic, and Pacific basin linear regressions estimate the slope of the meridional transport in the top branch to be −0.395 ± 0.455 Sv $decade^{-1}$ ($p = 0.098$), 0.116 ± 0.251 Sv $decade^{-1}$ ($p = 0.363$), and −0.127 ± 0.557 Sv $decade^{-1}$ ($p = 0.654$) respectively. In each basin, the trend is statistically insignificant for the top branch. The middle branch in all

three basins have p-values that indicate slopes are significantly different from zero. The Atlantic basin middle branch is significantly increasing in southward transport at −0.289 ± 0.160 Sv decade^{-1} ($p < 0.001$), while significantly decreasing 0.878 ± 0.196 Sv decade^{-1} ($p < 0.001$) and 0.436 ± 0.384 Sv decade^{-1} ($p = 0.026$) in net meridional transport within the Indian and Pacific basins respectively. The lower branches of the Atlantic and Indian basins indicate results are statistically significant. The Atlantic basin bottom branch is significantly increasing in northward transport at 2.48 ± 0.172 Sv decade^{-1} ($p = 0.005$); while the Indian is decreasing in northward transport at −0.634 ± 0.336 Sv decade^{-1} ($p < 0.001$). The Pacific basin bottom branch slope is statistically insignificant at −0.0895 ± 0.378 Sv decade^{-1} ($p = 0.642$). For a visual comparison of transports and trends, Figure 3.2 includes the time-mean transports (A) and the trends in transports (B) that are significantly significant.

The temporal analysis of the meridional branches of the overturning cells' transports is used to explore the strength of the global overturning circulation. Within the Atlantic basin, the middle and lower branches are significantly increasing in magnitude at 95% confidence by 0.289 ± 0.160 Sv decade^{-1} (southward) and 0.248 ± 0.172 Sv decade^{-1} (northward). This would indicate a change in the CDW and AABW transports within the Atlantic basin and a statistically significant acceleration of the Atlantic portion of the global MOC lower cell, as both northward and southward transports are increasing trends. From section 3a, the Atlantic meridional transport trends were indicated to be statistically insignificant, whereas when using density to define the circulation, we find that the Atlantic transports are increasing in strength within the defined water masses.

Within the Indian and Pacific basins, the meridional depth-integrated transports are shown to be statistically insignificant; however, using density-integration within the Indian basin, there are significant opposing trends in the middle branch southward transports and the bottom northward transports in the Indian basin. This indicates that there is a deceleration in the net density-defined volume transport in the lower cell of the overturning circulation. The 95% confidence intervals for the middle and bottom branches are 0.878 ± 0.192 Sv decade^{-1} and -0.634 ± 0.336 Sv decade^{-1}, respectively. In the Pacific basin, there is a positive regression in the middle cell, a trend that opposes the southward direction of transports at 0.436 ± 0.384 Sv decade^{-1}. The significant negative trends found in the Indian and Pacific basins could indicate a deceleration in the CDW and AABW of the Indian and Pacific basin circulations, as there is a significant decline in the middle and lower branch transports associated with the global MOC.

In the Atlantic, the largest variability occurs within the top branch of the meridional transports. Moreover, compared to the Pacific and Indian basin meridional transports, the Atlantic has the lowest standard deviations and standard errors in transports. The Indian and Pacific basins similarly indicate the largest variability is within the surface waters, but larger than that of the Atlantic. The Pacific basin has the largest variability in depth- and density-integrated transports and results in large residuals within the linear fit.

3.3.3. Standardized Density-integrated Volume Transports

The statistical results in section 3b indicate significant changes within the density-integrated volume transports. To further analyze the changes within the density classes, the area of each of the three branches of the meridional circulation is used to standardize the

volume transport (Sv m^{-2}). Meridional transports are divided by the area of each branch at 30º S for the Atlantic, Indian, and Pacific basins and units are converted to be in terms of velocity (m s^{-1}). Standardizing the transports into velocity better accounts for variability in the amount of each the three water masses. The results (Figure 3.6, Table 3.3), again, indicate significant changes within the meridional velocities. The Atlantic basin middle branch shows a significantly increasing southward velocity at $-2.56 \pm 1.33 \times 10^{-6}$ Sv m^{-2} $decade^{-1}$ ($p < 0.001$), while the bottom branch shows a significantly increasing northward velocity at $7.61 \pm 5.36 \times 10^{-6}$ Sv m^{-2} $decade^{-1}$ ($p = 0.006$). In section 3b, the slopes of increase within the middle and bottom branches of the Atlantic basin were similar in magnitude, whereas when standardized for area, the bottom branch velocity is increasing nearly three times faster than the middle branch. This difference illustrates the significant increase in the AABW northward transports out of the SO and increase of the lower cell circulation from 1992 to 2015.

The Indian basin demonstrates the middle branch shows significantly decreasing southward velocity at $5.79 \pm 1.56 \times 10^{-6}$ Sv m^{-2} $decade^{-1}$ ($p < 0.001$), while the bottom branch shows a significantly increasing northward velocity at $-12.0 \pm 4.68 \times 10^{-6}$ Sv m^{-2} $decade^{-1}$ ($p < 0.001$). The Pacific basin shows a further decreasing southward velocity in the middle branch at $1.47 \pm 1.38 \times 10^{-6}$ Sv m^{-2} $decade^{-1}$ ($p < 0.037$). These results further imply significant changes within the Indian and Pacific basins, decreasing meridional circulation in the middle and bottom branches of the MOC at 30º S.

Within Figure 3.6 and Table 3.3, the largest variability in each basin exists in the bottom branch of the transports, while the lowest variability exists in the middle branch.

This suggests the circumpolar deep waters maintain relatively low variability in velocity in each basin, while the bottom waters exhibit the greatest variability. Despite changes in the area of transports across 30° S, trends within the Atlantic, Indian, and Pacific basin velocities are significantly changing.

3.3.4. Depth-integrated Temperature and Salt Transports

The meridional transports of potential temperature and salinity and the regression are plotted as a function of latitude between 1992 and 2015 (Figure 3.7 and Table 3.4). The net transport is decomposed into the advective and diffusive components, which account for deviations from the mean. In the SO, there is a net poleward transport of both temperature and salinity. The temperature transports (Figure 3.7a) are mainly driven by advection near the sub–tropical and polar regions, influenced by gyre circulation, but is balanced by both advective and diffusive forces in the ACC region. The decadal trend in temperature transport (Figure 3.7c) shows trends opposing the direction of net, diffusive, and advective transports in the polar region, indicating the transports poleward of 60°S are decreasing. The sub–tropical region indicates increasing gyre transports and the ACC region depicts the southward movement of the maximum advective, net, and diffusive transports of temperature. Salinity transports (Figure 3.7b) are a balance of the advective and diffusive terms, with southward transport throughout the SO. The lowest mean fluxes occur near the sub–tropical and polar gyre, while the greatest difference in the two components appears in the ACC region. The decadal trends (Figure 3.7d) indicate opposing trends to both advective and diffusive components, which relates to increasing southward net transport trend in the sub–tropical and polar regions and decreasing southward net transport in the ACC region.

Regional meridional depth-integrated transports of salinity and temperature are further analyzed (Figure 3.8, Table 3.4). The 95% confidence interval of time–mean temperature transport across 30°S in the Atlantic basin is 70.1 ± 43.3 °C Sv (~0.3 PW) and 70.8 ± 122.3 °C Sv (~0.3 PW) in the Pacific basin. There is a net southward transport of –317.2 ± 73.2 °C Sv (~–1.3 PW) in the Indian basin. The net transport across 30°S is roughly –176.2 ± 197.2 °C Sv (~–0.7 PW), southward into the SO (Figure 3.7a). The ECCO estimates larger temperature transports in the Atlantic and Indian basins than that of Mazloff et al. (2010), but lower values for the Pacific basin, but estimates similar variability to Mazloff et al. (2010). The estimates are similar to those of Ganachaud and Wunsch (2003), Talley (2003), and Zheng and Giese (2009), but larger than those of Stammer et al. (2003) estimates. Estimates of temperature transports for the Atlantic basin by Mazloff et al. (2010) are 99 ± 66 °C Sv and 0.3 ± 2 PW in Ganachaud and Wunsch (2003). The net temperature transport into the Indian and Pacific basins is estimated to be –246.3 ± 172.0 °C Sv, greater than –180.0 ± 210 °C Sv of Mazloff et al. (2010).

The Atlantic and Pacific basin meridional transport trends (Table 3.4) are not significant. The Indian basin, however, is significantly increasing southward transport at a rate of –8.72 ± 4.5 °C Sv decade^{-1} ($p = 0.026$), approximately –0.0358 PW decade^{-1}. The net potential temperature depth-integrated transports across 30° S indicates a significant trend. The 95% confidence level of the meridional trend across 30°S from Figure 3.7a is –15.0 ± 13.5 °C Sv decade^{-1} ($p = 0.030$), approximately –0.0615 PW decade^{-1}. This indicates that there is a significantly positive trend of southward potential temperature transports into

the SO. In this analysis, the results suggest that there is an increasing net potential temperature transport into the SO from 1992 to 2015.

Meridional depth-integrated salinity transports trends are not significant within the SO. The time-mean and standard deviation salinity transport is –32.9 ± 21.7 psu Sv southward in the Atlantic and –509.0 ± 122.4 psu Sv in the Indian basin. The Pacific basin is estimated to be 540.3 ± 140.6 psu Sv northward. The large southward transport of salinity from the Indian basin results from the large-scale evaporation in Indian Ocean (Talley, 2008). The time-mean SO salinity transport across 30° S is –1.7 ± 22.4 psu Sv. The regressions for salinity transports are not significant and we can therefore conclude the net salinity transports across 30°S in the SO are not significantly changing from 1992 to 2015.

3.3.5. Density-integrated Temperature and Salt Transports

Density-integrated salinity and potential temperature transports are further analyzed in a similar manner to that in section 3b. Using ECCO (Figure 3.9 and Table 3.5), the Atlantic basin time-mean and standard deviation northward transport in the top branch is 120.1 ± 47.4 °C Sv and the bottom branch is 0.9 ± 1.6 °C Sv, while southward transport in the middle is −50.9 ± 3.8 °C Sv. The Indian basin has southward transports of −309.3 ± 78.1 °C Sv in the top and −10.3 ± 3.9 °C Sv in the middle branches, with northward transports of 2.5 ± 3.5 °C Sv in the bottom branch. In the Pacific basin, the top branch time-mean has a northward transport of 77.9 ± 127.9 °C Sv and 6.4 ± 2.5 °C Sv in the bottom, while the middle branch transports southward at −13.5 ± 5.5 °C Sv. These values demonstrate the large southward transport of potential temperature within the surface waters of the Indian Ocean and the high variability of the Pacific Ocean surface transports.

Least squares linear regressions indicate significant trends within the SO basins. The Atlantic basin middle branch is increasing southward transports at 95% confidence of –1.86 ± 0.432 °C decade^{-1} ($p < 0.001$) and northward transports in the bottom branch at 0.31 ± 0.19 °C Sv decade^{-1} ($p = 0.001$). The top branch of the Indian basin shows a significant increase in southward transports at –10.29 ± 8.0 °C Sv decade^{-1} ($p = 0.012$), but a decrease of 1.98 ± 0.43 °C Sv decade^{-1} ($p < 0.001$) in the middle branch and northward transports by –0.41 ± 0.28 °C Sv decade^{-1} ($p = 0.004$) in the bottom branch. The middle branch of the Pacific basin indicates a negative trend, decreasing southward transport by 0.80 ± 0.67 °C Sv decade^{-1} ($p = 0.020$). These results agree with section 3b, that there is an acceleration of transports in the middle and bottom branches of the Atlantic and decline in the Indian and Pacific basins. However, the upper branch of the Indian basin significant increase of southward transports of potential temperature, driving changes to the energy balance of the SO.

The Atlantic basin time-mean northward salinity transport (Figure 3.10 and Table 3.5) in the top branch is 486.0 ± 84.6 psu Sv and the bottom branch is 71.9 ± 51.6 psu Sv, while southward transport in the middle branch is −590.9 ± 48.2 psu Sv. The Indian basin has southward salinity transports of −511.4 ± 141.1 psu Sv in the top and −141.7 ± 58.0 psu Sv in the middle branch, with northward transports of 143.5 ± 143.9 psu Sv in the bottom branch. In the Pacific basin, the top branch time-mean has a northward salinity transport of 474.4 ± 260.2 psu Sv and 299.7 ± 116.5 psu Sv in the bottom, while the middle branch transports southward at −234.0 ± 105.4 psu Sv.

In each basin, the top branch has slopes that are not significant and thus have no linear trends in salinity transports. The Atlantic basin middle branch shows an increasing southward transport at a rate of –10.26 ± 5.5 psu Sv decade^{-1} ($p < 0.001$) and northward transports in the bottom at 8.06 ± 5.4 psu Sv decade^{-1} ($p = 0.008$). The middle branch of the Indian basin is significantly decreasing in southward transports at 30.43 ± 6.8 psu Sv decade^{-1} ($p < 0.001$) and the bottom branch northward transports by–23.03 ± 11.6 psu Sv decade^{-1} ($p < 0.001$). The middle branch of the Pacific basin shows decreasing southward transport by 14.76 ± 13.2 psu Sv decade^{-1} ($p = 0.028$). Similar to the transports in section 3b, the density-integrated salinity transports support increasing circulation within the middle and bottom branches in the Atlantic and decreasing within the Indian and Pacific cells.

3.3.6. Mechanisms for Density-integrated Transport Changes

Salinity, temperature, and density trends are estimated through a least squares linear fit of the climatological anomalies, removing seasonality (Figure 3.11). Long-term decadal changes in the SO's temperature and salinity have been previously shown (Gille, 2002; Gille, 2008; Durack and Wijffels, 2010). These results demonstrate broad-scale warming throughout much of the mid-latitudes in all three basins and the high latitudes of the Atlantic and Indian Ocean basins, while cooling in much of the ACC regions of the Atlantic and Indian basins and poleward of 50º S in the Pacific basin. The high latitude warming in the Atlantic and Indian basins reach depths near 4000 m, far below the surface.

Within the Atlantic and Indian basins, salinity trends correspond to similar regions and magnitudes as temperature trends, although greater trends within the high latitude

bottom waters. The Pacific basin illustrates broad-scale freshening throughout much of the surface SO, while increasing salinity in the high latitudes. Compared to the other basins, the bottom waters in the Pacific have weaker trends that are not significant. Our results show there are large-scale changes in temperature and salinity values from the surface to the ocean bottom within the Indian and Atlantic basins, while only significant changes within the surface 1000 m of the Pacific basin.

In both the Atlantic and Indian basins, similar high latitude regions illustrate a positive trend in temperature and a negative trend in density, despite a significant increase in salinity. Outside the surface waters and the high latitude Pacific basins, much of the changes in density correspond with changes in temperature. This is important to consider as both the Indian and Pacific basins' CDW potential temperature trends imply a decrease in temperature transports out of the SO, but ECCO further indicates decreasing temperatures and increasing densities within the middle branch of the basins. Within the Indian basin at 30º S, the bottom branch shows significant increasing in temperatures and decrease in densities. Moreover, changes in density are statistically significant along the region of the 28.11 kg m^{-3} time-mean isopycnal, which indicates water masses are changing density over time. Each basin indicates significant changes of density in regions around the 27.72 kg m^{-3} and 28.11 kg m^{-3} time-mean isopycnals (Figure 3.12), except the 28.11 kg m^{-3} neutral density surface in the Atlantic. These results imply a significant increase within the area of intermediate and mode waters of all three basins and within AABW of the Pacific and Indian basins at 30º S. Moreover, there is a significant decrease in the area of the CDW within all three basins.

The change in density classes may drive the decrease in the density-integrated transports within the Indian and Pacific basins. However, when standardizing for area of each density class, the meridional transports within the middle and bottom branches are shown to be decreasing. This could be as a result from changes in the amount of each water mass class or a proxy of circulation changes. The Atlantic basin poses a more interesting result, where the AABW is the only branch to not have a significant trend. This implies the area across 30º S that AABW is transported in the Atlantic basin is not significantly changing between 1992 – 2015. Our analysis indicates the lower branch of the Atlantic MOC is accelerating, while the Indian and Pacific basins are decreasing in transports.

3.4. Conclusion

Through the use of ECCO, the SO variability and trends of depth- and density-integrated zonal and meridional transports are examined throughout a 24-year period. Zonal transports between all three basins are statistically insignificant. The net Drake Passage volume transport is estimated to be 148.2 ± 5.3 Sv, the Atlantic-Indian basin transport is 150.6 ± 5.5 Sv, and Indian-Pacific is 162.6 ± 7.4 Sv. Similar values are found in many previous studies (i.e. Ganachaud and Wunsch, 2000; Mazloff et al., 2010), but are larger than previous observational analyses (i.e. Stammer et al., 2003). We have expanded on these results to show trends in net zonal transports are not significantly different from zero between the SO basins from 1992 to 2015. The depth-integrated meridional transport trends are further not statistically different from zero. The Indian basin has net southward transport of -14.4 ± 3.5 Sv, the Pacific basin net northward transport of 15.5 ± 4.1 Sv, and the Atlantic basin estimated -1.4 ± 0.6 Sv southward. Initial results indicate that there are

no significant changes within the Atlantic MOC transports or the Indian and Pacific sector of the MOC.

The meridional transports were further separated into the upper, middle, and lower branches of the MOC by density classes to provide a more accurate representation of the meridional transports. Our estimates of the various transports are within reason with regard to previous studies, but include transport trends. The Atlantic basin time-mean transports are 13.9 ± 2.4 Sv, -17.1 ± 1.4 Sv, and 1.8 ± 1.5 Sv for the top, middle, and bottom branches, respectively. The Indian basin time-mean meridional transports are -14.4 ± 4.0 Sv, -4.0 ± 1.7 Sv, 4.0 ± 4.2 Sv and 14.1 ± 7.5 Sv, -7.2 ± 3.1 Sv, and 8.6 ± 3.4 Sv in the Pacific. Trends in the Atlantic basin indicate a significant acceleration in the bottom branch northward transports (0.248 ± 0.172 Sv decade^{-1}) and the middle branch southward transports (−0.289 ± 0.160 Sv decade^{-1}). The area of the density classes further implies the bottom water area across 30º S is not significantly changing over time. The estimated trends indicate a significant increase in the Atlantic basin lower cell overturning within the SO, as CDW and AABW transports are increasing within a consistent area.

The acceleration in the South Atlantic is opposed by the Indian and Pacific sector. The Indian and Pacific basin branches of the MOC have trends that oppose the direction of transport, significantly decreasing by 0.878 ± 0.196 Sv decade^{-1} and 0.436 ± 0.384 Sv decade^{-1} in the middle, respectively, and −0.634 ± 0.336 Sv decade^{-1} in the lower branch of the Indian basin. However, analysis of the area implies a decrease in the area of CDW and increase in AABW, where the water masses could be switching the defined density classes to reduce transports. The opposing water mass trends indicate a significant

deceleration in the lower cell water transport in the Indian and Pacific basins, but could further be an artifact of the changing density classes.

The SO potential temperature and salinity transports are analyzed through the advective and diffusive components. Temperature transport trends indicate increased potential temperature being transported southward across 30º S, increasing the right-hand side of the budget estimation. Potential temperature transports are mainly influenced by the gyres in the polar and subtropical regions mean-flow but are strongly influenced by the eddy-component in the ACC region. Furthermore, the trends in the ACC region indicate a narrowing and southward shift of the eastward transports. Salinity transports are largely influenced by both mean-flow and diffusive properties at any given latitude but having opposing trends in both the advective and diffusive components. The Indian basin is significantly increasing net southward transports of potential temperature at a rate of –8.72 ± 4.5 °C Sv decade^{-1} and combined there is an increasing trend of potential temperature transports into the SO at –15.0 ± 13.5 °C Sv decade^{-1}. This indicates that the temperature transports are significantly increasing within the SO between 1992 to 2015, but there are no significant trends in the SO salinity transports.

The time-mean ECCO transports are consistent with many previous model-based and state-estimates, but are shown to estimate larger zonal transports than observational analyses. Through the use of ECCO, we find that the Atlantic MOC in the SO is accelerating, while the Indo-Pacific MOC is decreasing. Meridional transport trends additionally estimate significant changes in boundary current transports but could further be linked to a shift in mid-latitude gyres. The initial hypothesis is that ECCO supports decreasing zonal and meridional depth-integrated transports in the SO. Monitoring and

studying the exchange and transports of volume, heat, and salt all relate back to general circulation and the importance of the global MOC. Since the SO plays a fundamental role in balancing the downwelling waters of the North Atlantic, continuous monitoring of the SO MOC and ACC would allow for a better understanding of earth's climate and advancing model potency.

Table 3.1. Statistics from Figure 3.3, the time-mean and regression of meridional and zonal depth-integrated climatological anomalies in volume transport from 1992-2015 in ECCO V4r3. An alpha of 0.05 is used to determine significance.

		Mean (Sv)	Standard Deviation	Regression in Sv month^{-1}	Confidence Interval	p-value	Standard Error	Adjusted R^2	Durbin-Watson	Sen's Slope in Sv month^{-1}	p-value
Meridional	*Atlantic*	-1.4	0.6	6.26E-04	7.89E-04	0.119	4.01E-04	5.00E-03	2.02	5.83E-04	0.143
	Indian	-14.4	3.5	-1.14E-03	3.17E-03	0.479	1.61E-03	-1.70E-03	1.48	-1.39E-03	0.374
	Pacific	15.5	4.1	1.79E-03	3.33E-03	0.291	1.69E-03	4.00E-04	1.52	1.84E-03	0.306
Zonal	*Pacific-Atlantic*	148.2	5.4	-4.10E-03	6.49E-03	0.215	3.30E-03	1.90E-03	1.25	-5.21E-03	0.123
	Atlantic-Indian	150.6	5.5	-4.35E-03	6.59E-03	0.195	3.35E-03	2.40E-03	1.26	-5.55E-03	0.111
	Indian-Pacific	162.6	7.4	-3.05E-03	6.90E-03	0.385	3.50E-03	-8.00E-04	1.35	-5.82E-03	0.095

Table 3.2. Statistics from Figure 3.5, the time-mean and regression of the density-integrated climatological anomalies in meridional volume transport from 1992-2015 in ECCO V4r3. An alpha of 0.05 is used to determine significance.

		Mean (Sv)	Standard Deviation	Regression (Sv month^{-1})	Confidence Interval	p-value	Standard Error	Adjusted R^2	Durbin-Watson	Sen's Slope (Sv month^{-1})	p-value
Atlantic	*Upper*	13.9	2.4	9.68E-04	2.09E-03	0.363	1.06E-03	-6.00E-04	1.74	1.02E-03	0.349
	Middle	-17.1	1.4	-2.41E-03	1.33E-03	< 0.001	6.78E-04	3.89E-02	1.76	-2.22E-03	0.001
	Lower	1.8	1.5	2.06E-03	1.43E-03	0.005	7.27E-04	2.40E-02	1.89	2.02E-03	0.006
Indian	*Upper*	-14.4	4.0	-3.29E-03	3.79E-03	0.089	1.93E-03	6.60E-03	1.12	-2.61E-03	0.171
	Middle	-4.0	1.7	7.32E-03	1.63E-03	< 0.001	8.28E-04	0.212	1.38	7.20E-03	< 0.001
	Lower	4.0	4.2	-5.28E-03	2.80E-03	< 0.001	1.42E-03	4.27E-02	1.18	-5.96E-03	< 0.001
Pacific	*Upper*	14.1	7.5	-1.06E-03	4.64E-03	0.654	2.36E-03	-2.80E-03	1.82	-6.55E-04	0.774
	Middle	-7.2	3.1	3.64E-03	3.20E-03	0.026	1.63E-03	1.37E-02	2.06	3.02E-03	0.071
	Lower	8.6	3.4	-7.46E-04	3.15E-03	0.642	1.60E-03	-2.70E-03	1.83	-1.11E-03	0.503

Table 3.3. Statistics from Figure 3.6, the time-mean and regression of the density-integrated climatological anomalies in meridional volume transport standardized by area between 1992-2015 in ECCO V4r3. An alpha of 0.05 is used to determine significance.

		Mean ($m\ s^{-1}$)	Standard Deviation	Regression ($m\ s^{-1}\ month^{-1}$)	Confidence Interval	p-value	Standard Error	Adjusted R^2	Durbin-Watson	Sen's Slope ($m\ s^{-1}\ month^{-1}$)	p-value
Atlantic	*Upper*	167.7	28.5	9.51×10^{-3}	0.025	0.458	1.28×10^{-2}	-1.60×10^{-3}	1.74	1.00×10^{-2}	0.449
	Middle	-142.1	11.6	-2.14×10^{-2}	0.011	< 0.001	5.64×10^{-3}	4.43×10^{-2}	1.74	-1.96×10^{-2}	0.001
	Lower	54.6	46.8	6.34×10^{-2}	0.045	0.006	2.27×10^{-2}	2.31×10^{-2}	1.88	6.19×10^{-2}	0.007
Indian	*Upper*	-119.6	33.0	-2.30×10^{-2}	0.031	0.1517	1.60×10^{-2}	3.70×10^{-3}	1.12	-1.73×10^{-2}	0.273
	Middle	-31.7	13.1	4.83×10^{-2}	0.013	< 0.001	6.60×10^{-3}	0.154	1.36	4.67×10^{-2}	<0.001
	Lower	56.3	58.1	-1.00×10^{-1}	0.039	< 0.001	1.98×10^{-2}	7.86×10^{-2}	1.16	-1.11×10^{-1}	<0.001
Pacific	*Upper*	74.6	39.4	-7.86×10^{-3}	0.025	0.5282	1.24×10^{-2}	-2.10×10^{-3}	1.81	-5.27×10^{-3}	0.657
	Middle	-25.9	11.1	1.23×10^{-2}	0.012	0.037	5.86×10^{-3}	1.17×10^{-2}	2.07	1.01×10^{-2}	0.091
	Lower	146.9	57.7	-2.02×10^{-2}	0.054	0.458	2.72×10^{-2}	-1.60×10^{-3}	1.85	-2.60×10^{-2}	0.324

Table 3.4. Statistics from Figures 3.7 and 3.8 for 30º S, the time-mean and regression of meridional depth-integrated potential temperature (ºC Sv) and salinity (psu Sv) transports from 1992-2015 in ECCO V4r3. An alpha of 0.05 is used to determine significance.

		Mean	Standard Deviation	Regression (month^{-1})	Confidence Interval	p-value	Standard Error	Adjusted R^2	Durbin-Watson	Sen's Slope (month^{-1})	p-value
Potential Temperature	*Southern Ocean*	-176.2	197.2	-0.125	0.113	0.030	5.72E-02	0.013	1.63	-0.126	0.032
	Atlantic	70.1	43.3	9.72E-03	0.0374	0.609	1.90E-02	-2.58E-03	1.78	1.17E-02	0.531
	Indian	-317.2	73.2	-7.27E-02	0.0638	0.026	3.24E-02	1.38E-02	1.13	-6.48E-02	0.046
	Pacific	70.8	122.3	-6.21E-02	0.0810	0.132	4.11E-02	4.43E-03	1.93	-5.23E-02	0.183
Salinity	*Southern Ocean*	-1.7	22.4	-4.31E-03	0.0313	0.787	1.59E-02	-3.24E-03	1.04	-4.34E-03	0.631
	Atlantic	-32.9	21.7	1.70E-02	0.0275	0.223	1.40E-02	1.71E-03	2.02	1.58E-02	0.299
	Indian	-509.0	122.4	-5.50E-02	0.111	0.329	5.63E-02	-1.53E-04	1.47	-6.43E-02	0.253
	Pacific	540.3	140.6	3.23E-02	0.114	0.576	5.77E-02	-2.40E-03	1.53	3.32E-02	0.582

Table 3.5. Statistics from the time-means monthly anomalies in Figures 3.9 and 3.10, the regression of meridional depth-integrated potential temperature (ºC Sv) and salinity (psu Sv) transports from 1992-2015 in ECCO V4r3 at 30° S. An alpha of 0.05 is used to determine significance.

			Mean	Standard Deviation	Regression (month^{-1})	Confidence Interval	p-value	Standard Error	Adjusted R^2	Durbin-Watson	Sen's Slope (month^{-1})	p-value
Potential Temperature	*Atlantic*	*Upper*	120.1	47.4	2.26E-02	4.04E-02	0.271	2.05E-02	7.00E-04	1.78	2.48E-02	0.230
		Middle	-50.9	3.8	-1.55E-02	3.60E-03	< 0.001	1.83E-03	1.98E-01	1.69	-1.49E-02	< 0.001
		Lower	0.9	1.6	2.61E-03	1.57E-03	0.001	7.97E-04	3.27E-02	1.94	2.22E-03	0.005
	Indian	*Upper*	-309.3	78.1	-8.58E-02	6.66E-02	0.012	3.39E-02	1.85E-02	1.12	-7.72E-02	0.020
		Middle	-10.3	3.9	1.65E-02	3.57E-03	< 0.001	1.81E-03	0.221	1.36	1.62E-02	< 0.001
		Lower	2.5	3.5	-3.42E-03	2.34E-03	0.004	1.19E-03	2.46E-02	1.14	-4.04E-03	0.001
	Pacific	*Upper*	77.9	127.9	-6.87E-02	8.62E-02	0.118	4.38E-02	5.10E-03	1.93	-5.71E-02	0.159
		Middle	-13.5	5.5	6.67E-03	5.60E-03	0.020	2.84E-03	1.55E-02	2.05	5.56E-03	0.052
		Lower	6.4	2.5	1.50E-05	2.38E-03	0.990	1.21E-03	-3.50E-03	1.86	-1.68E-04	0.883
Salinity	*Atlantic*	*Upper*	486.0	84.6	3.54E-02	7.48E-02	0.352	3.80E-02	-5.00E-04	1.74	3.80E-02	0.337
		Middle	-590.9	48.2	-8.55E-02	4.61E-02	< 0.001	2.34E-02	4.12E-02	1.76	-7.90E-02	0.001
		Lower	71.9	51.6	6.72E-02	4.91E-02	0.008	2.50E-02	2.13E-02	1.91	6.49E-02	0.009
	Indian	*Upper*	-511.4	141.1	-1.21E-01	1.34E-01	0.079	6.83E-02	7.30E-03	1.12	-9.53E-02	0.156
		Middle	-141.7	58.0	2.54E-01	5.66E-02	< 0.001	2.87E-02	0.211	1.38	2.49E-01	< 0.001
		Lower	143.5	143.9	-1.92E-01	9.69E-02	< 0.001	4.92E-02	4.71E-02	1.18	-2.14E-01	< 0.001
	Pacific	*Upper*	474.4	260.2	-4.50E-02	1.62E-01	0.586	8.24E-02	-2.50E-03	1.82	-2.93E-02	0.707
		Middle	-234.0	105.4	1.23E-01	1.10E-01	0.028	5.58E-02	1.33E-02	2.07	1.02E-01	0.075
		Lower	299.7	116.5	-4.42E-02	1.09E-01	0.424	5.52E-02	-1.30E-03	1.85	-5.89E-02	0.307

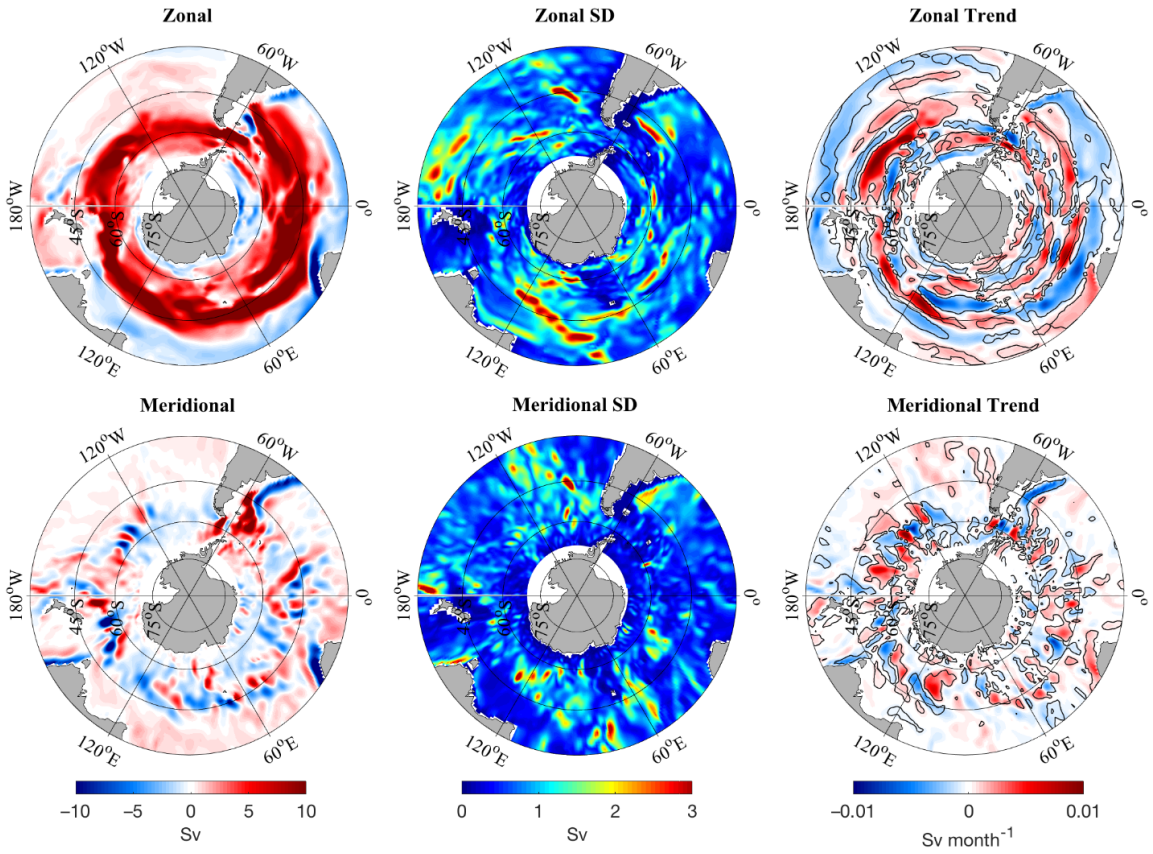

Figure 3.1. ECCO V4r3 (1992-2015) time-mean (Sv), standard deviation (SD; Sv), and coefficients of regression (Sv month^{-1}) of zonal and meridional depth-integrated volume transports for the Southern Ocean. Zonal (meridional) transports in red depict an eastward (northward) direction. The coefficients of regression are computed spatially with zonal and meridional depth-integrated transport in units of Sv per month (Figure 3.1c and 1f). The linear regressions significant under an alpha of 0.05 are contoured in black.

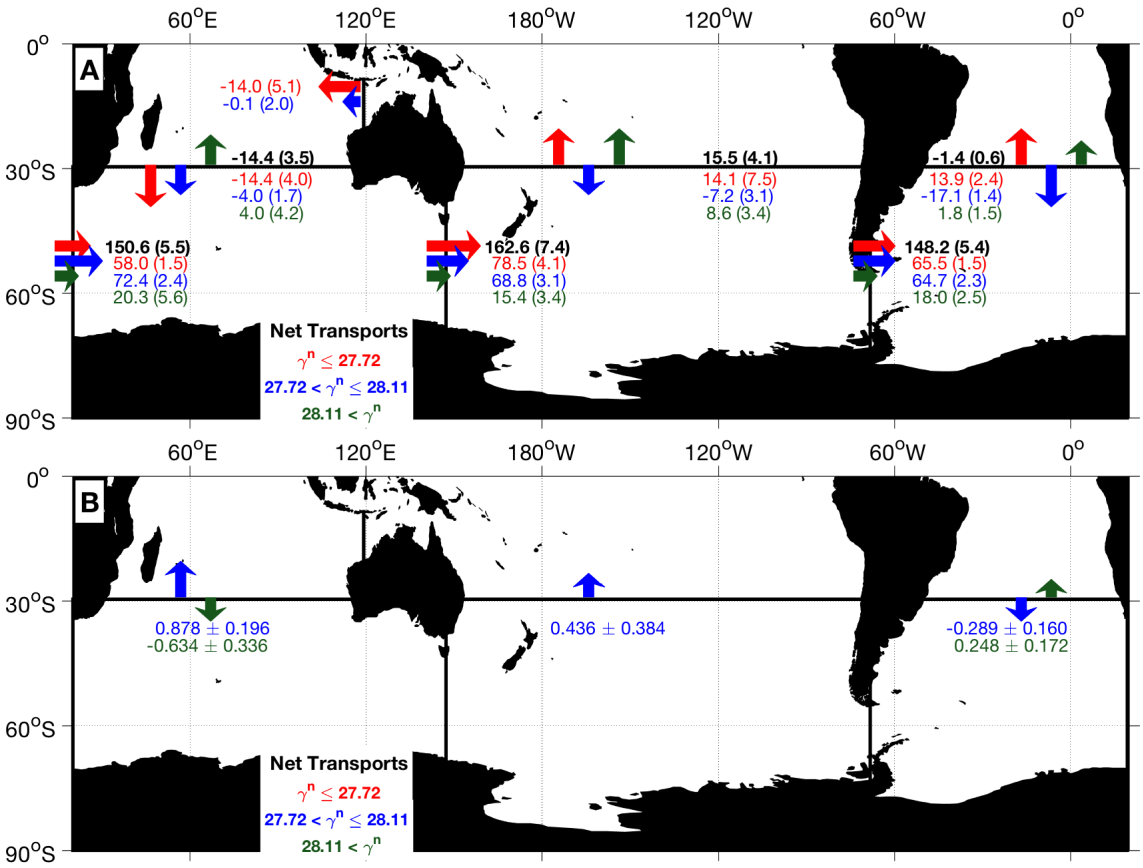

Figure 3.2. (A) ECCO's 24-year time-mean depth-integrated residual volume transports (Sv) and monthly standard deviations (in parenthesis) across each of the basins. (B) The slopes and 95% confidence intervals (Sv decade^{-1}) for the least-squares linear regression of the 288-monthly anomalies that are statistically significant. Red ($\gamma^n \leq 27.72$ kg m^{-3}) represents the surface and mode waters, blue (27.72 kg m^{-3} $< \gamma^n \leq$ 28.11 kg m^{-3}) the circumpolar deep waters, and green ($\gamma^n >$ 28.11 kg m^{-3}) the Antarctic bottom water. The Atlantic-Indian Oceans border is defined as 20° E, the Indian-Pacific border at 145° E, and the Pacific-Atlantic border at 70° W. The meridional transport is estimated across 30° S. Estimates for the meridional transport through the Bering Strait is 0.9 ± 0.5 Sv from the Pacific to the Atlantic Ocean.

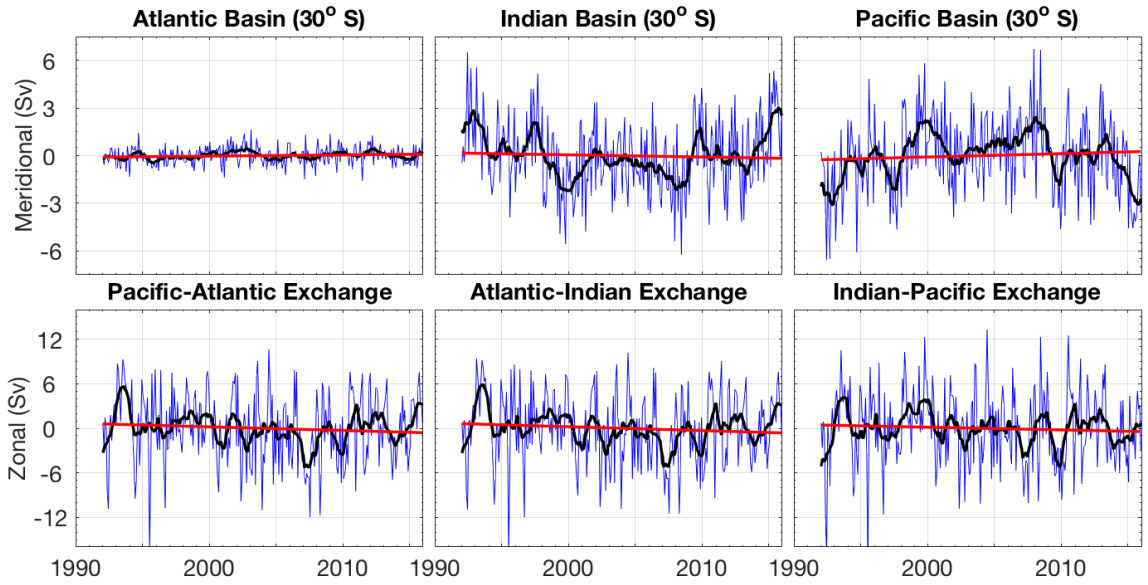

Figure 3.3. Monthly climatological anomalies of depth-integrated transports (blue), 12-month running mean (black), least-squares regression line (red), and Sen's slope regression line (dotted). The associated statistics are found in Table 3.1. The Atlantic-Indian Oceans border is defined as 20° E, the Indian-Pacific border at 145° E, and the Pacific-Atlantic border at 70° W. The meridional transport is estimated across 30° S.

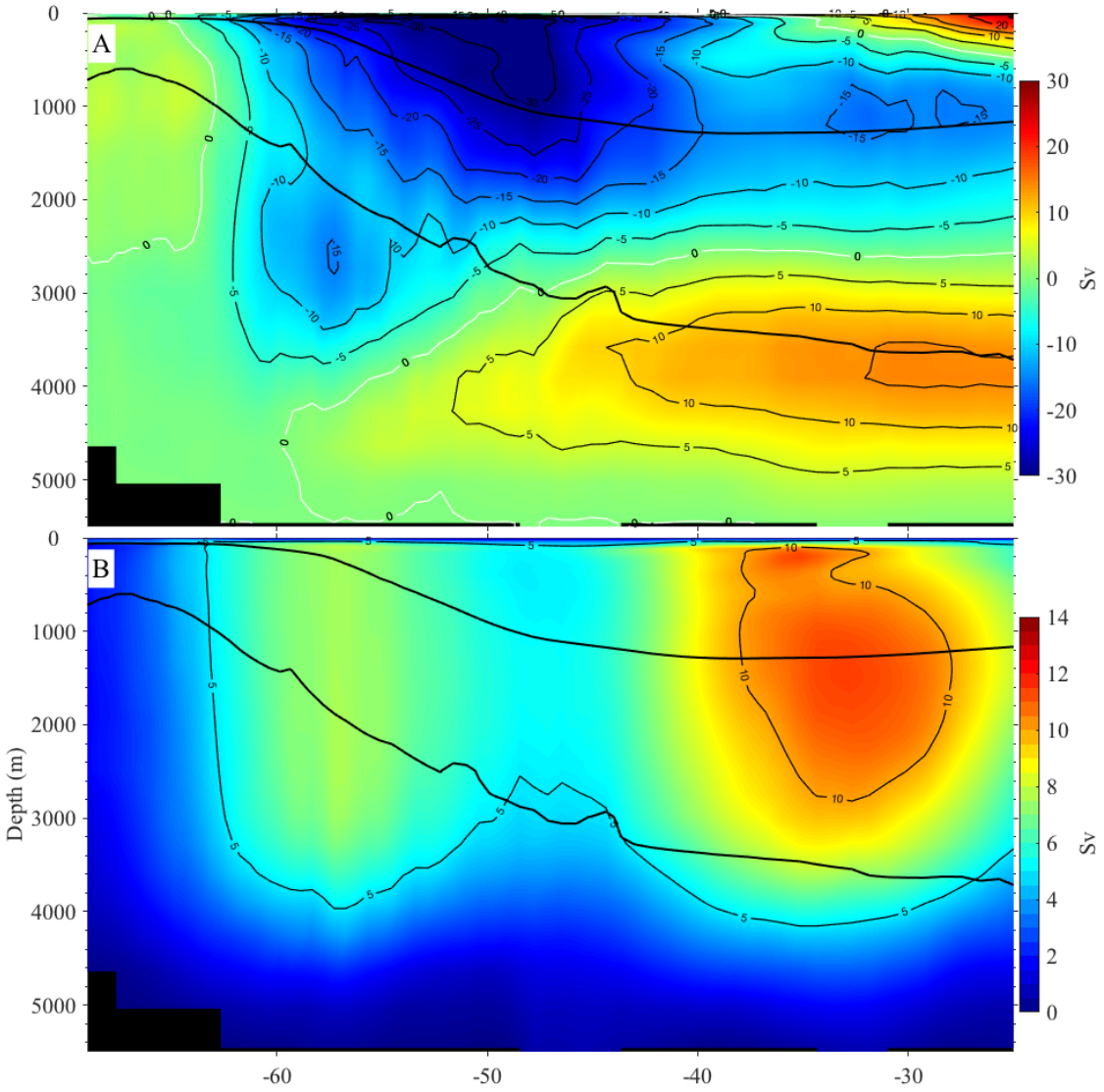

Figure 3.4. Time-mean Southern Ocean overturning stream function (A) between 25° S and 70° S. Positive (negative) values denote counterclockwise (clockwise) circulation. The standard deviation (B) is estimated for the entire 288-month state estimate. The black lines are the 27.72 kg m^{-3} and 28.11 kg m^{-3} neutral density surfaces to depict the branches of the two global meridional overturning cells.

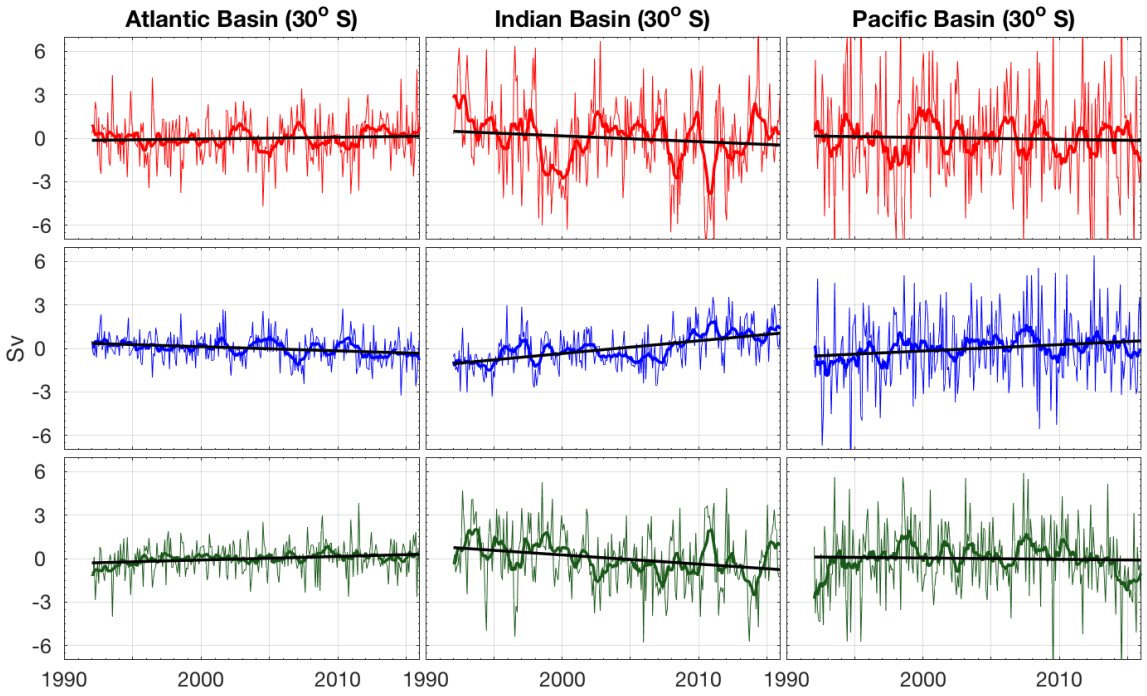

Figure 3.5. Monthly climatological anomalies of neutral density-integrated meridional transports, the 12-month running mean (bold), and regression line (black). The statistics for Figure 3.5 are found in Table 3.2. Red represents the upper, blue the middle, and green the bottom branch of the overturning circulation. The meridional transport is estimated across 30° S and binned based on 27.72 kg m^{-3} and 28.11 kg m^{-3} neutral density surfaces.

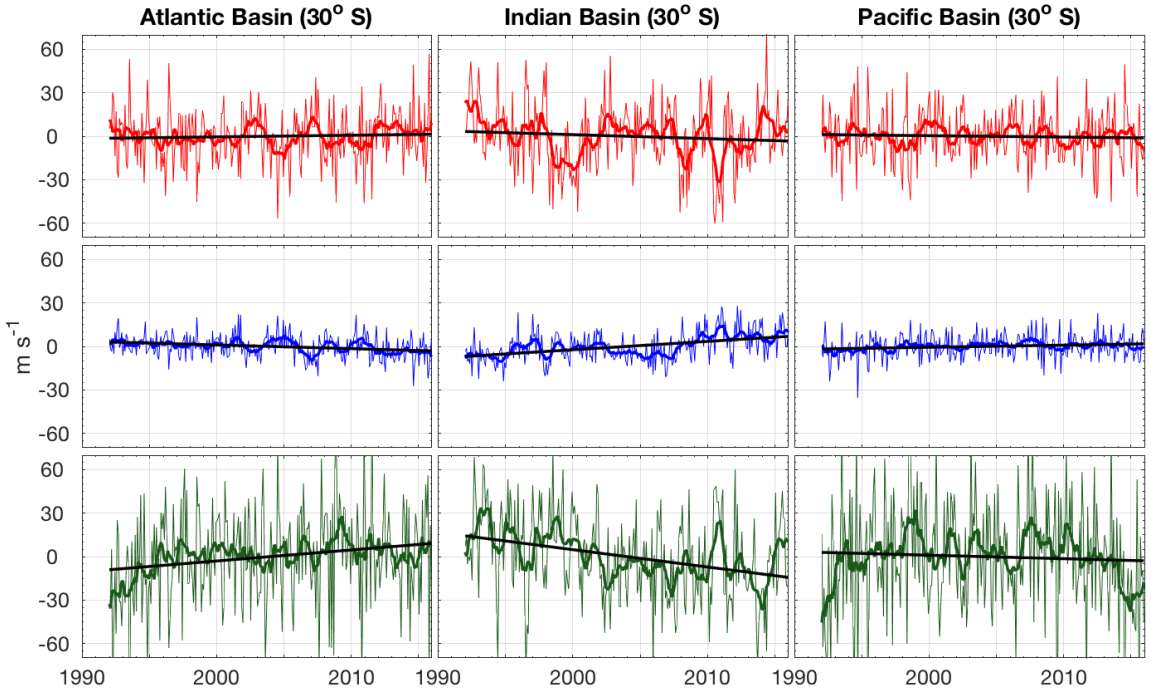

Figure 3.6. Monthly climatological anomalies of net meridional velocity by density class at 30°S (transports standardized by the area), the 12-month running mean (bold), and regression line (black). The statistics for Figure 3.6 are found in Table 3.3. Red represents the upper, blue the middle, and green the bottom branch of the overturning circulation; binned based on 27.72 kg m^{-3} and 28.11 kg m^{-3} neutral density surfaces.

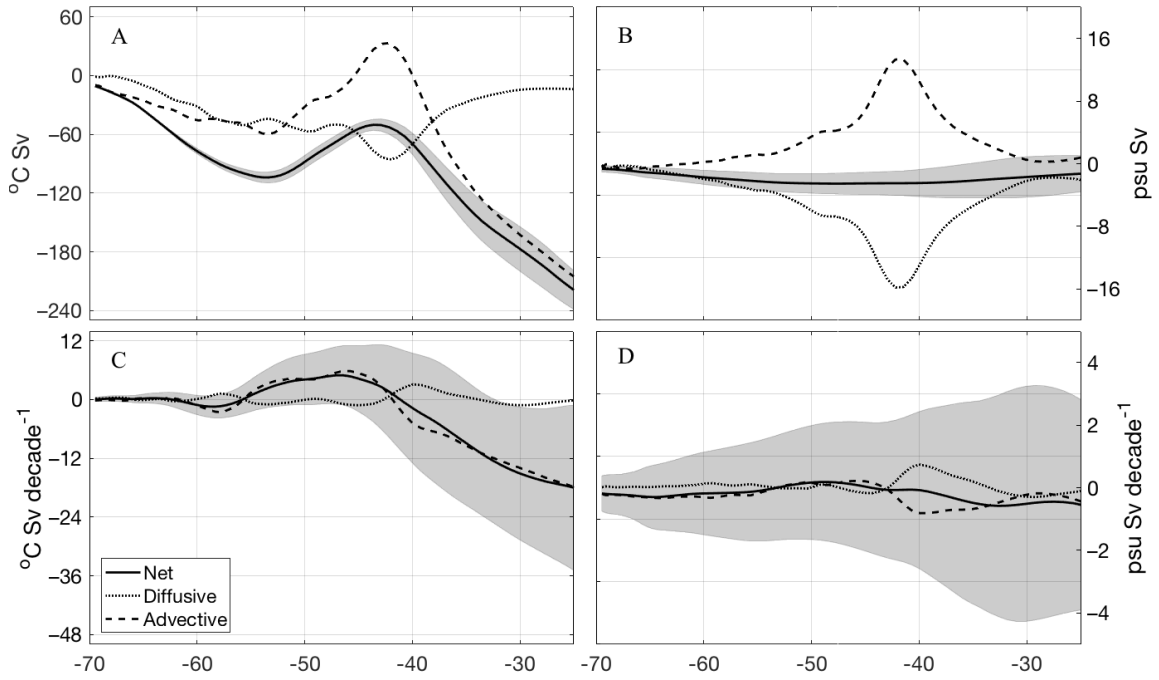

Figure 3.7. Time-mean net, diffusive, and advective potential temperature (a) and salinity (b) transports for the Southern Ocean, with the net time-mean outlined with the 95% confidence interval. Positive values are northward and negative values are southward transports. Plots (c) and (d) depict the monthly-time regression (in units of per decade) for each net, diffusive, and advective components. The net trend is contoured with the 95% confidence interval. Trends relate to the transports, where positive values indicate increasing northward transport or weakening southward flow.

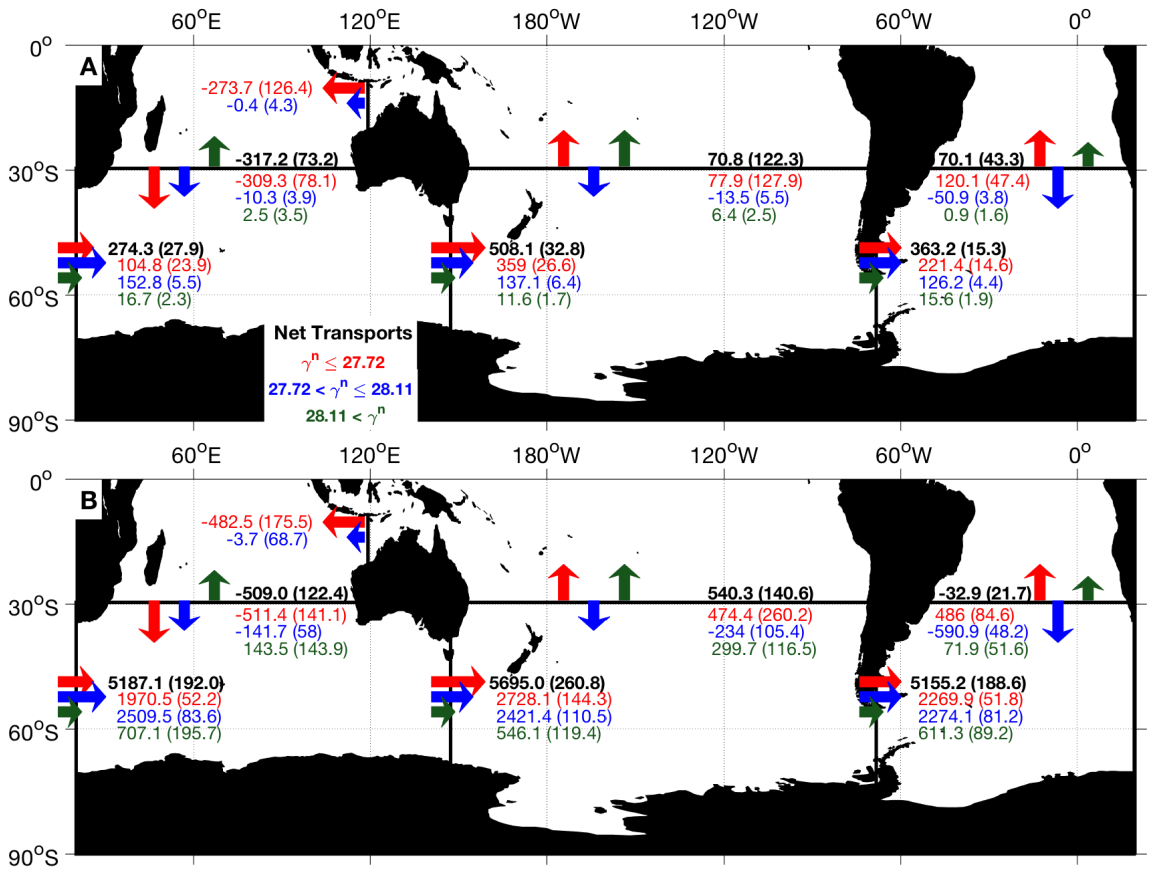

Figure 3.8. ECCO's 24-year time-mean depth-integrated net potential temperature (a) salinity (b) transports and monthly standard deviations (in parenthesis) across each of the basins. Units for potential temperature transport are in ºC Sv and salinity transports are in psu Sv. Red ($\gamma^n \leq 27.72$ kg m^{-3}) represents the surface and mode waters, blue (27.72 kg m$^{-3} < \gamma^n \leq 28.11$ kg m^{-3}) the circumpolar deep waters, and green ($\gamma^n > 28.11$ kg m^{-3}) the Antarctic bottom water. The Atlantic-Indian Oceans border is defined as 20° E, the Indian-Pacific border at 145° E, and the Pacific-Atlantic border at 70° W. The meridional transport is estimated across 30° S. Estimates for the meridional transport through the Bering Strait is 0.9 ± 0.5 Sv from the Pacific to the Atlantic Ocean.

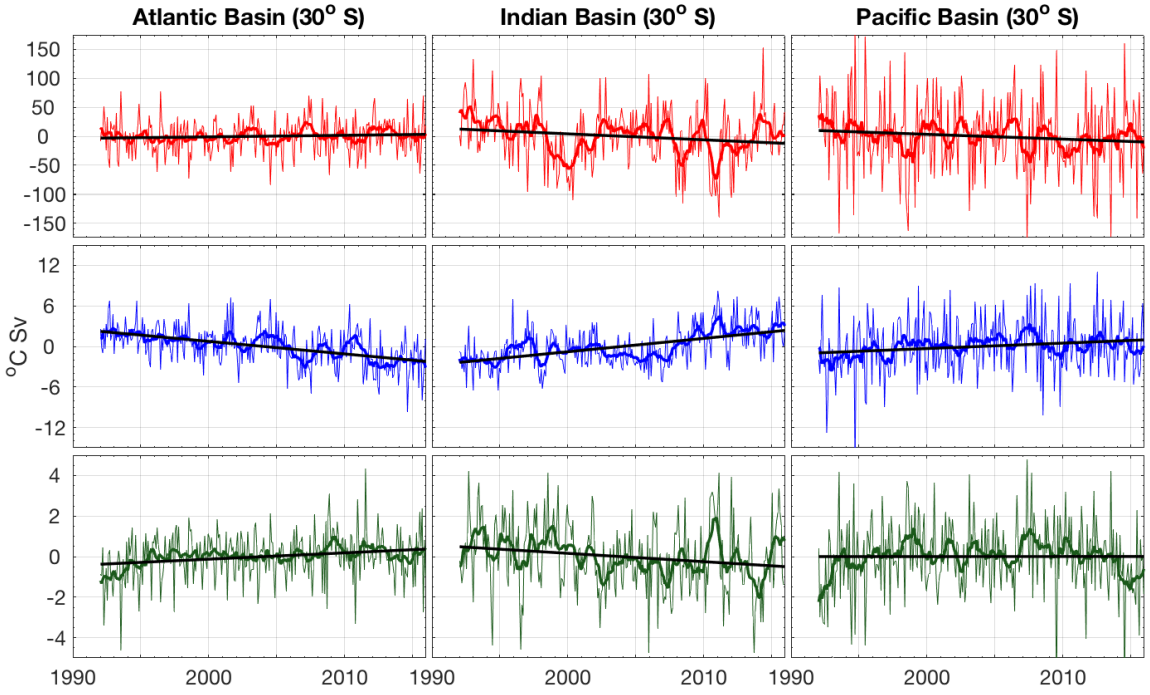

Figure 3.9. Monthly climatological anomalies of neutral density-integrated meridional temperature transports, the 12-month running mean (bold), and regression line (black). The statistics for Figure 3.9 are found in Table 3.5. Red represents the upper, blue the middle, and green the bottom branch. The meridional transport is estimated across 30° S and binned based on 27.72 kg m^{-3} and 28.11 kg m^{-3} neutral density surfaces.

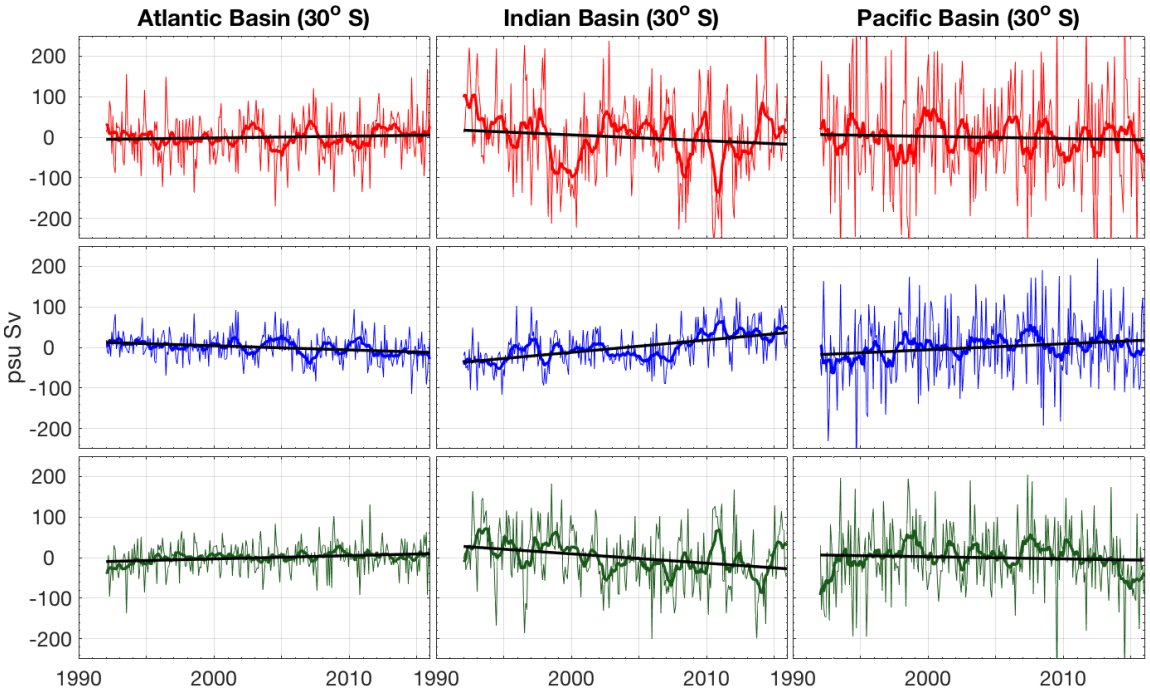

Figure 3.10. Monthly climatological anomalies of neutral density-integrated meridional salinity transports, the 12-month running mean (bold), and regression line (black). The statistics for Figure 3.10 are found in Table 3.5. Red represents the upper, blue the middle, and green the bottom branch. The meridional transport is estimated across 30° S and binned based on 27.72 kg m^{-3} and 28.11 kg m^{-3} neutral density surfaces.

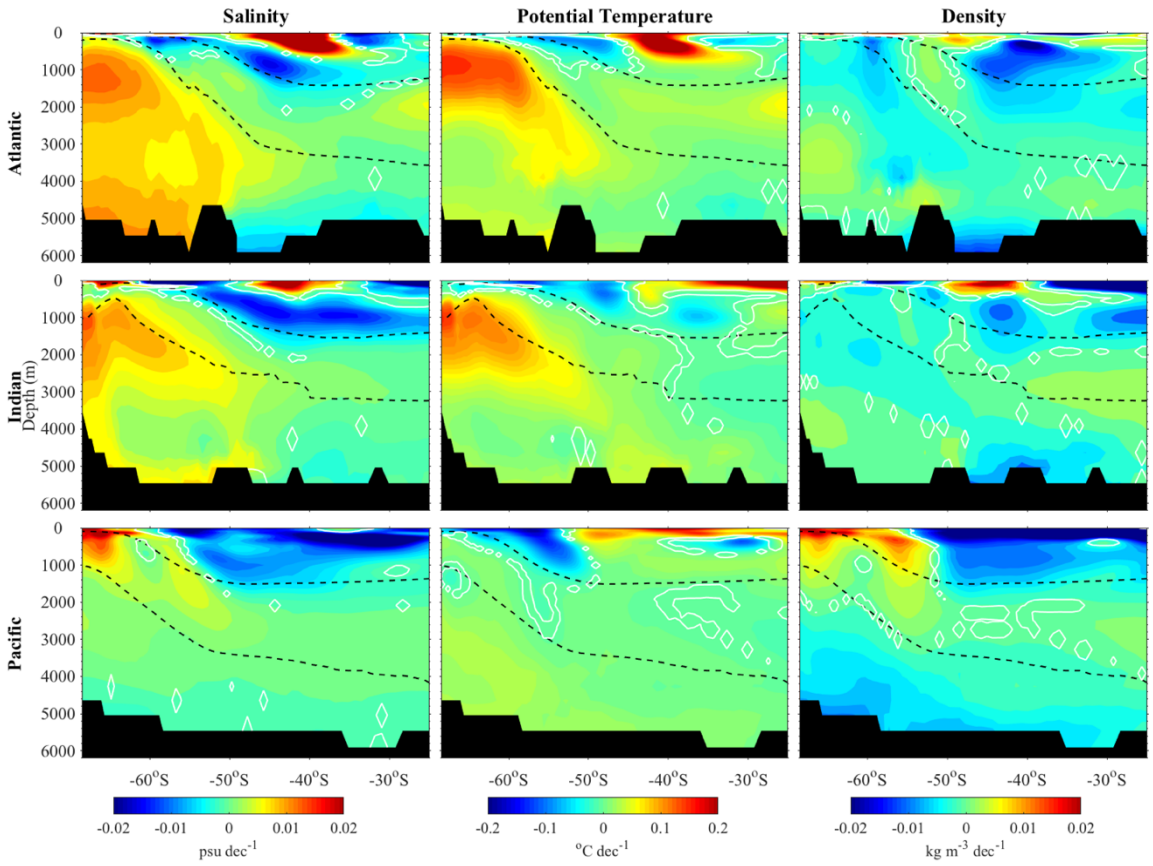

Figure 3.11. Coefficients of regression for salinity, temperature, and density for each of the Atlantic, Indian, and Pacific basins. A least-squares linear regression is used to fit the mean monthly anomaly for the variables between 1992 – 2015. The regions within the white contour are not statistically significant ($p > 0.05$) and those contours outside are significant ($p < 0.05$). The dashed lines represent the time-mean 27.72 kg m^{-3} and 28.11 kg m^{-3} neutral density surfaces between 1992 – 2015 for each respective basin.

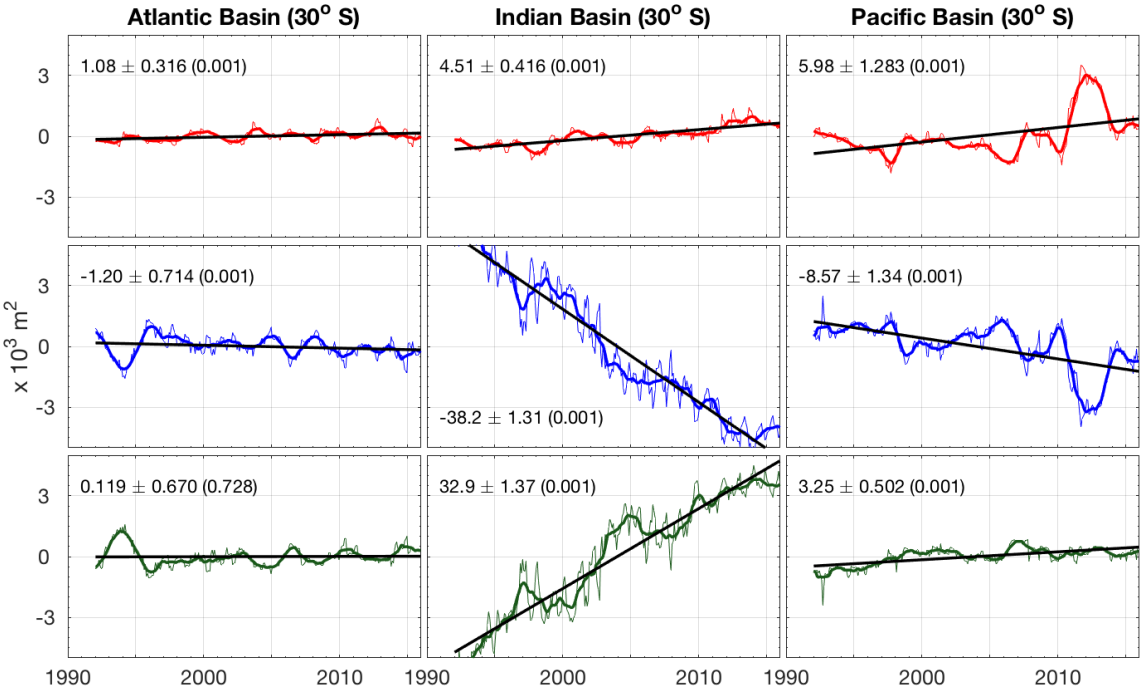

Figure 3.12. Monthly climatological anomalies of the area of neutral density-integrated meridional transports, the 12-month running mean (bold), and regression line (black). Red represents the upper branch, blue the middle branch, and green the bottom branch. The meridional transport is estimated across 30° S and binned based on 27.72 kg m^{-3} and 28.11 kg m^{-3} neutral density surfaces.

CHAPTER 4

DIAGNOSING BIASES IN ESTIMATES OF THE ANTARCTIC POLAR FRONT LOCATION AND VARIABILITY[3]

[3]Ferster, B. S., B. Subrahmanyam, and A.M. MacDonald (2019). Diagnosing Biases in Estimates of the Antarctic Polar Front Location and Variability, Submitted to the Journal of Geophysical Research: Oceans.

Abstract

Two methods for estimating Polar Front (PF) location, one based on sea surface temperature (SST), the other on sea surface height (SSH), are compared. Using the latest product from the Estimating the Circulation and Climate of the Ocean (ECCO) group, the PF locations are found to be similar to both climatology and a 24-year mean position. The SST approach produces larger estimates of seasonal and monthly variability. Both methods indicate geographically localized patterns in the location of the PF; a shift northward in the central Pacific and southward in the Atlantic and Indian Basins. SST-based zonal averages indicate a significant northward trend in the Pacific Basin (1.15 ± 0.73 km year-1), which is not observed in the SSH-based averages. On the other hand, the SSH approach suggests a southward drift in average position in all basins over time, a result not seen using SSTs. The seasonal and interannual variability of the PF is moderately-to-strongly correlated to decreasing temperatures and salinity within the ACC region. Combined with the northward trends of the PF in the central Pacific, the northward shift could be driving the observed decrease in central South Pacific temperatures. The interannual variability of the PF is weak-to-moderately correlated with the Antarctic and Southern Oscillations, but a large portion of the PF variability remains unexplained.

4.1. Introduction

Large-scale circulation within the Southern Ocean (SO) is dominated by the strong, eastward flow of the Antarctic Circumpolar Current (ACC). While this region is largely wind-driven (Marshall and Speer, 2012), the path of the ACC is strongly influenced by the bottom topography (Sokolov and Rintoul, 2009a; Freeman et al., 2016). The SO is unique

in that it is the only ocean that can freely flow to encircle the globe, separating the subtropical and subpolar regimes of the Southern Hemisphere (SH). The ACC region is comprised of strong eddies and jets, and is identified through three primary fronts: the Subantarctic Front (SAF), the Polar Front (PF), and the Southern ACC Front (SACCF). Each of the three fronts is classified by distinct water properties and has been shown to have strong meridional gradients in temperature, salinity, and biological productivity. The ACC therefore acts as a thermohaline boundary between the mid- and high latitude systems. The importance of this region to global circulation and climate is through its redistribution of heat, gases, and nutrients among the Atlantic, Indian, and Pacific Ocean Basins (Marshall and Speer, 2012).

Through the introduction of satellite-derived sea surface height (SSH) and sea surface temperature (SST), there has been an improved understanding of ACC variability (eg. Sokolov and Rintoul, 2009a,b; Freeman et al., 2016). Novel approaches in monitoring the ACC fronts have been developed using sea surface satellite data. Some use SSH (Sokolov and Rintoul, 2006a; Sokolov and Rintoul, 2009a,b; Kim and Orsi, 2014) and others SST (Dong et al., 2006; Freeman and Lovenduski, 2016a). Both methods have been shown to produce PF location estimates similar to in situ and observational approaches defined by water mass properties (Orsi et al., 1995; Belkin and Gordon, 1996). Compared to techniques using ground-based observations, which are limited spatially, temporally, or both, satellite-derived methods offer continuous monitoring of the strong seasonality of the entire SO with high spatial resolution.

Changes in the SH wind regimes have previously been regarded as the dominant factor in the variability of the ACC (Böning et al., 2008; Gille, 2008). It is generally thought

that the SH westerlies have intensified and shifted poleward (Marshall, 2003), largely due to the depletion of the stratospheric ozone layer (Marshall et al., 2001; Marshall and Solomon, 2002). The dominant mode of atmospheric variability in the SH is known as the Antarctic Oscillation (AAO, also referred to as the Southern Annular Mode). The trend of the mode is thought to be increasingly positive as a result of decreasing pressure over the poles and increasing pressure over mid-latitudes (Miller, 2006). These trends have been used to explain the shift and intensification of the westerlies. The other large-scale mode of ocean-atmospheric variability associated with the position of the ACC is the Southern Oscillation. The Southern Oscillation Index (SOI) is a common metric used to describe the El Niño-Southern Oscillation (ENSO) relationship. ENSO variability has been shown to have strong influences on SST, sea-ice, and atmospheric temperatures in the SH (Fogt and Bromwich, 2006; Welhouse et al., 2016; Cerrone et al., 2017, Ferster et al., 2018). Results from both SST and SSH studies suggest that large-scale AAO and ENSO variability is weakly correlated with ACC position (Sallée et al., 2008, Kim and Orsi, 2014; Freeman et al., 2016), mainly within the Pacific and parts of the Indian Basin.

The objective of this investigation is to analyze and compare the recent variability in the location of the PF using the two different satellite-based approaches (SST vs. SSH). In analysis with satellite-derived SST, Freeman et al. (2016) indicate that there are no significant trends (shifts) in the location of the PF and that there is low seasonal and interannual variability in the ACC position. Analyses using SSH have indicated both significant shifts in the PF location (Sallée et al., 2008; Sokolov and Rintoul, 2009a; Kim and Orsi, 2014) and a lack of recent trends in the position (Gille, 2014; Freeman et al., 2016; Chapman, 2017). Although changes in the zonal and meridional wind stress have

been linked to shifts in the PF (Dong et al., 2006), the location of the PF is largely thought to be influenced by bottom topography (Dong et al., 2006; Freeman et al., 2016).

Here, the null hypothesis is that there are no significant trends in PF location throughout the 1992-2015 period. As mentioned above, previous works have indicated various results using the SSH method, while the SST approach has consistently indicated that there are no significant trends in PF location. Using the latest state estimate for the *Estimating the Circulation and Climate of the Ocean* (ECCO) version 4 release 3 (Fukumori et al., 2017), we compare the location of the PF and the associated variability and trends using both SST and SSH methods. A state estimate such as ECCO offers the necessary SST and steric SSH outputs that can be used to estimate front locations, and provides the details needed to investigate the surface dynamics associated with ACC variability. Along with estimating the 1992-2015 PF location, additional statistical analyses are used to define the relationship between the PF and surface layer properties, and to demonstrate the major impacts of PF location on surface layer salinity and temperature.

4.2. Methods

4.2.1 Polar Front from SST

The PF location has been estimated using microwave-derived remotely sensed SST with a high degree of accuracy (Dong et al., 2006; Freeman and Lovenduski, 2016a). Freeman et al. (2016) showed that SST at the PF varies seasonally even though the absolute SST gradient exhibits minimal seasonal and interannual variability. The absolute gradient (∇T) is defined as,

$$|\nabla T| = \sqrt{(\delta T/\delta x)^2 + (\delta T/\delta y)^2} \quad (4.1)$$

where δT is the temperature difference (°C) and δx and δy are the distances (km) between longitude and latitude grid spacing, respectively. In both Dong et al. (2006) and Freeman and Lovenduski (2016a), the PF location is defined at the southernmost location where the absolute gradient exceeds 1.5°C per 100 km. Here, this threshold is relaxed across the SO to 1.0°C per 100 km where the gradient is known to be comparatively weaker (Dong et al., 2006; Freeman and Lovenduski, 2016a) and further relaxed in the eastern South Pacific to 0.7°C per 100 km due to the smoothness of the state-estimate product. This approach lowers the gradient threshold compared to the observation-based methods of Dong et al. (2006) and Freeman and Lovenduski (2016a) but is necessary due to a combination of the smoothing of the ECCO product, the average 5 m depth of ECCO SSTs, and the differences in the ECCO versus SST gridded product resolutions. SSTs greater than 10°C were removed from the PF identification method for similar reasons, and because this water property is typically associated with SAF waters. Additionally, SSTs and SST gradients greater than two standard deviations beyond their associated means, and longitude patches smaller than 3° were removed under the assumption that they represented either eddies or small broken-off filaments of frontal branches. The SST method has the advantage of being determined without the influence of steric sea level change and offers a longer record for analysis. Freeman and Lovenduski (2016a) estimated PF location weekly from 2002 through 2014, whereas here the monthly 1992-2015 ECCO product is used. Unlike satellite products, ECCO does not offer the possibility of near-real time analysis, but it does include additional physical properties that can be used to investigate sub-surface relationships to PF location and changes.

4.2.2 Polar Front from SSH

Methods of using SSH contours to identify the ACC fronts go back to the collection of sea level data from the Topex/Poseidon mission. Notable works (i.e. Sokolov and Rintoul, 2006a; Sokolov and Rintoul, 2009a; Kim and Orsi, 2014) have shown dynamic (i.e non-steric) SSH can be used as a good estimator of PF location. Here, the dynamic SSH contour used is –61 cm (Kim and Orsi, 2014). ECCO's SSH variable accounts for steric changes within each grid cell to compensate for the known warming and freshening within the SO (Swart et al., 2018).

4.2.3 Anomalies and Statistical Methods

The 1992-2015 ECCO monthly mean climatology is removed from the monthly record to estimate anomalies for PF location, temperature, and salinity. Removing the monthly climatology normalizes the values and effectively removes seasonality. To calculate trends in PF location, a least squares regression is used with the resulting 288 monthly anomalies. Pearson's correlation coefficient is used to determine the relationship between PF location, and individually, temperature and salinity at the 95% confidence level. The correlation coefficients are described as weak (< 0.30), moderate (0.30–0.70), and strong (> 0.70).

4.3. Data

4.3.1 The ECCO Product

The latest ECCO V4r3 product (Fukumori et al., 2017) provides appropriate resources to analyze the ocean circulation and the temporal variability. ECCO assimilates

in situ and satellite-derived measurements into an ocean-sea ice model based on the MIT general circulation model (MITgcm) (Forget et al., 2015; Fukumori et al., 2017). ECCO has a nominal 1° horizontal grid spacing with an average spatial resolution south of 30°S is 62 km (Forget et al, 2015). It has a maximum depth of 6134 m defined by 50 vertical layers. The layer thickness ranges from 10 m near the surface to 456 m near the bottom and the model includes parameters to account for the varying volume of each three-dimensional grid cell. It uses atmospheric forcing from the ERA-Interim reanalysis (Dee et al., 2011), a proficient sea-ice model (Losch et al., 2010), and three-dimensional, time-invariant mixing coefficients (detailed in Forget et al., 2015) to estimate the bolus component of the residual circulation. The ECCO product used here represents the first global multi-decadal ocean state estimate that includes parameters for both the Antarctic and the Arctic. Further details on this version of ECCO and the model in general can be found in reports by the ECCO Consortium (2017a, b), Forget et al. (2015), and Fukumori et al., (2017).

The advantage of ECCO over non-assimilating GCM's is that it provides ocean circulation parameters consistent within specific uncertainties with available observations, even for the SH high latitudes. SO observations alone are spatially and temporally limited due to the harsh austral winter conditions. This lack of spatial consistency in SO observations is mitigated by ECCO's dynamical system as it conveys the information provided by the observations spatially and temporally across the modeled domain.

4.3.2 Satellite-derived Products

Here, we use the 2002-2014 SST-based PF climatology from Freeman and Lovenduski (2016 a,b) as a comparison metric for the ECCO PF analysis. Henceforth we

refer to it as “the FL16 SST-based climatology” or simply “FL16”. For SSTs, data from A Group for High Resolution Sea Surface Temperature (GHRSST) for 1992 to 2015 are also used to compare with ECCO. This GHRSST product is a combination of microwave and infrared satellite measurements with assimilated in situ observations. The gridded GHRSST version 2.0 (Canada Meteorological Center, 2012) has 0.2° grid spacing. Further information regarding GHRSST can be found in Brasnett (2008). Satellite-derived SSH data (1993-2015) are obtained through the Copernicus Marine Environment Monitoring Service on a 0.25° grid. This reprocessed product allows for quality control checks and cross-calibration between the multiple satellite altimetry missions.

4.3.3 Indices of Large-scale Variability

Here, the location of the PF is compared against proxies for the large-scale climate patterns of the AAO and the Southern Oscillation. The AAO index (from the National Centers of Environmental Prediction, Climate Prediction Center (NCEP, CPC)) is computed from the first principle component from the EOF of the 700 hPa height anomalies between mid- and high latitudes from NCEP/NCAR (National Center for Atmospheric Research) reanalysis data (Kalnay et al., 1996). The SOI is estimated from the observed sea level pressure anomalies between Tahiti, French Polynesia and Darwin, Australia. The SOI, also from NCEP, is standardized by dividing the differences in sea level pressure by the monthly standard deviations (Trenberth and Caron, 2000).

4.4. Results

4.4.1 Comparison of PF Methods

Both the SST and SSH method have previously been used with a high degree of confidence to estimate the location of the PF. Despite strong confidence in SSH contours in previous analyses, Gille (2004) suggests that meridional shifts associated with SSH contours could be biased towards large-scale SSH changes rather than shifts in frontal positions. This idea is consistent with linear trends in SSH (Figure 4.1). In the SO, there is a general increase in sea level over time, even though the ECCO SSH product accounts for steric changes in temperature and salinity. The mean trend in SSH is 2.75 ± 0.10 mm year^{-1}. The largest magnitude trends, both positive and negative, occur in the South Pacific (7.51 ± 0.49 and –5.44 ± 1.4 mm year^{-1}). Although decreasing trends are indicated in the central South Pacific (55°-65°S), over most of the SO SSH is increasing. As Gille (2004) suggests this broad SSH increase means that the meridional shift of the contours used to identify the ACC fronts would result in biased PF location trends.

Trends in SST gradients for the SO depict localized patterns of zonal bands rather than a ubiquitous trend. The largest trends in the SST gradients occur in the central South Pacific, similar to SSH. Indicative of shifts in the different water mass properties, significant trends in the gradients are specified in both the mid-latitudes and ACC regions. The zonal band-like pattern in SST trends suggests that use of SST is the ideal approach for investigating not only the position of the ACC, but also shifts in the mid-latitude gyres and advocates for increased confidence in use of SST gradients over SSH contours. That

being said, here both methods are used to estimate the trends in the PF location so as to compare the different techniques and to compare results from ECCO to previous findings.

Both ECCO and altimetry SSH contour analyses produce PF positions generally similar to each other as well as to the FL16 climatology (Figure 4.2, white, yellow and red contours, respectively); however, in portions of the Pacific and Indian Basins, the SSH results suggest large biases (Figure 4.2a-c). The ECCO SSH-contour PF is further north throughout the entire Pacific and much of the Atlantic, while the altimetry product reveals localized regions between 50°-80°E and 120°-150°E that are further south. There is a strong agreement between the ECCO (black contour) and GHRSST (magenta contour) SST derived PF positions (Figure 4.2a, b, and d), and those from to the FL16 climatology (red contour); however, comparing the SST and SSH derived ECCO PF locations at each grid cell (Figure 4.3a) reveals the large (upward of 5° of latitude) disagreements between the two methods. In most cases, the ECCO SSH contour (black) is further north than the SST gradient approach estimate (red). This difference could be the result of method biases. The SST method relaxes the gradient threshold in regions of low values, whereas the SSH contours are based on a uniform standard; however, it is also true that the ECCO SSH derived PF locations lie to the north of the altimetric estimates (Figure 4.2, compare white and yellow contours). Taken together, these two results suggest that the more northern PF location estimated from ECCO SSH could be the result of a bias in the state estimate, perhaps induced by the grid spacing.

4.4.2 Polar Front Location: SST Method

The PF is located between 45°S and 55°S throughout much of the Atlantic and Indian Basins, while in the Pacific Basin it is situated poleward (55°-60°S). The mean position of the PF (Figure 4.3a) exhibits low variability, depicted through the standard deviations. The largest seasonal variability in the PF occurs throughout the Austral summer months (Figure 4.3c), but overall it maintains low variability as discussed in Freeman et al. (2016). The trends in the PF location (Figure 4.3d) are shown with their 95% confidence interval where they are significantly different from zero. This approach is similar to Orsi et al. (2014) and Freeman et al. (2016), but differs from other past studies as it compares the trends at each grid cell rather than the zonal averaged PF. The trends indicate the largest change is within the Pacific Basin. Orsi et al. (2014) suggest that the large variability in the location of the PF in the southeast Pacific (150°-90°W) is mainly attributed to the Southern Oscillation and ENSO, but they find no long-term trends.

In this analysis, positive trends are found the central South Pacific (160°-130°W), while there are regions of both negative and positive trends within the Atlantic and Indian Basins. These results follow previous literature (i.e. Gille, 2008; Sokolov and Rintoul, 2009b; Orsi et al., 2014), suggesting that trends in the Atlantic and Indian Basins are localized features, likely related to the southward shift of the subtropical gyres (Orsi et al., 2014). The largest individual trend is 6.69 ± 1.2 km year^{-1} in the central South Pacific. The strongest negative trend is located in the Indian Basin near the Agulhas retroflection and demonstrates a poleward trend of -4.13 ± 1.7 km year^{-1}. Regions of relatively large seasonal (Figure 4.3c) and monthly (Figure 4.3b) standard deviations in the PF tend to be

located where trends are not significant. In these instances, the natural variability of the PF inhibits statistical support of linear trends.

In lieu of solely describing trends from individual grid cells, the PF locations are zonally averaged for each of the Pacific, Atlantic, and Indian Basins (Figure 4.4). The 288-month mean (95% confidence interval) PF location in the Pacific is 60.3 ± 0.077°S and is further south than in the Atlantic (53.2 ± 0.085°S) and Indian (50.6 ± 0.026°S) Basins. Unlike Dong et al. (2006) and Freeman et al. (2016a), linear regression results indicate a significant positive trend ($p < 0.001$) in the Pacific basin between 1992-2015. The Atlantic ($p = 0.685$) and Indian ($p = 0.046$) Basins demonstrate trends that are not significantly different from zero. The 95% confidence interval for the Pacific trend is 1.15 ± 0.732 km year^{-1}, signifying a northward shift in the average Pacific PF location. The grid-located and basin averaged trends support similar results. In both instances, there are significant positive trends in the Pacific basins, most notably in the central Pacific. In both the Atlantic and Indian Basins, the relatively high natural variability and opposing localized trends indicate that there are not significant basin scale trends. Although there are not distinct linear trends, variability in the location of the PF can still drive changes in the surface temperature and salinity of the SO.

4.4.3 Polar Front Relationship with Temperature and Salinity: SST Method

To compare the reciprocal influences of PF location and surface SO properties, the PF is zonally averaged within each basin. The monthly-mean basin PF location is then compared with temperature and salinity anomalies associated with each individual grid-cell. Correlations with temperature over the 288 months indicate a strong negative

relationship between PF location and surface temperature (Figure 4.5a-c). A negative relationship would suggest that in months with a northward shift in the mean PF location, surface water temperatures decrease. This negative relationship is true between 45°-65°S in the Pacific, and between 45°-55°S in both the Atlantic and Indian. Significant negative correlations range from –0.15 to –0.71, and the strongest negative correlations are in the central South Pacific. In each of the three basins, the central mid-latitudes a positive relationship is indicated. Whether from the strength or location of the mid-latitude gyres or from the position of the PF, the correlations suggest that if the PF shifts northward, surface temperatures increase. The strongest positive trends are found along the Antarctic coast in both the Atlantic and Indian sectors, suggesting significant implications for sea ice and deep-water formation. The strength of these significant correlations is weaker in the mid-latitudes and strongest near the coast, ranging from 0.15 to 0.98.

The pattern of correlations between the PF and surface salinity (Figure 4.5d-f) is less clear and differs spatially from that of temperature. The maximum negative correlation is –0.41 and occurs in the Pacific Basin, while the strongest positive correlation is 0.46 within the Atlantic. Positive correlations indicate locations where salinity increases are related to a northward shift in the PF. The results signify a positive relationship within the western Pacific, the Polar regions of the SO, the western mid-latitude Atlantic, and the eastern mid-latitude Atlantic and Indian Basins. There are negative relationships in the western Pacific between 30°-55°S, the Atlantic from 40°-50°S, and across the eastern Indian Basin.

Correlations with subsurface waters due to the strong upwelling within the ACC region are further explored (Figure 4.6). The highest correlations are in the surface 100 m

in all three basins, with strong negative correlations near the location of the PF and moderate positive relationships in the approximate location of the subtropical gyres. These correlations indicative of a northward shift in the PF are related to decreasing temperatures in the ACC region and increasing temperatures in the southern hemisphere subtropics. In both the Pacific and Atlantic, the negative relationship with temperatures in the ACC region extends to depths of 1000 m. Correlations with the zonally averaged temperature anomalies indicate the strongest relationships are within the Pacific. There are weak-to-moderate positive and negative correlations in the Pacific extending down into the water column beyond 1000 m, suggesting a significant relationship to the surface water dynamics, a relationship which is certainly seen in eddies (eg. Moore et al., 2000; Thompson, 2010; Mitsudera et al., 2018). In both the Atlantic and Indian Basins, most of the significant correlations are confined to the upper 300 m, but there are localized positive correlations along the 2°C isotherm to depths over 1000 m.

The subsurface salinity structure indicates the strongest correlations are between 100 to 400 m. Despite stronger correlations being at depth rather than at the surface, these relationships are weak-to-moderate at best. Similar to temperature, the Pacific salinity presents the largest areas of significant correlations. As the PF moves northward in the Pacific, there is a negative correlation to the north of the PF location and a positive correlation to the south. This result suggests that a northward shift in the Pacific drives the deeper, higher salinity waters northward. A similar pattern exists in the other basins where fewer correlations that are significant at the 95% confidence level.

4.4.4 Polar Front Location: SSH Method

As mentioned in section 4.1, compared to SST-derived estimates, mean SSH-derived PF locations indicate a more southerly position in the Pacific and more northerly positions in the Atlantic and Indian Basins. The variability in the mean location associated with the SSH approach (Figure 4.3a, black) is less than that associated with the SST method (Figure 4.3a, red). Moreover, the SSH-derived seasonal and monthly (Figure 4.3b and 4.3c) standard deviations are smaller than those associated with the ECCO and FL16 SST derivations, suggesting that the SSH method produces less interannual movement in PF location. The trends in the SSH-derived PF location (Figure 4.3d) have negative slopes, i.e. southward (poleward) shifting PF locations throughout much of the Indian and Atlantic. The largest negative trends (-13.8 ± 1.6 km year^{-1}) are within the Agulhas retroflection region of the southern Indian Ocean. Positive trends of 3.05 ± 0.71 km year^{-1} are indicated in the central South Pacific, but negative trends dominate the remainder of the Pacific. The directions of the SSH- and SST-derived PF trends are similar; however, the SSH-derived southward shift in the Indian and Atlantic is greater and the northward shift in the central South Pacific is weaker. The results are similar to Orsi et al. (2014) in that strong negative trends are found in the Atlantic and Indian and positive trends are found in the Pacific. However, Orsi et al. (2014) suggests that the positive trends in the central Pacific are not significant, whereas our results indicate that they are.

There are negative (southward) shifts in the zonally averaged PF trends in all basins between 1992 and 2015 (Figure 4.7). The 288-month mean PF location in the Pacific is 57.3 ± 0.018°S, in the Atlantic is 50.2 ± 0.017°S, and in the Indian is 49.6 ± 0.025°S. Linear regressions indicate the trends in the PF location for the Pacific, Atlantic and Indian Basin

of –0.950 ± 0.35 km year^{-1} ($p < 0.001$), –1.80 ± 0.17 km year^{-1} ($p < 0.001$), and –2.03 ± 0.32 km year^{-1} ($p < 0.001$), respectively. Although weakest in the Pacific, all three basins indicate a poleward trend in PF location. This general trend, which is partially attributed to the change in SSH, is also related to changes in the contour used throughout the 24-year period. The decreasing SSH indicated in the central South Pacific could support the localized northward shift in the PF location, however, most of the SO has a negative trend in the SSH, indicating the –61 cm contour is shifting poleward. As a result, trends indicated using the SSH contour approach are likely biased on longer timescales.

4.4.5 Polar Front Relationship with Temperature and Salinity: SSH Method

SSH-derived correlations between PF location anomalies and surface temperature anomalies (Figure 4.8a-c) over the 288-monthly duration (1992-2015) are weaker and differ spatially from the SST gradient estimates. In the central South Pacific between 40°-65°S and in the central Atlantic between 35°-55°S there are negative correlations. A negative relationship indicates in months with a northward shift in the mean PF location surface water temperatures decrease. In the South Indian Basin (50°-65°S) there are positive correlations with surface temperatures, suggesting increased temperatures associated with northward PF shifts. The SST and SSH results for the South Indian Basin differ as the latter displays less significant correlations within the ACC region and increased negative and spatially different correlations in the mid-latitudes. In the central mid-latitudes of the Atlantic and Pacific there are smaller, but still significant positive relationships between the PF location and surface temperatures. Significant negative correlations throughout the three basins range from –0.15 to –0.54, and the strongest

negative correlations are in the central Atlantic. The positive correlations in the Indian Basin range from 0.15 to 0.50.

Correlations between the PF and surface salinity (Figure 4.8d-f) are greater in the mid-latitudes, rather than in the ACC. The surface salinity in the Pacific mid-latitude is largely positively correlated to PF location, most notably along the South American coast in the eastern Pacific. In the ACC region of the western South Pacific, there is a positive correlation between 50°-60°S and negative correlation between 60°-70°S. In the Atlantic and Indian negative relationships dominate between 35°-45°S, while positive correlations dominate the central mid-latitude Atlantic (30°-40°S) and the eastern to central mid- to low-latitude Indian. The maximum negative (positive) correlation is –0.61 (0.65). Both extremes occur in the mid-latitude Atlantic Basin. The results signify a stronger relationship within the mid-latitudes of all three basins, rather than the ACC region.

The spatial SSH-derived correlations with subsurface temperature and salinity (Figure 4.9) are stronger than the SST gradient-derived estimates. Correlations for both temperature and salinity are strongest in the Atlantic and Indian and approach 1. Moreover, the strongest relationships are shown to be below 200 m depth for both temperature and salinity. In all three basins and for both temperature and salinity, there are negative correlations north of the PF and positive correlations south of the PF. This relationship is indicative of the northward shift of water properties associated with Ekman driven transport. SSH-derived correlations in the Pacific are weaker that SST-derived correlations. These results could differ based on the variability in the location of the PF, as the SSH method demonstrated significant negative trends in the western and eastern portions of the Pacific and positive trends in the central region.

4.4.6 Large-scale Variability

The position of the ACC is often compared to the low frequency, large-scale climate variability patterns of the AAO and Southern Oscillation. In the South Pacific there are weakly positive correlations between the AAO (Figure 4.10a) and the anomalies in the PF location. The maximum correlation from the SST (SSH) method in the South Pacific is 0.29 (0.43). The correlations in the Atlantic and the Indian (80° W-100°E) are generally very weakly negative (< –0.25). The maximum negative correlation is –0.26 (–0.42) and is located within the southeast Indian Basin. The general pattern is a positive correlation with the AAO in the Pacific and a negative relationship in the Atlantic and Indian, especially on longer timescales (Figure 4.10b). Maximum correlation values of –0.64 (–0.71) and 0.48 (0.54) are located within these regions.

The zonal average PF location timeseries are further compared to the AAO for each basin on monthly scales (Table 4.1). The correlation coefficients for the SST and SSH methods are 0.277 ($p < 0.001$) and 0.269 ($p < 0.001$), suggesting a weak positive relationship between the AAO and PF location throughout the Pacific. The Atlantic and Indian basins are also significant using the SSH method, with values of –0.159 ($p = 0.007$) and –0.240 ($p < 0.001$) respectively. Using the SST approach, the results based on the zonal mean position differ statistically from the correlations at each grid cell (Figure 4.10a). That is, in the Atlantic and Indian, zonal mean analysis suggests no significant correlations, but grid cell analysis suggests localized significant correlations. This indicates that the large-scale variability of the AAO strongly relates to regional changes on monthly scales in the Atlantic and Indian Basins.

The correlations between the SOI and the anomalies in the PF location (Figure 4.10) indicate weak-to-moderate positive correlations in the South Pacific and weak negative correlations in the Atlantic and Indian. The maximum correlation for the SST (SSH) method in the South Pacific is 0.38 (0.46). In the Atlantic and the Indian (80°W-100°E), correlations are generally weak negative (< –0.25). The maximum SST (SSH) negative correlation is –0.33 (–0.27) and is located within the Atlantic. There is a general pattern of positive correlation with the SOI in the Pacific and negative in the Atlantic and Indian. Correlations on yearly time-scales in the central Pacific indicate a stronger relationship with the SOI than with those on monthly time-scales. Values in the central Pacific are as large as 0.70 (0.74), indicating the moderate-to-strong relationship. There is also a pattern of negative correlations in the region of Atlantic-Indian exchange, 20ºW to 60ºE. Maximum correlations for this region are –0.56 (–0.74). In all three basins, the zonally averaged PF location is significantly correlated to the SOI. The correlation coefficients for the SST and SSH methods are 0.312 ($p < 0.001$) and 0.259 ($p < 0.001$) in the Pacific, –0.141 ($p = 0.017$) and –0.172 ($p = 0.003$) in the Atlantic, and –0.202 ($p < 0.001$) and –0.184 ($p = 0.002$) in the Indian basin. These correlations indicate the weak basin-wide relationship between the Southern Oscillation and the PF location on monthly scales.

4.5. Conclusions

The SO is known to be warming throughout recent decades (Swart et al., 2018), but this warming is not driving a uniform increase in the SST gradient. Compared to the SSH approach, the trends in SST gradients demonstrate a meridional shift in both the ACC and subtropical gyres. This meridional shift is more indicative of ocean front and property displacement, than the ubiquitous positive trend in steric SSH (2.75 ± 0.10 mm year^{-1})

alone. A positive trend in SSH throughout the SO explains the significant negative (southward) trends in the PF location derived from the –61 cm contour, except in the central Pacific where sea level is decreasing. Therefore, the SST gradient approach of monitoring the ACC fronts can be used with greater confidence as an unbiased approach on longer timescales.

The SSH method suggests a more northerly mean PF location compared to the SST gradient method. Differences between the two methods are as large as 3º of latitude, larger than the variability of the PF. The SST method used here suggests the large variability seasonally and monthly, but is otherwise spatially similar to Freeman et al. (2016). The SSH approach exhibits low seasonal and monthly variability suggesting that this technique supports a strong linear nature to PF location variability. Both methods advocate regional northward shifts in the central Pacific and southward trends in the Atlantic and Indian. While the two methods produce differing magnitudes in Indian Basin negative trends there is strong agreement in the central Pacific.

Here, both methods suggest a significant northward (positive) PF shift in the central Pacific. a result that agrees with the shorter Freeman et al. (2016a) SST-based analysis (although they found no apparent displacement of the mean zonal PF). Orsi et al.'s (2014) 1993-2010 SSH based study found positive trends in the southeast Pacific, but these were not statistically significant over this short period. Similar to both studies, patterns in PF location trends are localized, but more so using the SST gradient approach. The trends in the PF location derived from SSH indicate a southward shift throughout much of the SO, except portions of the central Pacific and south of Australia, both regions shown to have negative trends in sea level (Figure 4.1d). The zonal averaged trends indicated by the SST

gradient method are only a significant in the Pacific where they are positive (1.15 ± 0.73 km year^{-1}), whereas those indicated by the SSH are significant and negative in all three basins: Pacific (–0.950 ± 0.35 km year^{-1}), Atlantic (–1.80 ± 0.17 km year^{-1}), and Indian (–2.03 ± 0.32 km year^{-1}).

Even without considering trends, variability in the location of the PF is significantly correlated to both temperature and salinity anomalies. Correlations indicate that northward shifts in the PF location are related to decreasing temperatures and salinities within the ACC region and increasing temperature and salinities in mid-latitudes and along the Indian and Atlantic coasts. Moreover, the moderate correlations in the mid-latitudes could imply a relationship between the subtropical gyres and ACC, rather than the ACC driving changes alone. Correlations with ocean properties exist down to 1000 m (and potentially deeper), signifying shift in isopycnals and upwelled water masses.

Interannual PF location variability has been further explored examining the influences of large-scale patterns. The analysis finds a stronger relationship with the Southern Oscillation than with the AAO. The Southern Oscillation is weak-to-moderately correlated on both weekly and monthly scales, whereas the AAO is weakly correlated on monthly scales. These results indicate the ENSO phenomenon of La Niña (El Niño) is weakly related to positive (negative) shifts in the Pacific and negative (positive) drifts in the Atlantic and Indian. The positive AAO phase is weakly responsible for similar patterns; a positive shift in the Pacific and negative in the Atlantic and Indian. The opposite is true for the negative phase of the AAO.

In summary, the SST gradient approach is unbiased to changes in sea level and steric contributions. Localized trends produced by both methods indicate a northward shift of the PF in the central Pacific and a southward shift throughout Atlantic and Indian. Trends in the Atlantic and Indian basins using the SST gradients are not significant, but still display seasonal and interannual variability that can influence surface water properties. A northward shift in the PF moderately-to-strongly relates to decreasing temperatures and salinity within and north of the ACC region. Combined with the northward trends of the PF in the central Pacific, the shift in the PF is in part responsible for driving the decreased temperatures in the central South Pacific. Variability in the PF is weakly-to-moderately correlated to both the AAO and Southern Oscillation on monthly scales, and moderately correlated to the Southern Oscillation on year scales. These results indicate variability in PF location is weakly related to the leading principle component of the westerlies (i.e. AAO) and ENSO phenomena; suggesting that a significant portion of what drives changes in PF location is largely left unknown. Our results imply that central South Pacific temperatures are decreasing as a result of the northward shift in the PF, but only a small portion of the PF location variability can be explained through large-scale patterns.

Table 4.1. Regression and correlation values from Figures 4.4 and 4.7. Regression values are estimated from the 288-monthly timeseries and are presented in units of km year^{-1} for both identification methods. Monthly correlation values with the large-scale variability are calculated using zero-lag.

Method		Regression	p-value	Standard Error	R^2	Confidence Interval	AAO	p-value	SOI	p-value
SST Gradients	Pacific	1.148	< 0.001	0.282	0.051	0.732	0.277	< 0.001	0.312	< 0.001
	Atlantic	-0.416	0.685	0.374	0.001	0.970	-0.078	0.187	-0.141	0.017
	Indian	0.176	0.056	0.212	-0.001	0.549	-0.025	0.674	-0.202	< 0.001
SSH	Pacific	-0.950	< 0.001	0.133	0.149	0.345	0.269	< 0.001	0.259	< 0.001
	Atlantic	-1.803	< 0.001	0.066	0.722	0.171	-0.159	0.007	-0.172	0.003
	Indian	-2.034	< 0.001	0.122	0.490	0.317	-0.240	< 0.001	-0.184	0.002

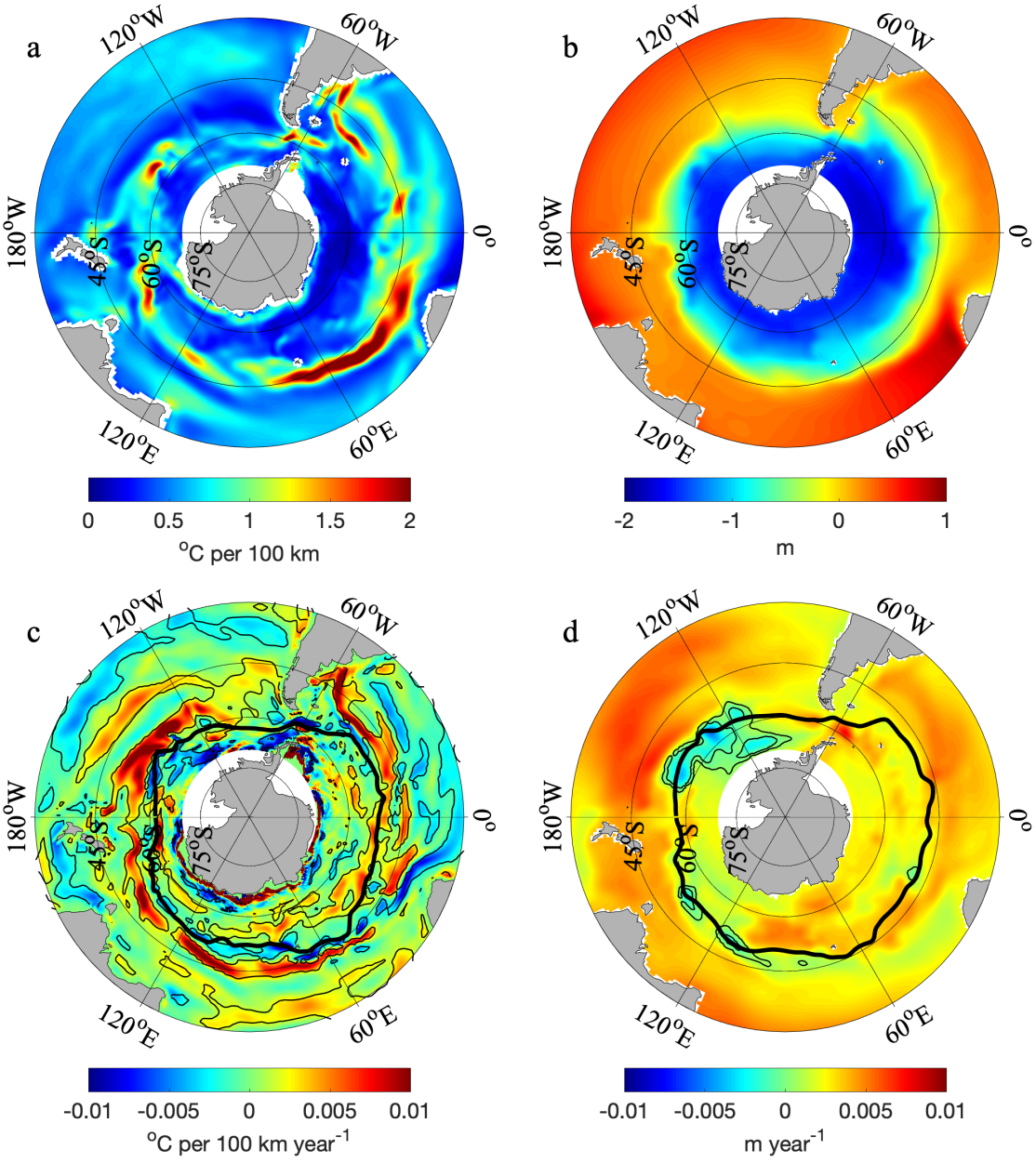

Figure 4.1. The 288-monthly mean SST gradient (a) and steric SSH (b). Linear regressions of SST gradient (c) and steric SSH (d) in units per year. Trends significant at the 95% confidence level are contoured in black.

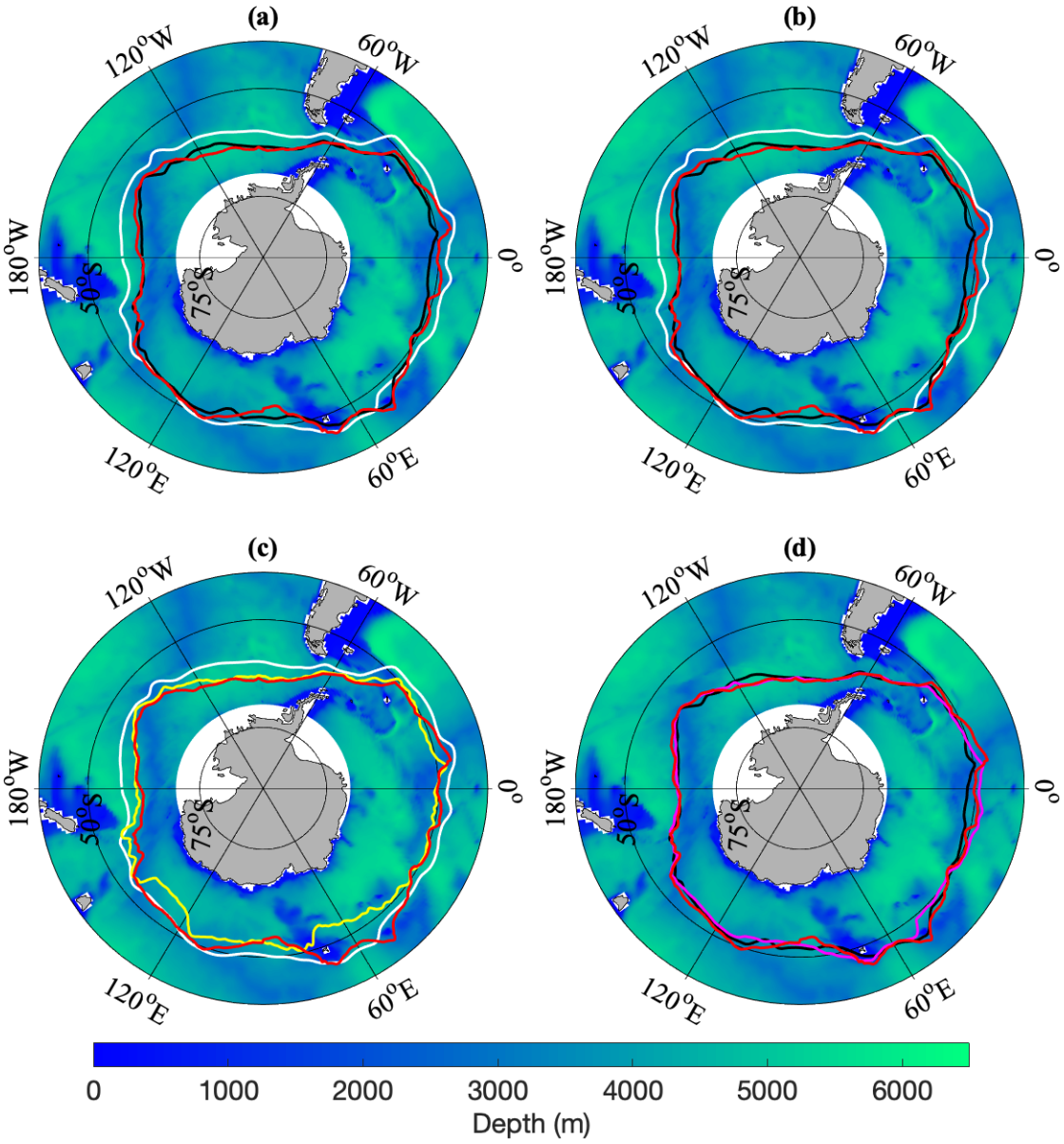

Figure 4.2. Mean ECCO derived PF location 2002-2014 (a) and 1992-2015 (b-d) overlaid on bathymetry from ECCO. Contours are: white derived from ECCO SSH; black derived from ECCO SST gradients. The results are compared to: red 2002-2014 SST-based climatological mean from Freeman and Lovenduski (2016b); yellow derived from 1993-2015 satellite altimetry (c), and magenta derived from 1992-2015 GHRSST (d).

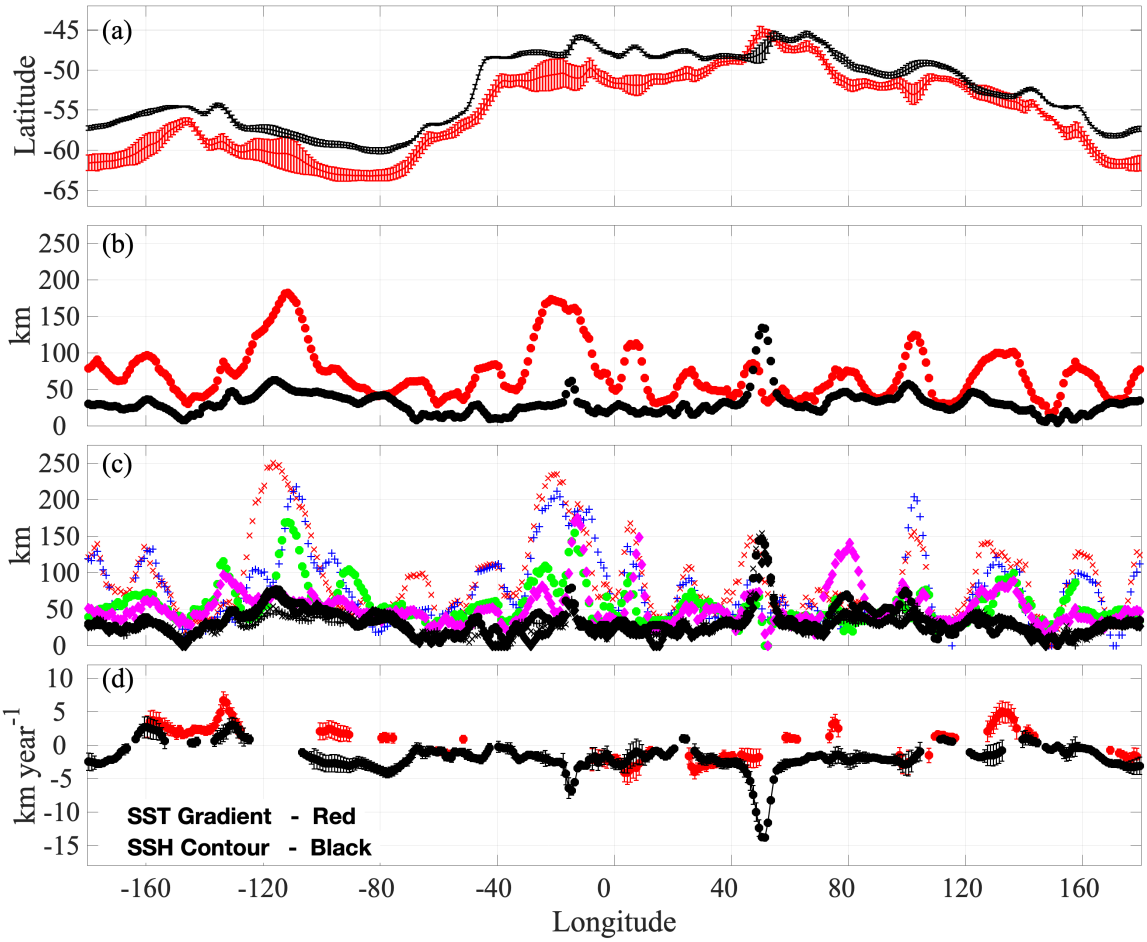

Figure 4.3. The 288-month ECCO-derived SST gradient-based (red) and SSH contour-based (black) mean PF positions with standard deviations (a), temporal standard deviations in units of km (b), seasonal standard deviations in units of km (c), and linear trends with 95% confidence intervals (d). In (d) only values significant at the 95% confidence level are shown. In (c), the "x" symbol are January, "+" are April, circles are July, and diamonds are October standard deviations. To help distinguish the differences in the SST gradient derived PF variability (c), the January standard deviation has been changed to red, April to blue, July to green, and October to magenta.

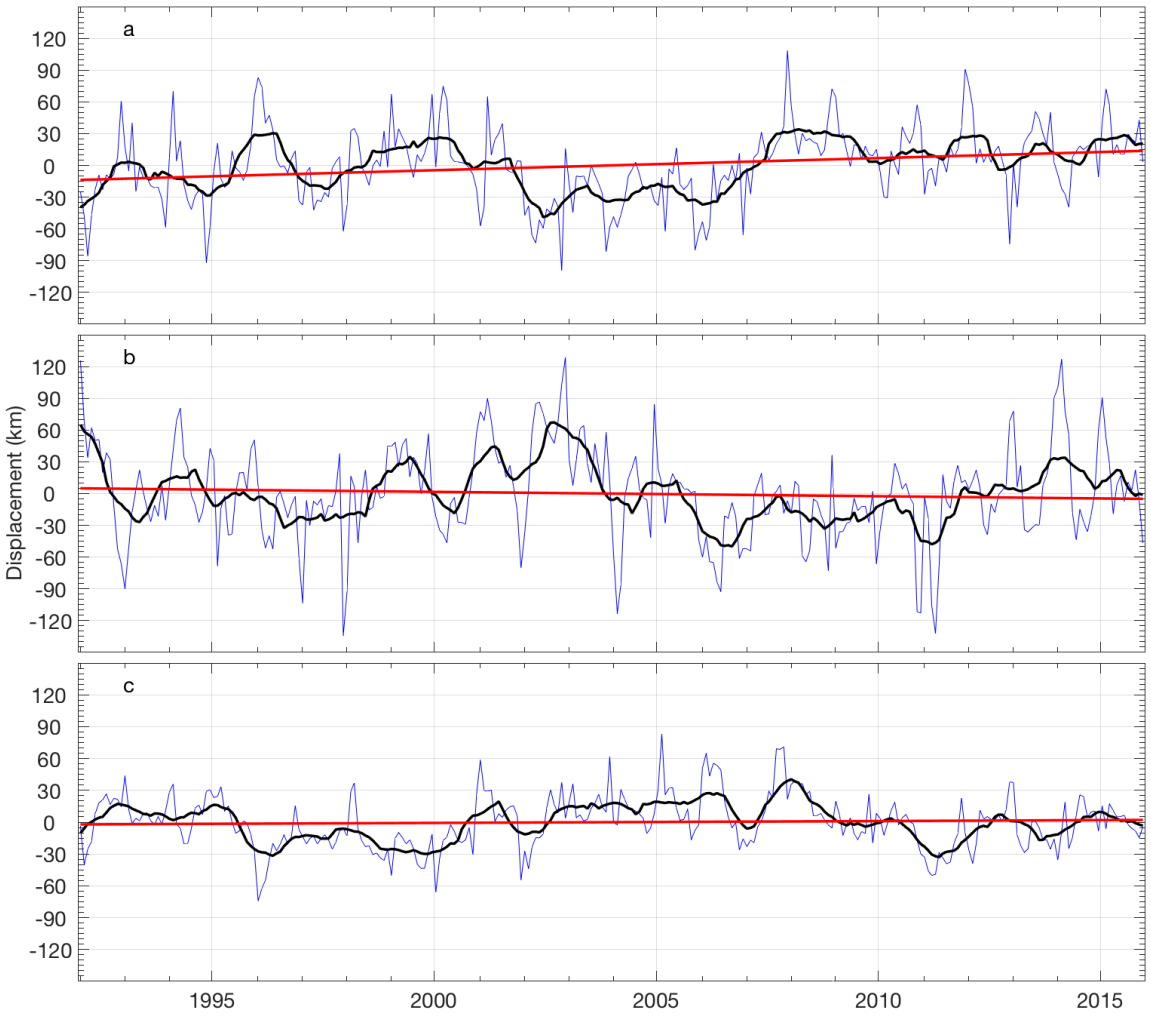

Figure 4.4. Timeseries of the anomalous displacement of the Polar front location in the Pacific (a), Atlantic (b), and Indian (c) Basins using sea surface temperature gradients. The monthly displacement (blue), 12-month running mean (black), and the linear regression (red) are plotted for each basin and the corresponding statistical values are found in Table 4.1.

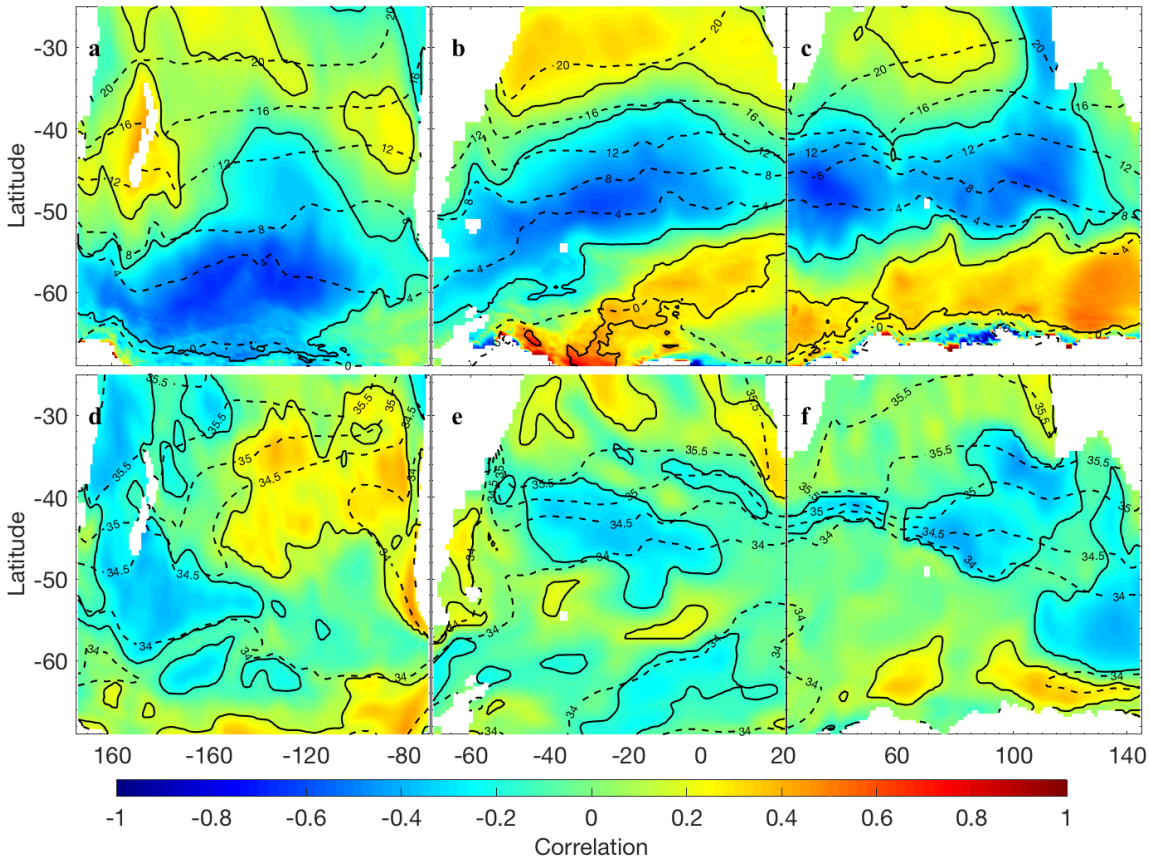

Figure 4.5. Correlation coefficients between the anomalous PF location using sea surface temperature gradients and the mean anomalous 0-100 m temperature (a-c) and (d-f) salinity for the Pacific (a,d), Atlantic (b,e), and Indian (c,f). Correlations significant at the 95% confidence level are contoured in black.

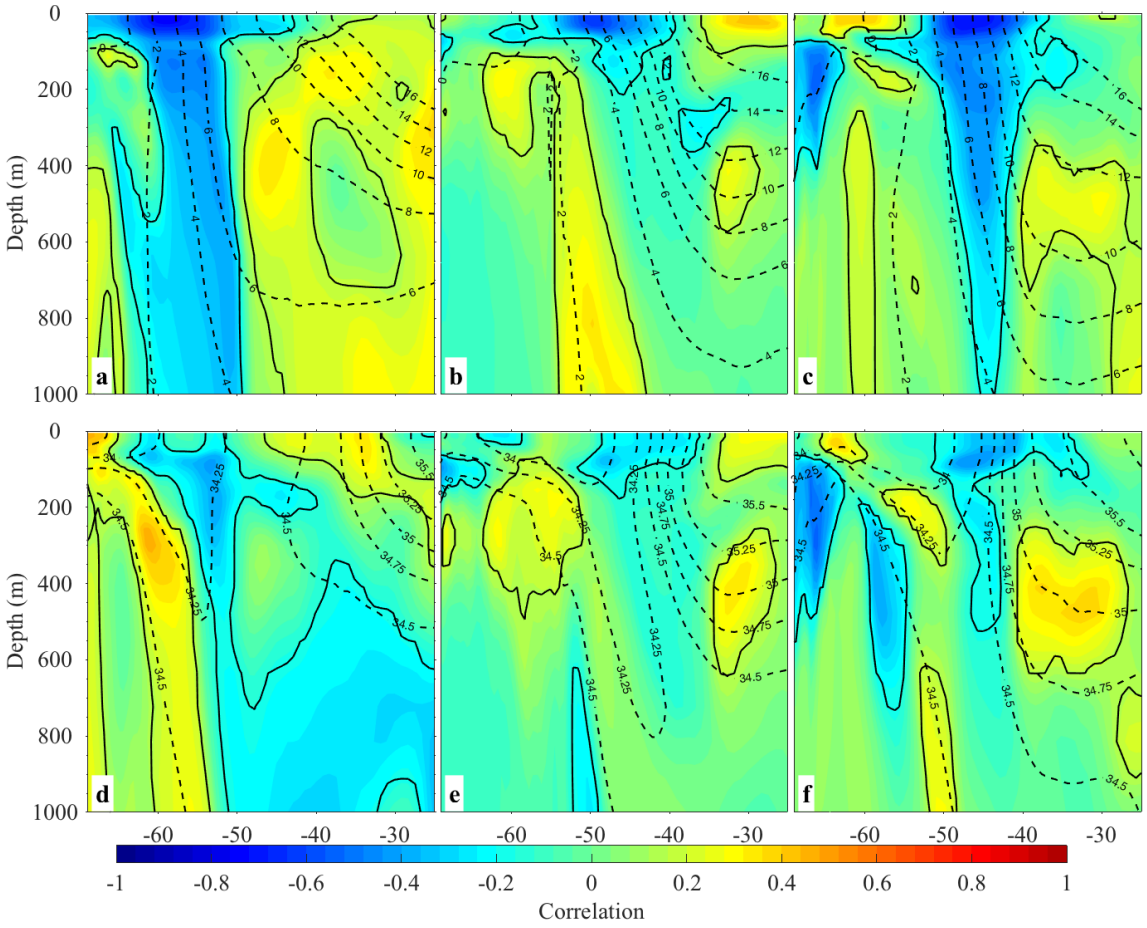

Figure 4.6. Correlation coefficients between the anomalous PF location using sea surface temperature gradients and the zonal mean anomalous temperature (a-c) and (d-f) salinity for the Pacific (a,d), Atlantic (b,e), and Indian (c,f). Correlations significant at the 95% confidence level are contoured in black.

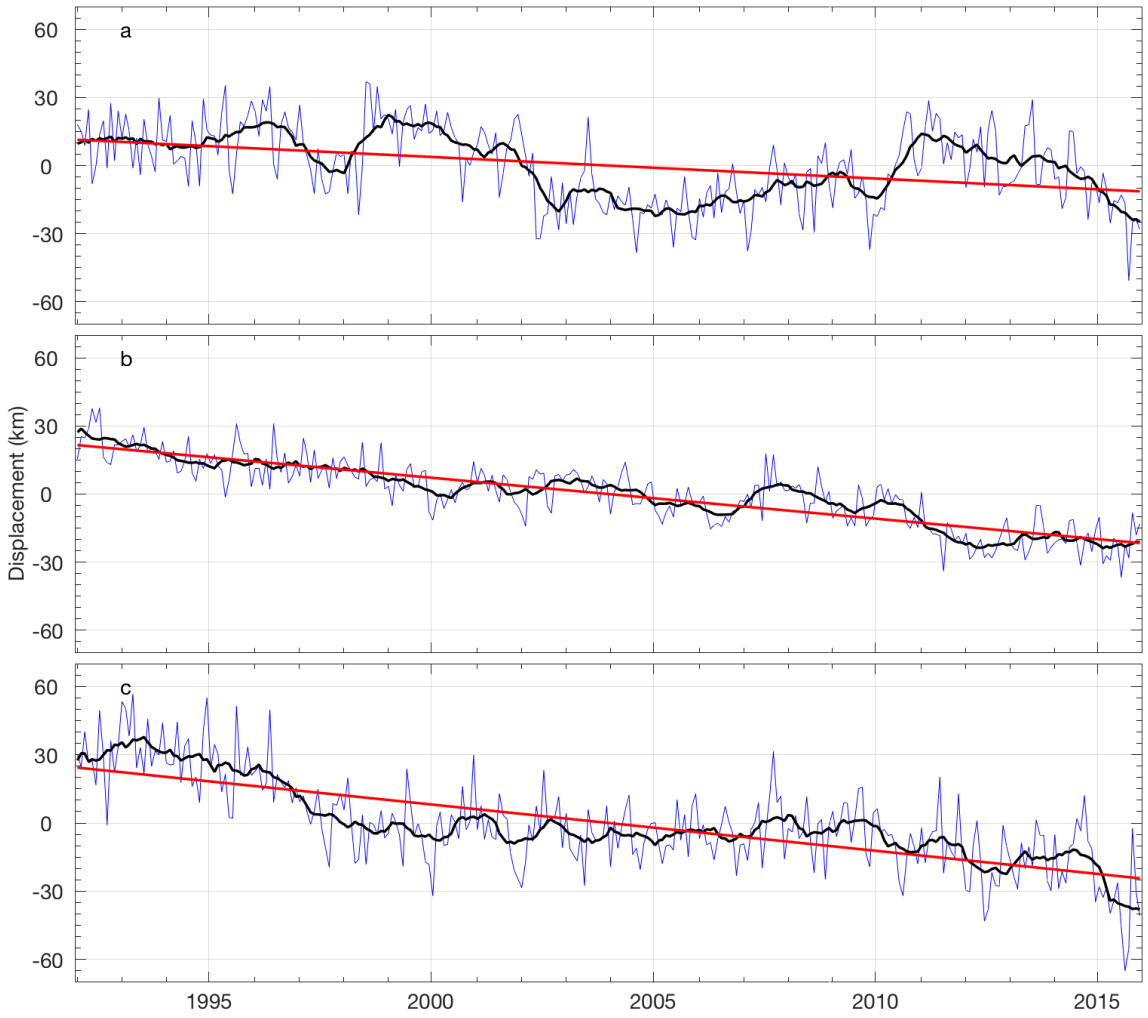

Figure 4.7. Timeseries of the anomalous displacement of the Polar front location in the Pacific (a), Atlantic (b), and Indian (c) using the sea surface height contours. The monthly displacement (blue), 12-month running mean (black), and the linear regression (red) are plotted for each basin and the corresponding statistical values are found in Table 4.1.

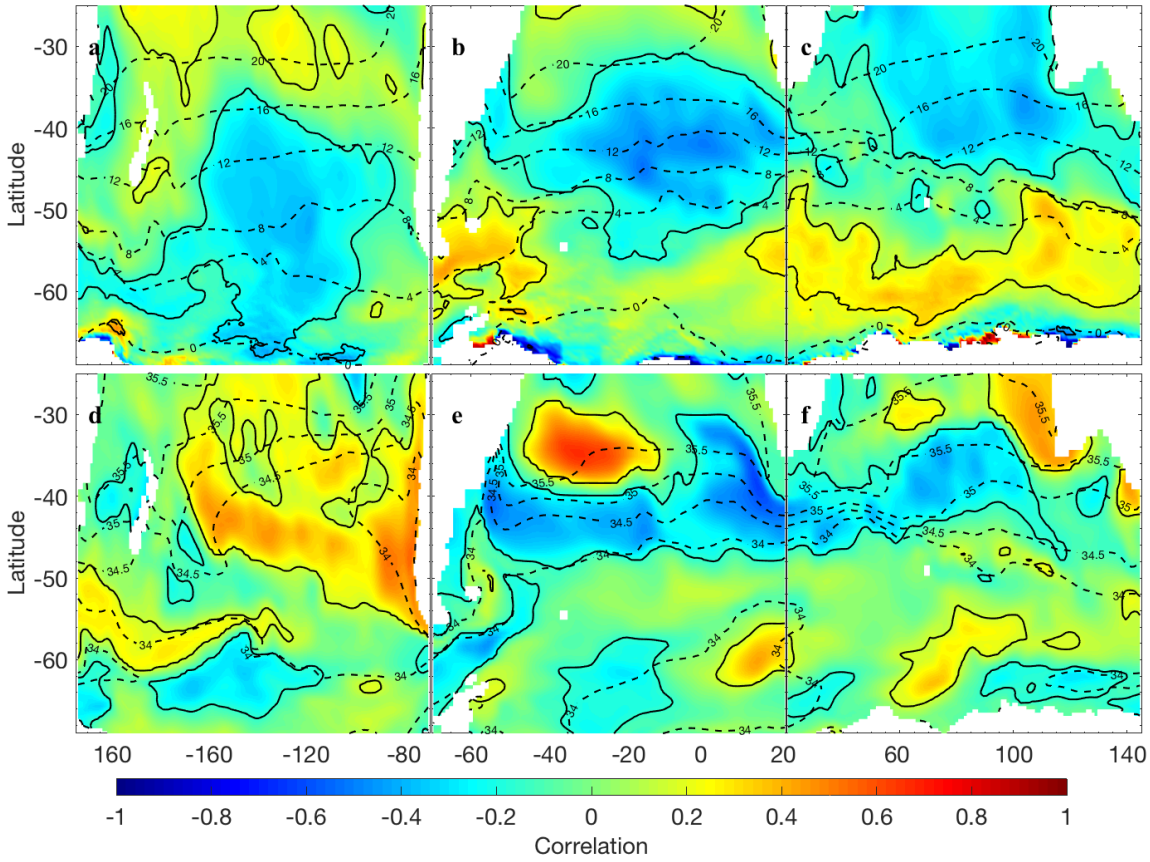

Figure 4.8. Correlation coefficients between the anomalous PF location using the sea surface height contours and the mean anomalous 0-100 m temperature (a-c) and (d-f) salinity for the Pacific (a,d), Atlantic (b,e), and Indian (c,f) basins. Correlations significant at the 95% confidence level are contoured in black.

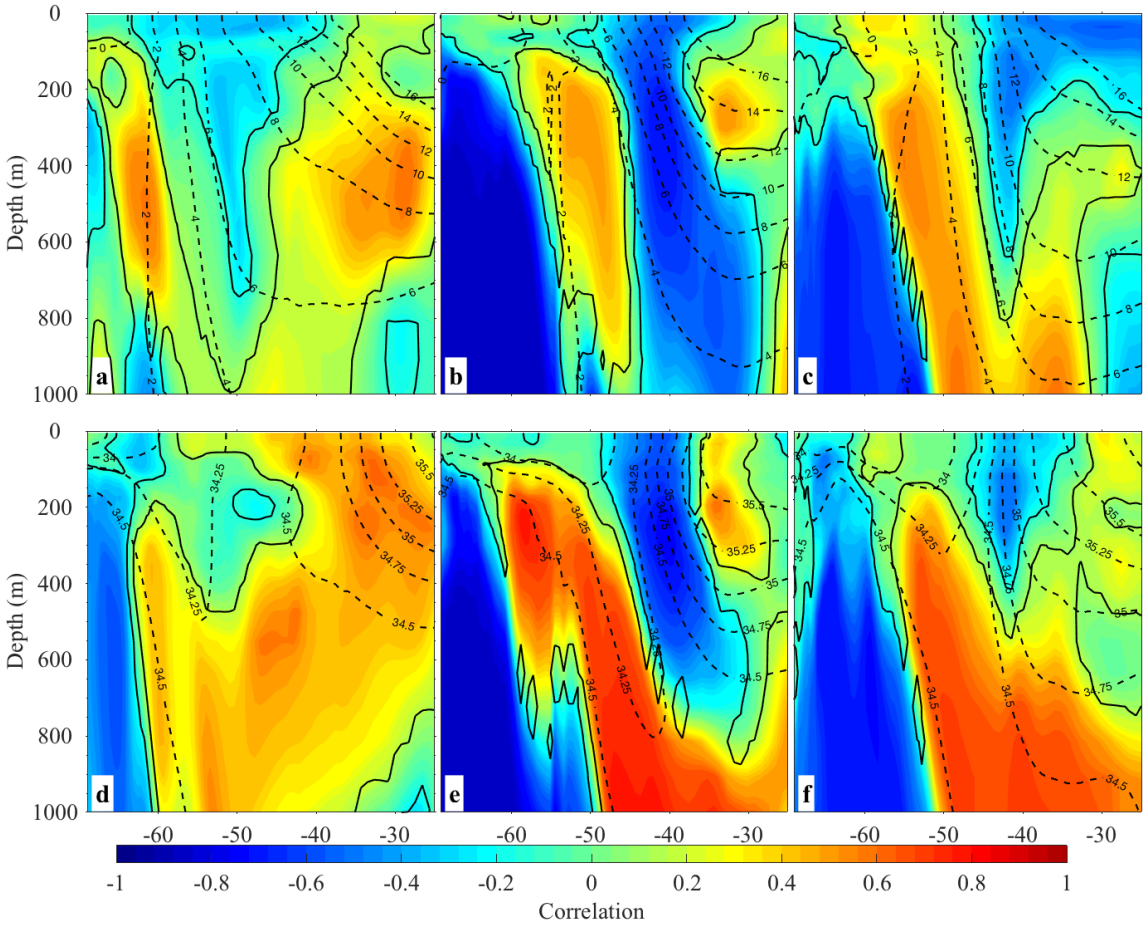

Figure 4.9. Correlation coefficients between the anomalous PF location using sea surface height contours and the zonal mean anomalous temperature (a-c) and (d-f) salinity for the Pacific (a,d), Atlantic (b,e), and Indian (c,f). Correlations significant at the 95% confidence level are contoured in black.

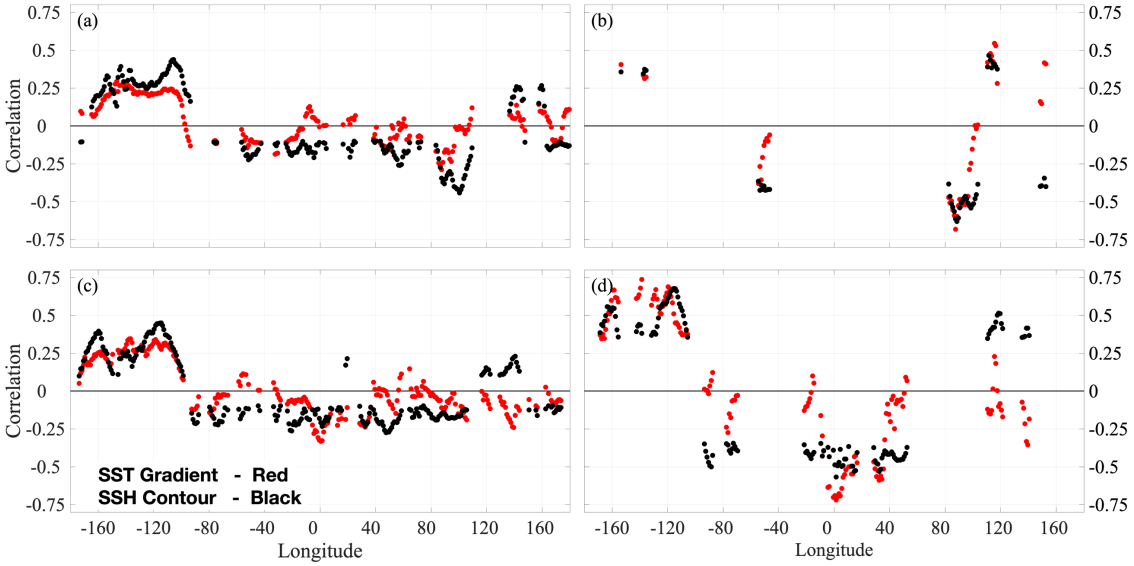

Figure 4.10. Correlation coefficients between the anomalous PF location and the Antarctic Oscillation (a) and Southern Oscillation(b). Only correlations significant at the 95% confidence level are plotted.

CHAPTER 5

CONFIRMATION OF ENSO-SOUTHERN OCEAN TELECONNECTIONS USING SATELLITE DERIVED SST[4]

[4]Ferster, B.S., B. Subrahmanyam, and A.M. Macdonald (2018). Confirmation of ENSO-Southern Ocean Teleconnections using Satellite Derived SST, Remote Sens., 10, 331; doi:10.3390/rs10020331.

Abstract

The Southern Ocean is the focus of many physical, chemical, and biological analyses due to its global importance and highly variable climate. This analysis of sea surface temperatures (SST) and global teleconnections shows that SSTs are significantly spatially correlated with both the Antarctic Oscillation and the Southern Oscillation, with spatial correlations between the indices and standardized SST anomalies approaching 1.0. Here, we report that the recent positive patterns in the Antarctic and Southern Oscillations are driving negative (cooling) trends in SST in the high latitude Southern Ocean and positive (warming) trends within the Southern Hemisphere sub-tropics and mid-latitudes. The coefficient of regression over the 35-year period analyzed implies that standardized temperatures have warmed at a rate of 0.0142 per year between 1982 and 2016 with a monthly standard error in the regression of 0.0008. Further regression calculations between the indices and SST indicate strong seasonality in response to changes in atmospheric circulation, with the strongest feedback occurring throughout the austral summer and autumn.

5.1. Introduction

Southern Ocean is a highly dynamic component of the global ocean circulation that plays a key role in the transport of heat, the uptake of carbon, and the global climate system (Sarmiento et al., 1998; Gille, 2002; McNeil and Matear, 2008; Montes-Hugo et al., 2009; Liu and Curry, 2010; Marshall and Speer, 2012; Landschützer et al., 2015; Cheng et al., 2017). The Southern Ocean circulation is largely wind driven. Changes in the Southern Hemisphere wind field drive sea surface temperature (SST) gradients that can support a

feedback mechanism and influence both the latitude of the Antarctic Circumpolar Current (ACC) and the distributions of heat and nutrients (Sun and Watts, 2002; Dong et al., 2006; Dong et al., 2007; Downes et al, 2011; Gille, 2014). Southern Hemisphere atmospheric variability exhibits a large number of modes, mostly influenced by large-scale low-frequency patterns (Simmonds and King, 2004) and has been known to play a major role in Southern Hemisphere weather and climate (Turner, 2004; Hendon et al., 2014). Due to the wave patterns associated with large-scale teleconnections, the largest temperature anomalies occur in the Amundsen-Bellingshausen Sea (Hendon et al., 2006). For a more in-depth analysis into the relationship between large-scale atmospheric teleconnections and Southern Ocean SST, refer to (Hendon et al., 2006). To analyze trends of Southern Hemisphere air-sea interactions, two patterns of atmospheric variability are compared with SST: the Antarctic Oscillation (AAO) and the Southern Oscillation (SO).

The AAO (also referred as the Southern Annular Mode) is a large-scale low-frequency pattern and is the dominant mode of atmospheric variability in the Southern Hemisphere Westerlies (Hendon et al., 2014). Previous studies found that the westerly winds have shifted south due to the increasing frequency of the AAO and the growing Antarctic ozone hole (Thompson et al., 2011; Thompson and Solomon, 2002) and significant changes have been observed in both the temperature and salinity of the Southern Ocean (Sarmiento et al., 1998; Gille, 2008; Durack and Wijffels, 2010). However, despite the increasing frequency of the AAO and the shifting Westerlies, statistical evidence indicates an insensitivity of the ACC and sloping isopycnals to decadal changes in wind stress (Böning et al., 2008). Within the Southern Ocean and Antarctic waters, previous studies have compared SST with the AAO (Ciasto et al., 2008; Ciasto et al., 2011; Xiao et

al., 2016) on weekly to monthly scales, noting the significant anomalies induced by the atmospheric pattern.

The SO is a measure of the Walker circulation in the tropical South Pacific. This circulation relates to variations in ocean temperatures and atmospheric pressure across the broad expanse of the tropical Pacific. The SO is also a metric for the El Niño-Southern Oscillation (ENSO) index. Negative (positive) SO index signifies warm (cold) SST across the eastern tropical Pacific and can therefore describe patterns similar to El Niño (La Niña) events. Additionally, the SO and El Niño (La Niña) were found to be negatively (positively) related to the Pacific-South American (PSA) wave pattern (Mo, 2000), which can have strong influences on SST, sea-ice, and atmospheric temperatures along Antarctica (Fogt and Bromwich, 2006; Welhouse et al., 2016; Cerrone et al., 2017). Fogt and Bromwich (2006) describes the strengthened influence of the AAO and SO during in phase periods, indicating the strong relationship between the atmospheric circulation and the effect on ocean dynamics. In this analysis, the statistical significance of the influence of teleconnections on Southern Ocean SST is investigated.

Hypothesizing that the SO has a greater influence than the AAO in the Southern Ocean and that both teleconnections drive warming (cooling) trends during positive (negative) phases of the oscillations, this analysis compares atmospheric teleconnections to Southern Ocean SST in both space and time. Investigation of the relationships between SST patterns and atmospheric variability with which they are associated provides a basis for improved understanding of Antarctic sea-ice and air-sea dynamics within the Southern Ocean.

5.2. Materials and Methods

5.2.1. Observational Data

Historically, in situ observations in the Southern Ocean have been sparse and made difficult due to harsh austral winter conditions. Southern Ocean in situ observations were particularly limited prior to the Argo float program, with most of the high-quality collections derived from repeat hydrography programs (Lyman and Johnson, 2008; Talley et al., 2016), such as the World Ocean Circulation Experiment (WOCE). Compared to in situ observations, satellites have relatively high spatial resolution and for SST a long temporal record extending back to the 1980's. The Optimal Interpolated Sea Surface Temperatures version 2 (OISST v2) product (Reynolds et al., 2007), utilizes statistically blended Advanced Very High Resolution Radiometer (AVHRR) data and in situ measurements to accurately represent the sea surface. OISST v2 is obtained from the National Oceanic and Atmospheric Administration (NOAA) Earth Science Research Laboratory Physical Science Division. OISST v2 (Reynolds et al., 2007) has 0.25° resolution spatially and temporal coverage dating back to September 1981. For this analysis, full-year only, high-resolution AVHRR data were used (1982–2016) to prevent seasonal bias, and all data points with satellite-derived fractional sea-ice in the high latitudes were removed.

Variability in SST anomalies is compared against proxies for large-scale, low frequency climate patterns of AAO and SO. Both the AAO and SO indices come from the National Centers of Environmental Prediction, Climate Prediction Center (NCEP, CPC). AAO index is computed from the leading empirical orthogonal function of 700 hPa height

anomalies between mid- and high latitudes from NCEP/NCAR (National Center for Atmospheric Research) reanalysis data (Kalnay et al., 1996). SO index is computed from standardized observed sea level pressure anomalies between Tahiti, French Polynesia and Darwin, Australia, divided by monthly standard deviations (Trenberth and Caron, 2000).

5.2.2. Methods

To analyze the teleconnections and standardized SST anomalies, multiple statistical tests are performed. To calculate standardized anomalies, the monthly mean climatology from OISST v2 (1982–2016) is subtracted from the monthly SST record and divided by the monthly standard deviation of OISST v2, effectively removing seasonality. Standardized anomalies typically provide a better representation on the magnitude of anomalies since the influences of dispersion have been removed. The linear regressions of standardized anomalies are calculated using whole years for the duration of OISST v2 SST, 1982–2016. Within the regressions and correlations, *p*-values are used to determine significance (alpha = 0.05). Positive (negative) indices are defined as those above (below) the 70th (30th) percentile, which is approximately 0.5 (−0.5). We define neutral years as those with indices between −0.5 and 0.5. Additional seasonal comparisons define austral summer as January through March and austral winter as July through September.

5.3. Results

We begin by addressing the relationship between SST and the large-scale AAO and SO teleconnections during the period 1982–2016. This period is used as it includes all full years in the OISST v2 data product. As described above, to reduce seasonal bias, standardized anomalies are compared against the large-scale patterns of AAO and SO

indices. Correlations between SST and the teleconnections (Figure 5.1a,b) relate positive anomalies in the mid-latitudes (30°S–50°S) and negative anomalies in the high latitude regions during positive phases. A positive AAO is associated with a poleward shift in the Westerlies, while a positive SO describes anomalously cold temperatures in the eastern Pacific (similar to La Niña events).

During positive AAO years, the shift in the Westerlies correlates with anomalously warm surface waters in the mid-latitude Atlantic and Indian basins and a broad negative anomaly in the South Pacific (Figure 5.1a). A similar spatial pattern exists during positive SO years (Figure 5.1b). Positive SO years correlate with large-scale negative standardized SST anomalies in the high latitude Pacific and positive anomalies in the mid-latitude Pacific, along the west coast of Australia, and south of 45°S in the Atlantic. The spatial extent of significant SST anomaly correlations with the SO is larger than the correlations between SST and the AAO. Between the mid-2000's and 2014, both indices have been mostly in a positive phase (Figure 5.1c). When both indices are in the positive phase, spatial correlations relate increasing negative anomalies along the Antarctic coast with increasing positive anomalies in portions of the Ross and Weddell Seas and the sub-tropical Southern Ocean, similar to Ciasto et al. (2011).

The influences of teleconnections are further explored through a more detailed analysis of the standardized SST anomalies (Figure 5.2). Spatial linear regressions from 1982 to 2016 in the Southern Ocean (Figure 5.2a) show significant large-scale surface warming (positive) in the mid-latitude Southern Ocean, the southern Indian Basin (60°E–120°E), and the Amundsen Sea sector. In addition, significant negative trends in the South Pacific Basin and Drake Passage region are seen. An estimate of the Southern Ocean trends

suggests a mean value of 0.0142 per year, a median of 0.0154 per year, and a distribution negatively skewed towards negative trends.

Comparing one-year averaged anomalies, we look to analyze two recent examples: a year with opposing index values and another with similar in-phase index values. In doing so, we explore the spatial regions and magnitudes of positive and opposing index years. Using Figure 5.1c, the years 2016 and 2010 were selected for each comparison respectively. The 2016 indices are described by a strong negative SO in the beginning of the year, changing to a strong positive SO by the end of the year with a consistently positive AAO (see Figure 5.1c). That is, the phases of the indices are mostly out of sync. The pattern of standardized SST anomalies (Figure 5.2b) from 2016 does show the strong similarities to the positive phases of both AAO and SO (i.e., negative sub-polar and positive sub-tropical anomalies), but also from the negative SO phase. The potency of the strong negative SO value (Figure 5.1b) is seen in the anomalously warm SSTs in the eastern and central sub-tropical Pacific Ocean (Figure 5.2b), both of which overshadow the values forced by the positive SO months.

The 2010 mean standardized SST anomalies (Figure 5.2c) were the start of successive La Niña years (denoted in Figure 5.1c) and a positive AAO. Most notable are the anomalously warm temperatures in the sub-tropical Pacific, South Atlantic, and western Indian Basins. Moreover, there are strong negative anomalies in the South Pacific and in the South Indian Ocean (near 60°E). The pattern of 2010 positive and negative anomalies (Figure 5.2c) shares strong similarities with the positive and negative SST and SO correlations (Figure 5.1b), showing the strong influence of the in-phase oscillations on SST.

Temporal analysis of the mean Southern Ocean SST (Figure 5.2d) suggests warming at a rate of 0.0142 per year between 1982 and 2016 (0.0092 °C per year if not standardized), with a standard error of 0.0008. The average was taken between 30°S and 70°S for each month. Throughout the 35-year period, there was a net warming of approximately 0.50 based on standardized anomalies (approximately 0.32 °C if not standardized). A spatial comparison indicates that positive index months correlate to broad-scale warming in the mid-latitudes that supports the warming trend. To show the more recent relationship of in phases indices, Figure 5.3 depicts the standardized SST anomalies for AAO positive and SO neutral, AAO neutral and SO positive, and both AAO and SO positive indices. In this comparison, the opposing relationships of neutral-phase indices mitigate anomalies. However, during in-phase months of AAO and SO indices, the anomalies are greater in magnitude and broader spatially compared to either out-of-phase relationship, similar to the results of (Fogt and Bromwich, 2006).

A comparison of monthly and yearly averaged standardized SST anomalies (Figure 5.4) mark contrasting differences between the temporal scales of AAO and the SO. The monthly (Figure 5.4a) and yearly (Figure 5.4b) averaged standardized SST anomalies during positive AAO events both have negative anomalies in the Pacific Basin and positive anomalies in the Atlantic and Indian Basins. On longer time-scales, this yearly pattern of anomalous temperatures is stronger than monthly averaged. Differences in the yearly and monthly AAO anomalies (Figure 5.4c) show the stronger (red) yearly signal, particularly east of the Greenwich Meridian and south of Australia to the dateline. Yearly anomalies are weaker (blue) in the high latitude Indian, the mid to high-latitude Atlantic and mid-latitude Central Pacific.

Although global air-sea interactions are heavily influenced by large-scale teleconnections, seasonal regressions derive a response in SST to changes in index values (Figure 5.5). In both instances, the largest coefficients of regression occur in austral summer and autumn, while the weakest coefficients arise in austral winter. Similar results for SST and ENSO were previously described in Welhouse et al. (2016) and Fogt and Bromwich (2006). Based on these findings, spatial changes in austral summer indices can be used to depict linear changes in temperature. However, minimally significant regressions between austral winter anomalies and the indices suggest a potential non-linear or lag relationship.

5.4. Discussion

Analyzing correlations and mean standardized anomalies allow for the interpretation of how large-scale teleconnections influence the Southern Ocean. Strong positive indices of both the AAO and SO (La Niña) induce broad-scale cooling in the high latitudes of the Southern Ocean and warming in the mid-latitudes and Weddell Sea. Each index is seen to drive spatial anomalies on a magnitude of 0.5 and anomalies approaching 1 when both indices are in-phase. Within Figure 5.1a and 1b, the spatial correlations of the SO are more highly correlated spatially and based on magnitude, displaying the overlaying influence of the SO on the Southern Ocean SST. This result is important as the mid-2000's through 2012 were largely in-phase positive oscillations, associated with large-scale negative anomalies in the high latitudes and positive anomalies in the mid-latitudes and Weddell sea. More importantly, the spatial pattern in the temporal linear regression of SST is spatially similar to SST anomalies in 2010, a year marked by a strong La Niña period and a positive AAO index value, showing the importance of in-phase oscillations on SST. The continual positive indices within the 21st century would therefore be strongly contributing to

the positive trend in Southern Ocean mid-latitude SST and negative trend within the Southern Hemisphere high latitudes.

The patterns of SST anomalies seen during positive SO monthly (Figure 5.4d) and yearly (Figure 5.4e) periods are similar, with intensification throughout the year in both the Indian and Pacific Basins (Figure 5.4f). This temporal disparity is most likely due to the time required for an Equatorial-Tropical Pacific phenomenon to influence large regions. A distinguishing feature of these patterns is that the magnitude of positive SO events in the Pacific Basin is greater than those associated with the AAO. The potential implication is that the SO plays a dominant role in the Southern Ocean. Furthermore, differences in yearly and monthly averaged anomalies are comparatively large. Thus, the longer duration of AAO and SO events could be an effective means of supporting or driving long-term trends.

SST anomalies can still be influenced by localized processes and feedback mechanisms. In years where the AAO and SO are increasingly positive, the Westerlies shift poleward and anomalously cooler temperatures are found in the high latitudes, with warmer temperatures in the mid-latitudes. There are breaks in the trend when strong El Niño events occur (negative SO), driving temperature changes that oppose the existing trend. Although this analysis supports the long-term increase in mean Southern Ocean surface temperature found by earlier analyses, it suggests that while the Atlantic and Indian Basins continue to warm, there has been significant cooling in the South Pacific as a result of the most recent patterns in the AAO and SO.

5.5. Conclusions

In summary, an analysis of satellite-derived SST observations provides statistical grounds for measuring and understanding the spatial correlations between SSTs and global atmospheric teleconnection patterns. We find SSTs to be significantly correlated to both the AAO and the SO, with larger magnitude of anomalies associated with the SO events. Large-scale spatial patterns of both the AAO and the SO are significantly correlated to sea surface temperatures in Southern Ocean, driving significant cooling in Antarctic sub-polar regions and warming in the Southern Hemisphere subtropics. The recent in phase positive AAO and SO patterns are simultaneously driving significant cooling in the high latitude Pacific basin, despite broad-scale warming throughout the Southern Ocean at a rate of 0.0142 per year. We further find that the strong in phase austral summer and autumn relationships are driving the most significant changes. Our analysis, which suggests the potential for a continuous warming trend should the AAO and SO spend extended periods in their positive phases, provides strong grounds for the promotion of continued monitoring of the high latitude SST.

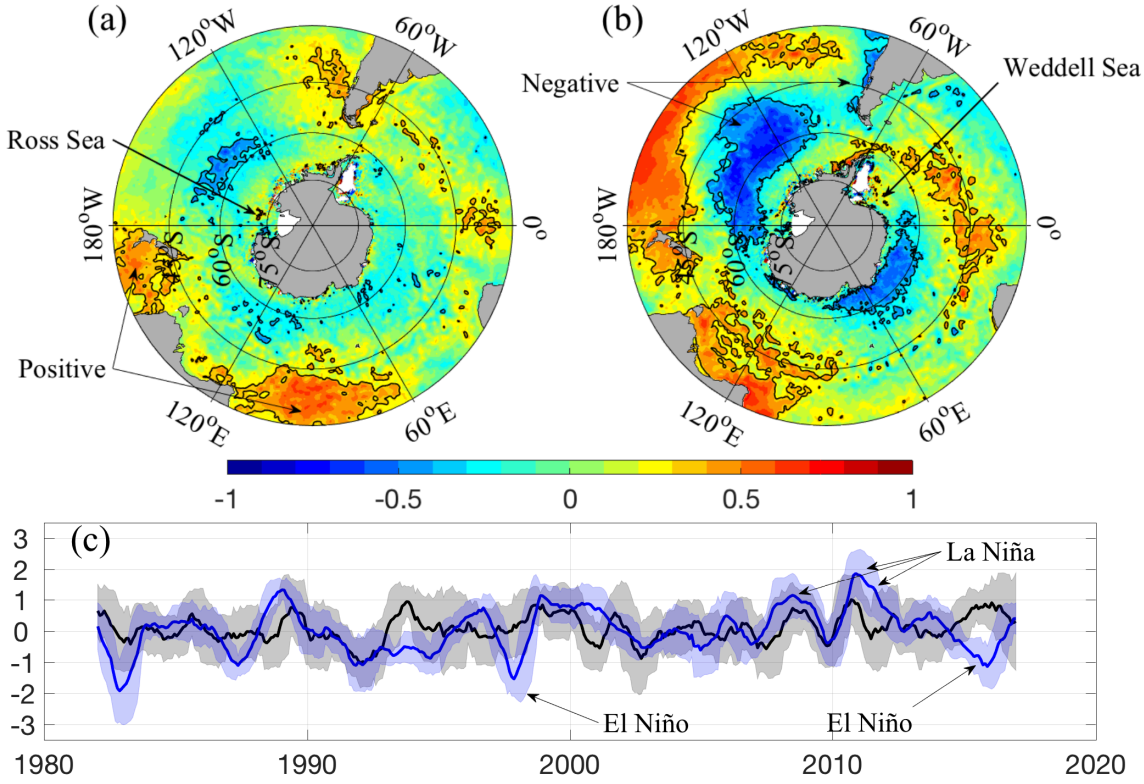

Figure 5.1. Pearson's correlation coefficient between standardized SST anomalies and the (a) Antarctic Oscillation (AAO) and (b) Southern Oscillation (SO). Negative (positive) coefficients are blue (red), and indicate decreased (increased) standardized SST anomalies. Coefficients interior to the black contour are significant (alpha = 0.05). (c) The 12-month running mean of AAO (black) and SO (blue) indices between 1982 and 2016, the shaded regions indicate the uncertainty.

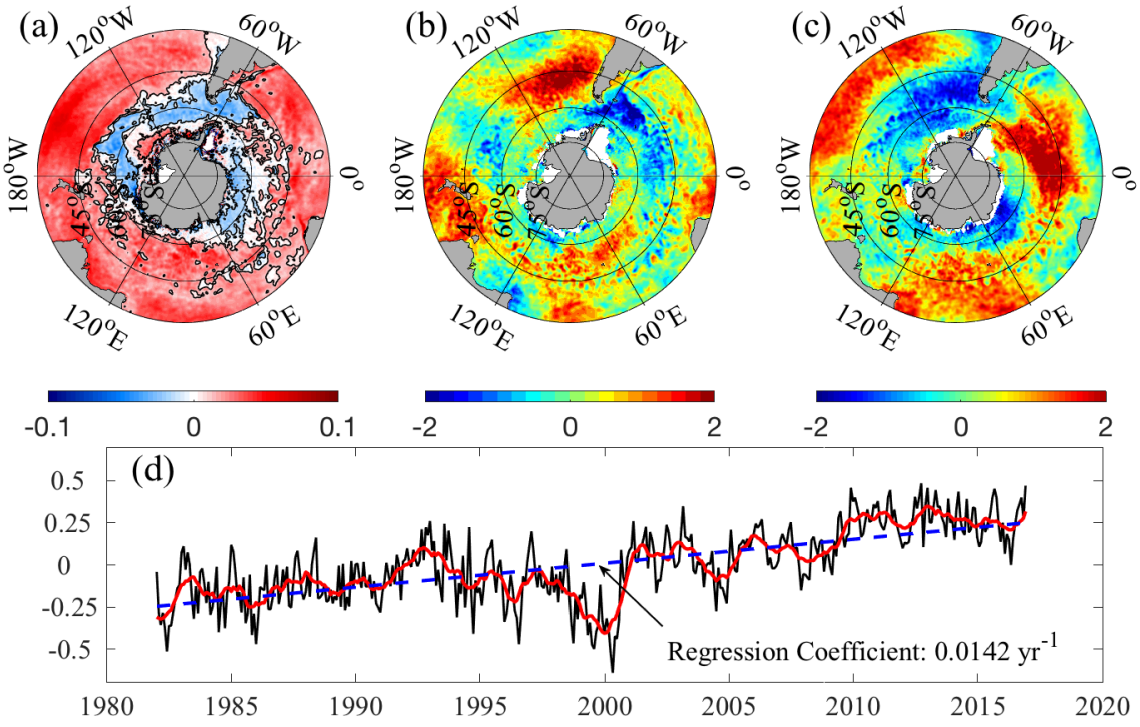

Figure 5.2. The 1982–2016 sea surface temperature (SST) coefficient of regression (year^{-1}) (a), mean standardized SST anomalies during 2016 (b), and 2010 (c). In (a), values interior to black contour lines represent significant trends (alpha = 0.05). (d) The monthly averaged standardized SST anomalies (black) in the Southern Ocean (30°S–70°S), 12-month running mean (red), and the linear regression (dashed blue). The coefficient of regression is 0.0142 year^{-1} and the coefficient of determination (r2) is 0.436. The temporal monthly standard error in regression is 0.0008.

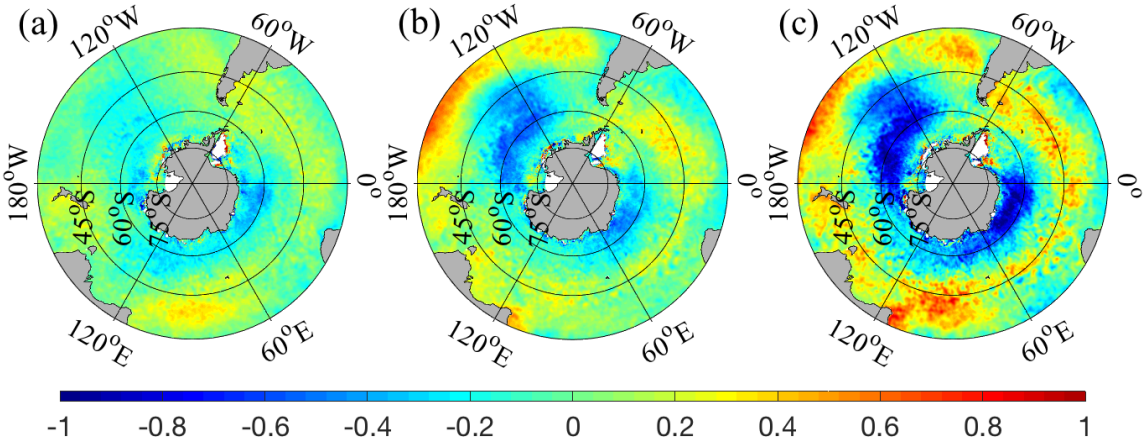

Figure 5.3. Monthly mean standardized sea surface temperature (SST) anomalies (°C) during (a) positive Antarctic Oscillation (AAO) and neutral Southern Oscillation (SO) months, (b) neutral AAO and positive SO months, and (c) both positive AAO and SO months. In each instance, a positive (negative) index is defined as greater (less) than 0.5 (−0.5) and neutral between −0.5 to 0.5.

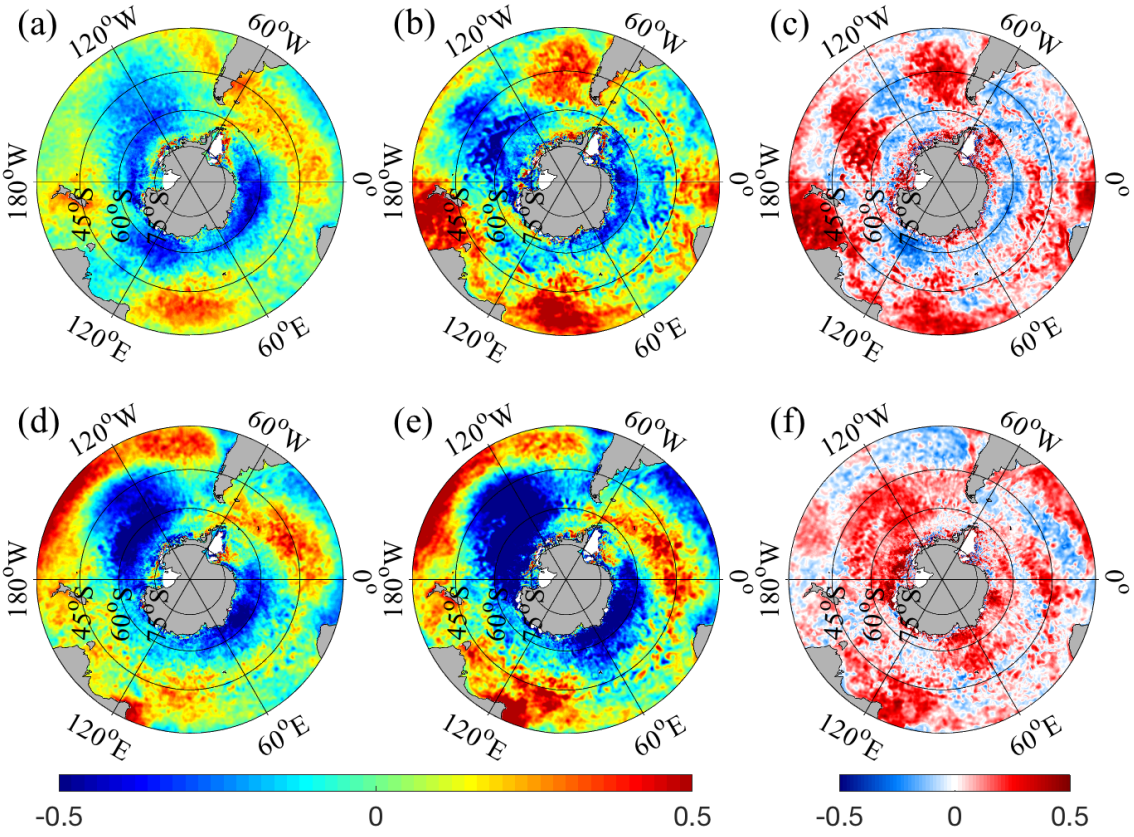

Figure 5.4. Monthly mean sea surface temperature (SST) standardized anomalies during positive Antarctic Oscillation (AAO) (a) and Southern Oscillation (SO) (d) months and (b) and (e) are standardized temperature anomalies during positive AAO and SO years respectively. (c) and (f) are the absolute value of yearly averaged anomalies minus the absolute value of monthly averaged anomalies. Red (blue) depicts yearly averages are greater (weaker) than monthly. In each instance, a positive index is defined as greater than 0.5.

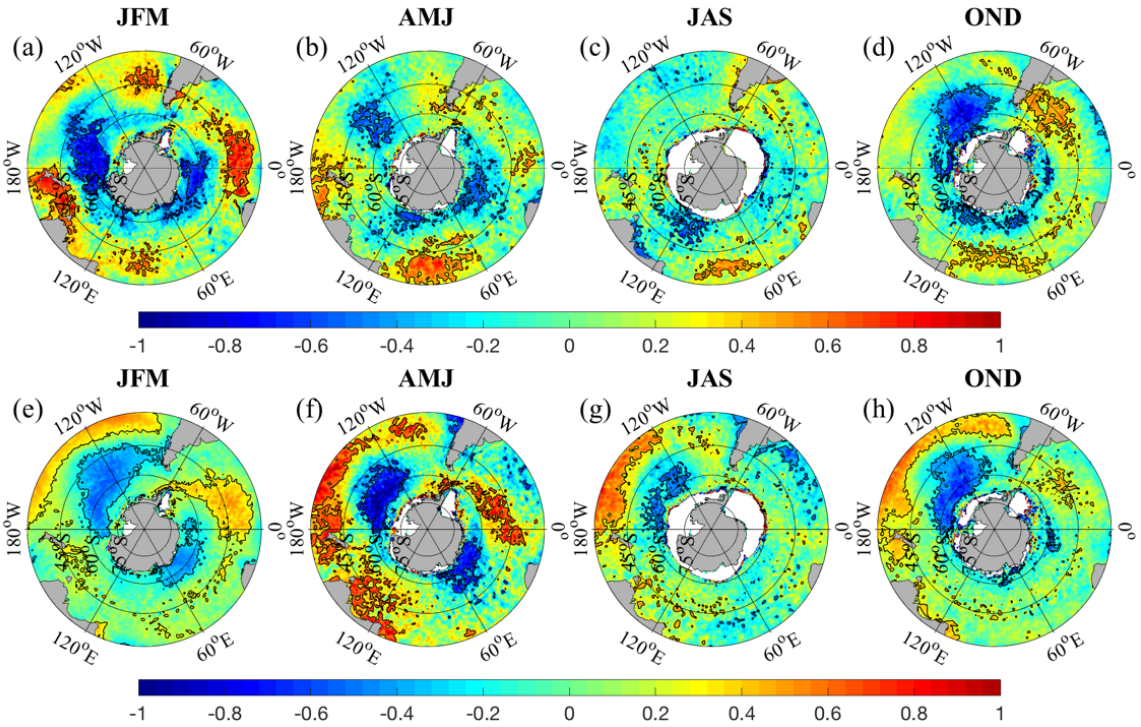

Figure 5.5. Coefficients of regression between the Southern Oscillation (AAO) (a–d) and standardized sea surface temperature (SST) anomalies (°C) from 1982 to 2016. (a) is monthly anomalies averaged over January to March (austral summer), (b) April through June, (c) July through September (austral winter), and (d) October to December. The coefficients of regression between the SO (e–h) SST anomalies are through the same temporal scale as (a–d) respectively. The largest coefficients occur with AAO and SO during the austral summer and autumn, while the smallest coefficients occur in austral winter.

CHAPTER 6

RECENT CHANGES IN SOUTHERN OCEAN CIRCULATION AND CLIMATE[5]

[5]Ferster, B. S., B. Subrahmanyam, and A. Arguez (2018). Recent changes in Southern Ocean Circulation and Climate, *IEEE GRSL*, pp. 1-5, doi:10.1109/LGRS.2018.2880589.

Abstract

The Southern Ocean is an essential component of ocean circulation and climate variability. The strength and position of the Southern Hemisphere (SH) Westerlies are largely thought to be driving the variability and recent trends in the Southern Ocean. Analysis in the SH winds illustrate increasing winds in the high latitudes, while decreasing in the mid-latitude region of ± 5 cm s^{-1} $year^{-1}$. Mean surface temperatures (heat content) are significantly increasing at 0.0066ºC $year^{-1}$ (3.8 W m^{-2}), although significantly decreasing within the high latitude Pacific and Atlantic basins. Sea level change indicates the median regression in the SH is 3.1 mm $year^{-1}$, despite decreasing in the central South Pacific. Our analysis concludes the surface winds are driving regional changes sea level, heat content, and surface temperatures in the SH high latitudes, significantly contributing negative trends in the central South Pacific.

6.1 Introduction

The Southern Ocean (SO) plays a pivotal role in the global-scale meridional overturning circulation, working to distribute mass, heat, and freshwater between the Atlantic, Pacific, and Indian Oceans (Marshall and Speer, 2012). The SO is largely wind-driven, interacting with the Southern Hemisphere (SH) Westerlies to drive the Antarctic Circumpolar Current (ACC). The Westerlies are known to exhibit large natural variability, oscillating on week-to-centennial time scales (Thompson and Wallace, 2000; Thompson and Solomon, 2002). Recent studies have found that the Westerlies have shifted southward, largely driven by the Antarctic ozone hole (Thompson and Solomon, 2002; Thompson et al., 2011), and is thought to be a major influence into the recent restructuring of the ACC

fronts (Dong et al., 2002; Downes et al., 2011), which could have major implications on circulation, surface mixing, and climate variability.

Significant changes in SO temperature and salinity (Gille, 2002; Durack and Wijffels, 2010) have been observed through observational data, and suggested to be driven the changes in the Westerlies and ACC. Further significant changes in ocean heat content (OHC) (Willis et al., 2004), sea level rise (Rye et al., 2014), and sea ice extent (Kwok et al., 2016) have all been observed through satellite and *in situ* based data analyses. As a result, regional-scale changes in wind, salinity, and temperature trends have all be observed to influence thermodynamic and dynamic forcings, such as sea ice formation or surface mixing. The stability of the SO relates to global significance, regulating and transporting heat, nutrients, and gases throughout the global oceans.

Historically, *in situ* observations have been sparse in the SO, particularly prior to the Argo float program (Lyman and Johnson, 2014). For satellite products such as surface winds, sea level, and sea surface temperature (SST), high-quality data with improved spatial resolution extends back through the 1990's. For this analysis, the long temporal time-scales of the products are ideal to analyze the SO trends and variability. An investigation into the surface winds, SLA, SST, and OHC allows for an in-depth examination on the current state of the SO climate and circulation. Expected results are increased SST in the mid-latitude SO and decreased SST in the high latitude SO, with similar spatial results in OHC. We further hypothesize increased magnitude of surface winds and SLA.

6.2 Data and Methodology

6.2.1 Satellite Observations

In analysis of winds, we have used the daily NOAA's blended sea winds product (research quality version 1.2). The blended product contains wind vector velocities on daily 0.25º resolution with daily coverage from July 1987 through 2017, utilizing multiple satellite derived winds to allow global coverage. The daily products were binned and averaged for monthly time scales in this analysis. Further description on the data can be found through (Zhang et al., 2006; Peng et al., 2013). For this analysis, the vectors are used to estimate wind speed, and is therefore a magnitude.

Sea surface height (SSH) data can be downloaded through Copernicus Marine Environment Monitoring Service in near real–time and reprocessed products that allow for quality control checks and cross–calibration processes to remove residual orbit error. The multi–mission gridded SLA and anomalous currents were derived through the 20–year mean of SSH (1993 to 2012). Both reprocessed and near-real time SLA products are used in this analysis are from January 1993 through December 2017 in 0.25º spatial resolution.

Liquid water equivalent thickness anomalies (LWE) is estimated through the twin satellites Gravity Recovery and Climate Experiment (GRACE) (Chambers, 2012). This mission measures regional mass changes of the Earth's water of land, ocean, and ice regions. In this analysis, GRACE LWE is analyzed from 2002 through 2017 in monthly format with 1º resolution (Chambers, 2012). For more information regarding the estimation and validation of GRACE monthly mass release 5.0, please refer to Chambers and Willis (2010) and Chambers and Bonin (2012). Methods of Chambers et al. (1997) and Jayne et

al. (2003) are used to estimate OHC anomalies from sea level and LWE anomalies.

Sea surface temperature data from A Group for High Resolution Sea Surface Temperature (GHRSST) version 2.0 (Canada Meteorological Center, 2012) can be downloaded globally from September 1991 through 2016 (Brasnett, 2008). This level 4 product combines infrared and microwave satellite–derived data with in situ observations to assimilate a high resolution product. The product is in 0.2º spatial resolution globally and is used from 1992 through 2016. For this analysis, high resolution GHRSST data was used for full years (1992–2016) to prevent seasonal bias, and have removed all data points with satellite–derived fractional sea–ice in the high latitudes.

6.2.2 Methods for Anomalies and Statistical Tests

To estimate the anomalies of surface winds, sea level, and SST, the twenty-year monthly climatological means (1993 through 2012) have been removed, the same time period to that of the processed SLA product. OHC anomalies use the mean of 2005 to 2012 based on the years of available LWE data. To estimate trends, a robust regression of the yearly averaged anomalies is used to better account for outliers and autocorrelation. Trends are tested under the assumption of being zero and are considered significant (non-zero) using an alpha of 0.05. In each instance, grid cells with sea-ice are treated as missing values and are ignored. The trends are presented in units year^{-1}. The ACC region is defined as 45ºS to 60ºS, the mid-latitude area is 30ºS to 45ºS, and the high latitudes are poleward of 60ºS.

6.3 Results and Discussion

6.3.1 Surface Winds

Figure 6.1 illustrates the increasing wind speeds in the ACC region and decreasing magnitude in the mid-latitude regions; the regressions contoured in black are significantly different from zero. The 1988-2017 trend indicates rates approaching ± 5 cm s^{-1} $year^{-1}$, a mean (median) of 1.0 (3.1) mm s^{-1} and a standard deviation of 7.0 cm s^{-1} $year^{-1}$. These trends are roughly an order of magnitude smaller than the climatological anomalies and are found to have significant trends in much of the ACC and the mid-latitude Indian basin. Moreover, there are significant positive regressions along the eastern boundary of each ocean basin (mid-latitudes) and a negative regression throughout much of the central and western boundaries in each basin.

The SH winds have been shown to have intensified and shifted poleward in recent decades (Thompson and Solomon, 2002; Thompson et al., 2011). In the most recent decade of 2010 through 2017, surface wind anomalies drastically increase within the ACC region of the Atlantic and Indian basins and decrease within the central South Pacific and Indian Oceans. There are large anomalies found along the Drake Passage, New Zealand, and the western South American and South African coasts. The large magnitude of the most recent decade anomalies suggests the intensification of surface winds since 2010. The ACC region in the Atlantic and Indian basins show large anomalies and thus relate to the strong positive trend. These anomalies further indicate the recent weakening of winds in the South Pacific, despite the overall intensification from 1988 through 2017.

6.3.2 Sea Level Anomalies

Figure 6.2 depicts the mean decadal SLA and trends, with significant regressions contoured in black. Similar to surface winds, the largest magnitude of anomalies occurs during the 2010-2017 period. Within this decade, the mean (median) SLA is 5.8 cm (5.7 cm). Regions like the western South Pacific and Atlantic basins indicate the mean 2010-2017 anomalies are approaching 10 cm. These regions denote the largest temporal trends, which show the large-scale amplification of anomalies through the recent decade. Within the South Indian, Atlantic, and Pacific Oceans, the western boundaries are significantly increasing in sea level, while significantly decreasing in the central South Pacific (160ºW–120ºW, 50ºS–60ºS) and Atlantic-Indian exchange. These SLA trends further show the intensification of the SH sea level rise. Much of the SH reveals statistically significant trends, the mean (median) of 3.1 mm year^{-1} (3.0 mm year^{-1}) and a standard deviation of 2.0 mm year^{-1}. Regions such as the central and western South Pacific, Indian, and Atlantic Oceans suggest significant regressions larger than 6.0 mm year^{-1}, and pose as large outliers. Despite such large positive trends, the South Pacific basin with the ACC region, Drake Passage, and within the Agulhas retroflection all indicate significant negative trends of roughly –1.6 mm year^{-1} (median).

Past studies argue the global average sea level rate increased from 1.5 to 3.2 mm year^{-1}, largely attributed to ocean warming and mass loss from glaciers and ice sheets (Church et al., 2013). During 2003 to 2011, sea level rate slowed to 2.4 mm year^{-1} Cazenave et al., 2014), but could be largely influenced by land-driven hydrology and water storage (Reager et al., 2016). Both the median and mean sea level rise rate for the SO in this analysis is ~3.1 mm year^{-1} and a standard deviation of 1.8 mm year^{-1} from 1993

through 2017, which is consistent with previous global mean rates. However, as shown in Figure 6.2, there are regions in the SH that are greater than 6.0 mm year^{-1} and –1.6 mm year^{-1}. Moreover, similar to the anomalies in surface winds, the most recent decadal anomalies suggest the amplification of sea level trends from the 2000 to 2009 period. These results suggest the recent sea level trends are greater than both the previous decade and the 1993-2017 trend.

6.3.3 Ocean Heat Content Anomalies

Figure 6.3 shows OHC anomalies have largely increased between 2010 and 2016, similar to wind and SLAs. There are strong positive anomalies in the western South Pacific and Indian Oceans and near the Drake Passage. The fifteen-year trends illustrate that much of the South Pacific and Indian Oceans and the central South Atlantic Ocean have statistically significant positive trends. The mean (median) positive regression is 6.1 (4.4) W m^{-2}. Significant negative trends occur within the ACC region of the Pacific basin and the Atlantic-Indian basin exchange. The mean (median) negative regression is –4.7 (–3.3) W m^{-2}. The mean (median) regression in the entire SO is 3.8 (3.5) W m^{-2} and a standard deviation of 7.8 W m^{-2}.

Chambers and Bonin (2012) concluded sea surface height data in the SO is strongly correlated with OHC anomalies from 300 to 1800 meters depth. Results for OHC anomalies and trends in this analysis are spatially similar to the of the SLA, despite including the ocean mass data in estimating OHC. The similarities stress the importance of OHC in sea level within the SO. A difference between OHC and SLA trends are the negative anomalies along the Antarctic coast (0º–60ºE) in heat storage rates. This trend

indicates negative heat storage values, but is collocated in a region of increasing SLA. This could be a result of the different temporal mean periods, salinity, or runoff.

The regressions along the Antarctic coast are comparatively large. OHC anomalies derived from SLA and ocean mass allows for reduced errors in regions like the high latitude SO (Jayne et al., 2003); however, poleward of the ACC is known to be dominated by salinity rather than temperature. Taking this into consideration, the results poleward of 60ºS should be taken with caution and examined with the use of salinity. (Willis et al., 2004) has shown global OHC to be steadily increasing between 1993 to 2003, increasing globally 0.86 W m^{-2} during that time. The SO is known to experience the greatest global ocean warming from 1960 to 2015, with large changes OHC to depths of 2000m (Cheng et al., 2017). Their results suggest the SO contributes 30% (28%) of the global OHC increase from 0–2000m (0–700m) between 1998 to 2015. Cheng et al. (2017) concluded that the SO plays a major role in global heat storage through the overturning circulation, increasing ~4.26 x 10^{22} J between 1998 to 2015 in the SO along.

6.3.4 Sea Surface Temperature Anomalies

The more recent decade implies the large-scale warming throughout the mid-latitude SO. The 2010-2016 mean anomalies are largely positive during this period, indicative of the temporal regression and broad-scale warming through the mid-latitude region. The 2010-2016 mean anomaly is 0.083ºC, larger than either of the other periods. This displays the clear warming pattern and shows the increased magnitude of anomalies in the recent decade. The mean SST regression (standard deviation) is 0.0066 (0.016) ºC $year^{-1}$ in the SO, shown in Figure 6.4. The large variability in the trends are a result of the

differences in the mid- and high-latitudes. Decadal analyses of SH SSTs show positive trends in much of the mid-latitude and ACC region and negative in the South Pacific basin (50°S to 60°S), the Drake Passage, and Agulhas region. Regressions are statistically significant within much of the SO. The South Pacific and Atlantic-Indian exchange show significantly negative trends and the mid-latitude SO are significantly positive. These results display significant cooling (negative) trends in SST in the high latitude Southern Ocean and warming (positive) trends within the Southern Hemisphere sub–tropics and mid-latitudes. The largest trends approach –0.1ºC year^{-1} in the Agulhas retroflection, but is approximately –0.015ºC year^{-1} in the Drake Passage, central South Pacific, and the Atlantic-Indian exchange. Despite these large negative trends, the mean high-latitude trend is 0.004ºC year^{-1}, a lower rate than the mid-latitudes.

The mid-latitude regions of the western South Atlantic, Pacific, and Indian Oceans are increasing by ~0.050ºC year^{-1}, nearly four times greater than the mean mid-latitude trend of 0.013ºC year^{-1}. Similar SST trends are discussed in Ferster et al. (2018) using AVHRR (Advanced Very High Resolution Radiometer) data between 1982 and 2016. These results illustrate that there are significant trends in SST, warming or cooling rates are significantly different from zero throughout much of the mid-latitudes.

6.3.5 The Role of Surface Winds in the Southern Ocean Climate

Surface winds are important to study due to relevance on ocean dynamics. Surface winds play a strong role in forcing ocean currents and work to induce ocean mixing. Within the SO, the strong winds drive water circulation and influences the vertical structure and

distribution of heat, nutrients, and gases. In the SH, there are strong correlations and regressions (Figure 6.5) between SLA, OHC, and SST with surface winds anomalies.

SLAs are negatively correlated with surface winds in the western South Pacific, the South Indian basin, and the Agulhas Current and positively correlated throughout much of the ACC and high latitude Atlantic and Indian basins. Statistically significant correlations approach ±0.8, indicating the strong relationship. Positive regressions along the Agulhas retroflection, the Malvinas, and the high latitude Indian basin have slopes greater than 10 cm of SLA per 1 m s^{-1} anomaly in wind speed, with maximum significant values in these regions of 25.2 cm per m s^{-1}. The median positive significant value is 4.45 cm per m s^{-1}. The significant negative regressions suggest slopes as large as –16.2, but a median value of –3.24 cm per m s^{-1}. These results illustrate that surface winds are significantly driving SLA in the high latitude Atlantic and Indian basins, western South Pacific, and the South Indian Ocean.

Correlations between the SH wind and OHC anomalies indicate a significant positive relationship throughout much of the ACC and a negative relationship in the southeastern Indian Ocean and high latitude South Pacific. Significant correlations in the high latitude are near ±0.9, noting the strong role of the surface wind speed on OHC. The correlations of OHC and SLA are similar for the high latitude regions; suggesting much of the SLA and OHC are positively driven by the surface winds in the Atlantic and Indian basins and driving negative OHC anomalies in the South Pacific basin. The median (maximum) statistically significant high latitude positive regression is 1.56 (6.62) GJ per m s^{-1} and negative regression is –1.21 (–7.05) GJ per m s^{-1}. These results show the broad-

scale ocean warming in the South Atlantic and Indian basin high latitudes and cooling in the South Pacific basin as a result of wind speed anomalies.

Correlations with SST anomalies indicate a significant negative relationship throughout much of the South Pacific, Indian, and Atlantic Oceans, the Drake Passage, and the Malvinas region. The median (maximum) significant correlations are ± 0.50 for positive (0.99) and negative (–0.78) values. Positive relationships in the mid-latitude Western Indian and Atlantic basins are likely associated with wind–driven currents moving warm waters from the tropics to the mid-latitudes. Negative correlations in the high latitude Pacific, South Atlantic, and Eastern Indian basin are driven by upwelling waters and surface current, where increasing winds are associated with decreasing SST. The median (max) significant positive regression is 0.37 (1.76) ºC per m s^{-1} and negative regression of –0.24 (–0.99) ºC per m s^{-1}. The slopes suggest broad-scale surface cooling in the South Pacific, Atlantic, and Indian basins and warming in the Malvinas and Agulhas region as a result of positive changes in wind speed.

6.4 Conclusion

The SO is a major driver in global circulation and offers insight into understanding global-scale climate changes and variability. This analysis explores recent decadal changes in the SO winds, SLA, OHC, and SST. Analysis of the SH winds illustrate the intensification of 5 cm s^{-1} $year^{-1}$ throughout the high latitudes and much of the eastern ocean basins, while decreasing intensity in the mid-latitudes. The SH mid-latitudes are shown to be increasing in sea level, SST, and OHC. The high-latitudes and Antarctic coast are largely decreasing in heat content and sea level in the central South Pacific and Atlantic-

Indian basin exchange, but show negative trends outside these regions. The mean SST (OHC) trend in the SO is 0.0066ºC year^{-1} (3.8 W m^{-2}). SST (OHC) are significantly increasing in the mid-latitude regions by 0.013ºC year^{-1} (4.4 W m^{-2}) and decreasing within the high latitude Pacific and Atlantic basins by –0.015ºC year^{-1} (–3.3 W m^{-2}). Trends in SLA indicate the median SO sea level rise is approximately 3.1 mm year^{-1}, with regions such as the western South Pacific and Atlantic greater than 6.0 mm year^{-1}. Conversely, the central South Pacific, Drake Passage, and the Atlantic-Indian basin exchange are all regions of negative trends (–1.6 mm year^{-1}).

Mean decadal anomalies suggest the recent amplification and acceleration of changes in surface winds, sea level, OHC, and SST during the 2010-2017 period. The recent anomalies display increased trends since the 2000-2009 period, further driving the 1993-2017 regressions. Correlations and regressions further indicate surface winds are significantly driving changes in the SO; driving increased SLA (4.45 cm per m s^{-1}) and OHC (1.56 GJ per m s^{-1}) anomalies in the high latitude Atlantic and Indian basins, while supporting decreased SLA (–3.24 cm per m s^{-1}), OHC (–1.21 GJ per m s^{-1}), and SST (–0.24 ºC per m s^{-1}) in the high latitude South Pacific Ocean.

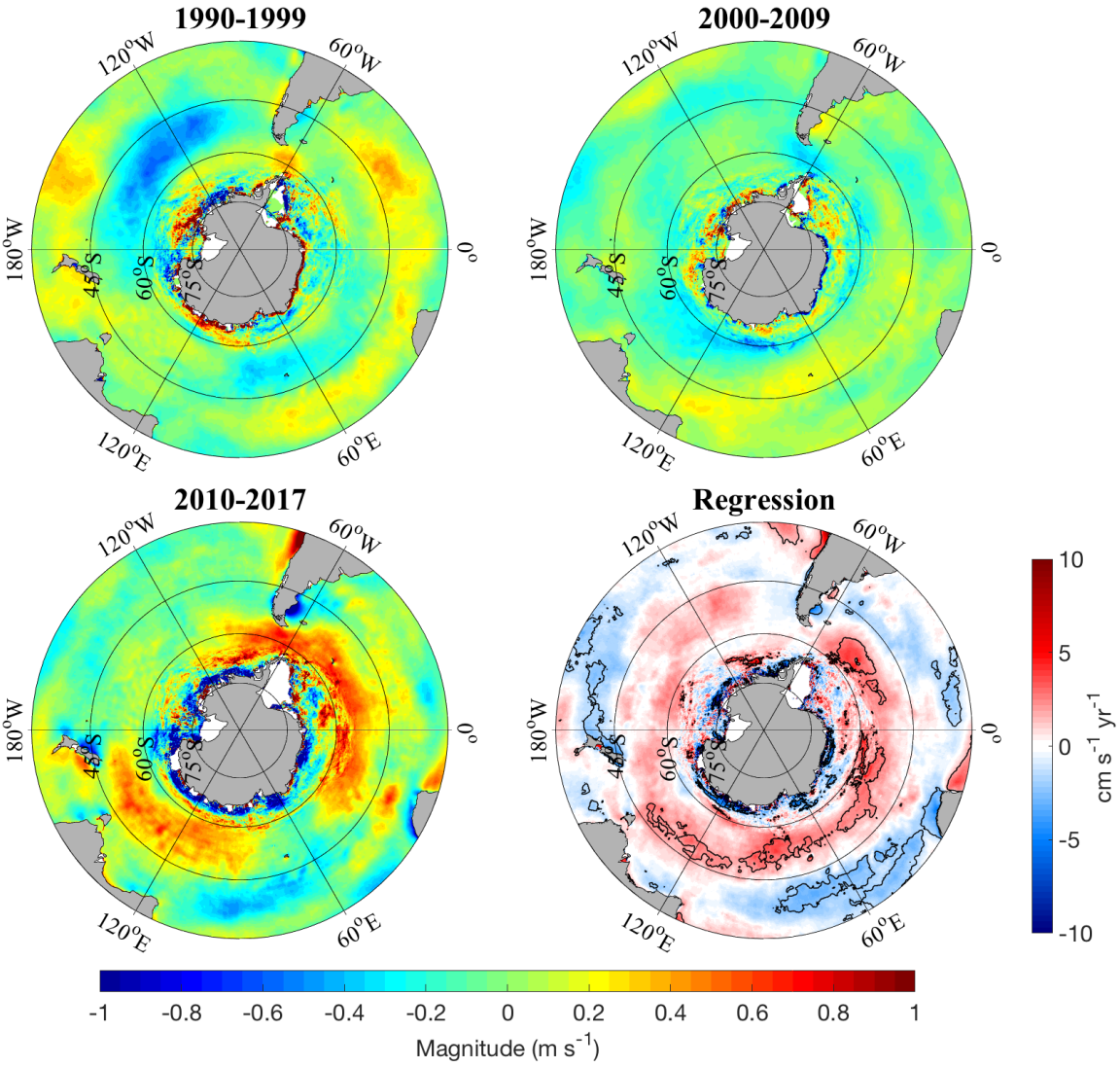

Figure 6.1. Mean decadal anomalies and robust regressions of the surface winds from 1988 to 2016. Trends significantly different from zero are contoured in black. © 2018 IEEE

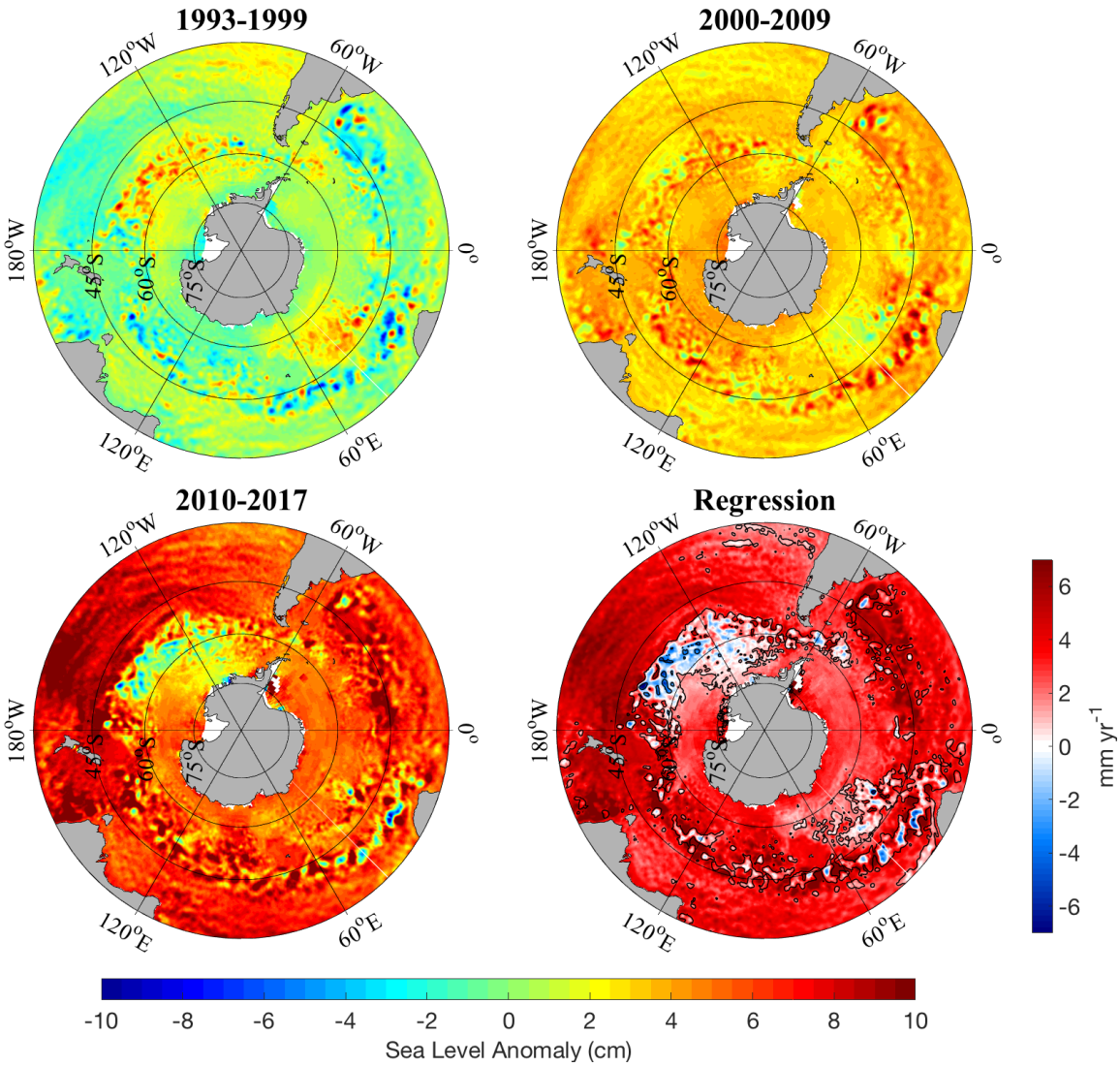

Figure 6.2. Decadal mean and robust regression of sea level anomalies (SLAs) from 1993 through 2017. Trends significantly different from zero are contoured in black. © 2018 IEEE

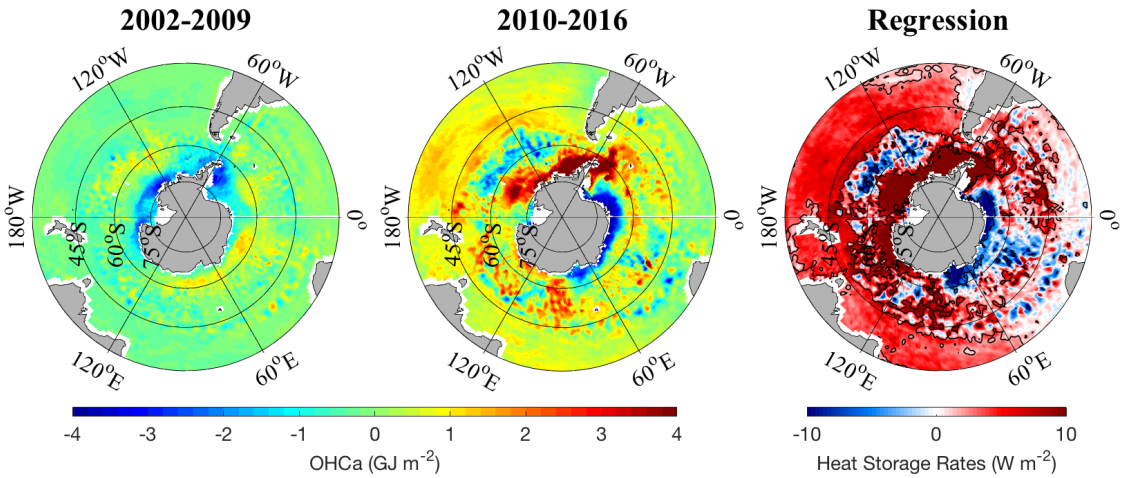

Figure 6.3. Decadal mean ocean heat content (OHC) anomalies and robust regressions of ocean heat storage rates from 2002 to 2016. Trends significantly different from zero are contoured in black. © 2018 IEEE

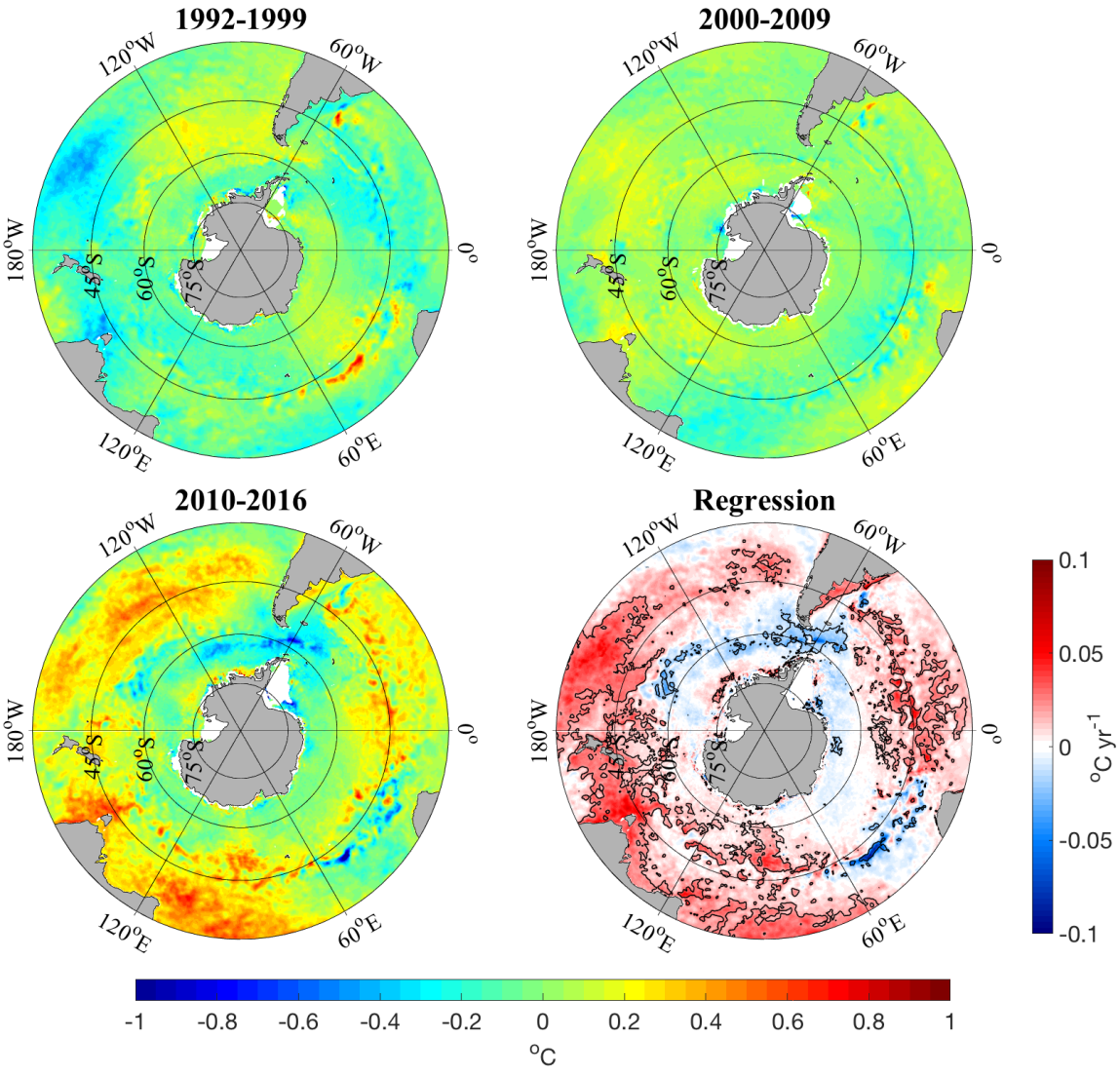

Figure 6.4. Decadal mean sea surface temperature (SST) anomalies and robust regressions from 1991 to 2016. Trends significantly different from zero are contoured in black. © 2018 IEEE

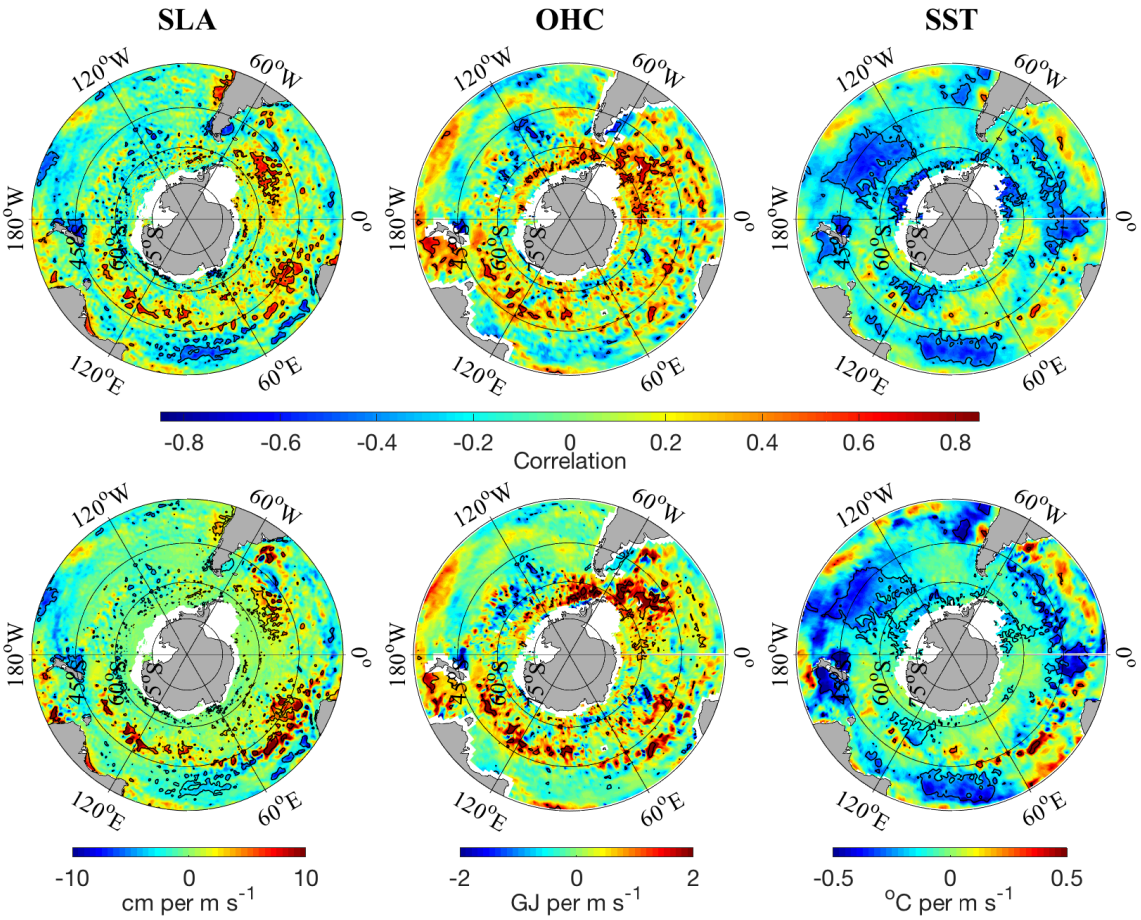

Figure 6.5. Pearson's correlation coefficients and robust regressions between surface wind anomalies and SLA, OHC, and SST anomalies. The comparisons of SLA are between 1993 and 2017, OHC between 2002 and 2016, and SST from 1992 through 2016. Positive (red) values indicate a positive relationship between surface wind anomalies and the variables.

CHAPTER 7

CONCLUSIONS

Five topics of SO dynamics and surface properties have been addressed throughout this dissertation: a comparison of SSS, variability in volume transports, the location of the PF, large-scale variability from atmospheric teleconnections, and recent changes in the SO physical properties.

Satellite-derived salinity is a relatively new advancement for the scientific community, with three satellites estimating SSS since 2010. Although methods of capturing brightness temperature are similar between the satellites, swath width, resolution, and methods of deriving salinity differ, which results in product differences outside of the errors associated with low temperatures, strong winds and currents, and land contamination. Despite all these difficulties, the various satellites estimate SSS throughout much of the SO with differences lower than the satellite uncertainty, and similar results when compared to Argo. The results of Chapter 2 support the use of the satellite missions to monitor the SO with confidence, albeit the large differences poleward of the ACC and near the swift-moving western boundary currents. Although the spatial comparison of the products show minimal differences, the horizontal resolution and smoothing of the satellite products can create large bias in estimation of advective fluxes. The differences in zonal and meridional gradients for SSS are comparatively large along the ACC and boundary currents, estimating differences as large in magnitude as the monthly mean advective flux.

The large discrepancies between the gradients suggest results and analyses using the various satellite-derived SSS could significantly differ based on the product smoothing, despite having small differences in the surface salinity. These results support the need to further improve the methods of deriving SSS from satellites in the high latitude regions, as small biases in the process could lead to large errors in the estimation of the freshwater flux and global water cycle.

The overturning and ACC transports in the SO have been heavily examined through observational and inverse models, but the patterns of variability and trends have not been analyzed. The new and exciting results in Chapter 3 suggest for the first time that there is not a change in the net meridional transports, but rather significant trends in the overturning circulation. Using ECCO v4r3, the meridional transports in the bottom cell of the Atlantic MOC are shown to be increasing; that is, there bottom waters are increasing equatorward and the deep waters are increasing southward transports at 30 °S. Contradictorily, the volume transports of the Indian and Pacific bottom overturning cells are decreasing. The zonal ACC transport trends are not significant, indicating net basin exchange is not changing despite increasing and poleward shifting westerlies. Analyzing the volume transports were the initial stride into estimating mass and heat budgets. Zonal and meridional salt transports are not significantly changing throughout the 24-year period, but the meridional heat transports are significantly increasing. Mainly driven by the Indian Ocean basin, there is a net heat flux into the surface and deep waters of the SO, contributing to the increased heat budget. These results are significant for climate science, but do come with limitations. ECCO incorporates observational data, but there are still large sampling gaps, spatially and temporally, in the deep and bottom waters. Additionally, the model-

physics in ECCO include eddy parameterizations, but does not include eddy-permitting resolution.

Although the transports of the ACC are shown to not be significantly increasing, previous studies show large disagreement between the methods to derive and the location of the PF. Using ECCO, methods of SST-gradients and SSH are compared to analyze the variability in the PF throughout Chapter 4. The SSH approach indicates the PF in all the Atlantic, Indian, and Pacific basins is shifting poleward, but is biased due to the increasing trend in sea level. The SST-approach however indicates the PF in the Pacific is shifting equatorward, while the Atlantic and Indian basins are within the natural variability. The analyses improve upon previous results by comparing both methods' inter- and intraseasonal variability with temperature and salinity. The PF location is highly correlated to temperature and salinity profiles within the surface 1000 m of the SO, as the PF represents the surface outcropping of the sloping isopycnals. Moreover, both methods indicate the PF is weakly driven by the AAO and Southern Oscillation, especially in the Pacific basin. However, the low correlation coefficients and coefficients of determination suggest the variability of the PF is largely driven outside of seasonal changes, the AAO, and Southern Oscillation. Chapter 4 concludes that the SST approach is the ideal method for monitoring the long-term position of the ACC, but both techniques derive similar results with subsurface variability and relationships to the large-scale teleconnections. The results are essential to modern biogeochemical studies, as the fronts and jets associated with the ACC are strong indicators for silicate, carbonate, and other key components to biological activity.

The large-scale atmospheric teleconnections of the AAO and Southern Oscillation are further examined in Chapter 5 for their respective influences on local SST. Since many previous studies employ models or temporally sparse observations, this chapter serves to confirm the relationship of teleconnections with nearly 35-years' worth of satellite-derived SST. In both instances, the SST variability was significantly related to the Antarctic and Southern Oscillations on monthly and yearly scales. Moreover, on longer timescales and throughout the austral summer, both teleconnections are driving changes in the SSTs. In times of in-phase oscillations, the teleconnections are contributing to the surface warming throughout the mid-latitudes and cooling along the Antarctic coast. The results of Chapter 5 emphasize the importance of monitoring the large-scale variability of ENSO, as the strongest relationships in the SO SST exist with the Southern Oscillation. This teleconnection is significantly contributing to the decreasing temperatures in the central South Pacific as majority of the SO is increasing surface temperatures.

The final chapter compared multiple satellite-derived variables for long-term trends and the relationship to variability with the surface winds. Many studies have explored individual parameters using satellites and model simulations, but none have analyzed the SO sea level, OHC, and SST for over 30 years investigating the role of surface winds on variability. The westerlies have previously been thought to be increasing in magnitude, where through satellite-derived methods, is shown to further be driving changes in surface and subsurface dynamics. The negative relationship with SST could be driven throughout evaporative cooling or surface transports of cooler waters, but the increased sea level and OHC suggest strong agreements. The increasing winds are increasing the storage of heat throughout the ocean column and are therefore driving changes in the sea level. The

increased mixing related to winds is therefore not only important to studying heat content and sea level changes, but could further drive changes of surface organic carbon nutrients, carbon dioxide and oxygen exchange, and the location of key silicate fronts in the SO.

This dissertation has addressed several important contributions from remote sensing to analyze the SO and dynamic changes throughout the last few decades. The need to further correct biases in the high latitudes is stressed, as estimates of mean salinity have greatly improved but have consequently increased the horizontal gradients. Increased ship-, glider, mooring, and Argo-based observations would greatly improve the validation and methodology required to more accurately and precisely depict SSS and other satellite-derived variables. Moreover, increased observations in the high-latitudes and bottom waters would significantly improve the outputs of state-estimate products and increase the temporal scales in which analyses can be investigated. Although these chapters investigated the most recent decades, improving the spatio-temporal aspect of observations and satellites would significantly improve our understanding of current climate changes. Long-term coupled climate models used to estimate potential future scenarios are additionally derived from a steady-state and observations of the recent decades, where improving our knowledge on the current dynamics and air-sea relationships would greatly improve the ability to predict potential climate outcomes. Future studies in the SO should focus on the heat storage along the sea ice extent and variability as a result of eddy-interactions. Many biases in models arise from differences in eddy-dynamics (i.e. resolution, parameters, atmospheric forcings), resulting in significantly different results within heat content, the overturning circulation, and air-sea exchanges. To conclude, these

chapters stressed the importance of future studies utilizing the high spatial and temporal resolutions of satellite-derived variables and the recent circulation patterns within the SO.

REFERENCES

Beal, L.M. & Elipot, S. (2016), Broadening not strengthening of the Agulhas Current since the early 1990s, Nature, 540(7634), 570, doi:10.1038/ngeo19853.

Belkin, I. M., & Gordon, A. L. (1996), Southern Ocean fronts from the Greenwich meridian to Tasmania. J. Geophys. Res. Oceans, 101(C2), 3675-3696, doi:10.1029/95JC02750.

Bishop, S.P., Gent, P.R., Bryan, F.O., Thompson, A.F., Long, M.C. & Abernathey, R., (2016), Southern Ocean overturning compensation in an eddy-resolving climate simulation. J. Phys. Oceanogr, 46(5), 1575-1592, doi:10.1175/JPO-D-15-0177.1

Böning, C. W., Dispert, A., Visbeck, M., Rintoul, S. R. & Schwarzkopf, F. U. (2008), The response of the Antarctic Circumpolar Current to recent climate change, Nat. Geosci., 1, 864–869, doi:10.1038/ngeo362.

Boutin, J., et al. (2015), Satellite and In-situ Salinity: Understanding Near–Surface Stratification and Subfootprint Variability. Bull. Amer. Meteor. Soc., 97, 1391–1407, doi:0.1175/BAMS–D–15–00032.1.

Boutin, J., Martin, N., Yin, X., Font, J., Reul, N. & Spurgeon, P. (2012), First Assessment of SMOS Data Over Open Ocean: Part II—Sea Surface Salinity. IEEE Trans. Geosci. Remote Sens, 50(5), 1662–1675, doi:10.1109/TGRS.2012.2184546.

Boutin, J., Martin, N., Reberdin, G., Yin, X. & Gaillard, F. (2013), Sea surface freshening inferred from SMOS and ARGO salinity: impact of rain. Ocean Sci., 9, 183–192, doi:10.5194/os–9–183–2013.

Brasnett, B. (2008), The impact of satellite retrievals in a global sea–surface–temperature analysis. Q.J.R. Meteorol. Soc., 134, 1745–1760. doi:10.1002/qj.319.

Cabanes, C., Lee, T. & Fu, L.L. (2008), Mechanisms of interannual variations of the meridional overturning circulation of the North Atlantic Ocean. J. Phys. Oceanogr., 38(2), 467-480, doi:10.1175/2007JPO3726.1.

Cai, W., Whetton, P.H., Karoly, D.J. (2003) The response of the Antarctic Oscillation to increasing and stabilized atmospheric CO2. J. Clim., 16, 1525–1538, doi:10.1175/1520-0442-16.10.1525.

Canada Meteorological Center (2012), GHRSST Level 4 CMC0.2deg Global Foundation Sea Surface Temperature Analysis (GDS version 2). Ver. 2.0. PO.DAAC, CA, USA. doi:10.5067/GHCMC–4FM02.

Cazenave, A., Dieng, H. B., Meyssignac, B., Von Schuckmann, K., Decharme, B., & Berthier, E. (2014). The rate of sea-level rise. Nature Climate Change, 4(5), 358, doi:10.1038/nclimate2159.

Cerrone, D., Fusco, G., Simmonds, I., Aulicino, G. Budillon, G. (2017), Dominant Covarying Climate Signals in the Southern Ocean and Antarctic Sea Ice Influence during the Last Three Decades. J. Clim., 30, 3055–3072, doi:10.1175/JCLI-D-16-0439.1.

Chambers, D.P. (2012), GRACE MONTHLY OCEAN MASS GRIDS NETCDF RELEASE 5.0. Ver. 5.0. PO.DAAC, CA, USA., doi:10.5067/TEOCN–0N005.

Chambers, D.P. & Bonin, J.A. (2012), Evaluation of Release 05 time–variable gravity coefficients over the ocean. Ocean Science, 8, 859–868, www.ocean–sci.net/8/859/2012.

Chambers, D.P. & Willis, J. K. (2010), A Global Evaluation of Ocean Bottom Pressure from GRACE, OMCT, and Steric–Corrected Altimetry. J. of Oceanic and Atmosph. Technology, 27, 1395–1402, doi:10.1175/2010JTECHO738.1.

Chambers, D. P., Tapley, B. D., & Stewart, R. H., (1997), Long-period ocean heat storage rates and basin-scale heat fluxes from TOPEX. Journal of Geophysical Research: Oceans, 102(C5), 10525–10533, doi:10.1029/96JC03644.

Chapman, C. C. (2017), New perspectives on frontal variability in the Southern Ocean. J. Phys. Oceanogr., 47(5), 1151-1168, doi:10.1175/JPO-D-16-0222.1.

Cheng, L., Trenberth, K. E., Fasullo, J., Boyer, T., Abraham, J., & Zhu, J. (2017). Improved estimates of ocean heat content from 1960 to 2015. Science Advances, 3(3), e1601545, doi:10.1126/sciadv.1601545.

Church, J. A., et al., in Climate Change (2013), The Physical Science Basis. Contribution of Working Group I to the Fifth Assessment Report of the Intergovernmental Panel on Climate Change, T. F. Stocker, D. Qin, G.-K. Plattner, M. Tignor, S. K. Allen, J. Boschung, A. Nauels, Y. Xia, V. Bex, P. M. Midgley, Eds. (Cambridge Univ. Press, 2013).

Ciasto, L.M., Alexander, M.A.; Deser, C., & England, M.H. (2011), On the persistence of cold-season SST anomalies associated with the Annular Mode. J. Clim., 24, 2500–2515, doi:10.1175/2010JCLI3535.1.

Ciasto, L.M. & Thompson, D.W. (2008), Observations of large-scale ocean-atmosphere interaction in the Southern Hemisphere. J. Clim., 21, 1244–1259, doi:10.1175/2007JCLI1809.1.

Cook, R. D. (1977), Detection of Influential Observation in Linear Regression. Technometrics, 19(1), 15-18, doi:10.1080/00401706.1977.10489493.

Cunningham, S. A., Alderson, S. G., King, B. A. & Brandon, M. A. (2003), Transport and variability of the Antarctic Circumpolar Current in the Drake Passage, J. Geophys. Res., 108, 8084, doi:10.1029/2001JC001147.

Dee et al. (2011), The ERA-Interim reanalysis: configuration and performance of the data assimilation system. Q.J.R. Meteorol. Soc., 137(656), 553-597, doi:10.1002/qj.828.

Dinnat, E. P., Boutin, J., Yin, X, Le Vine, D. M. (2014), Inter–comparison of SMOS and Aquarius Sea Surface Salinity: Effects of the dielectric constant and vicarious calibration, IEEE Microrad., 55–60, 14528317, doi:10.1109/MicroRad.2014.6878907.

Dong, S., Gille, S.T., Sprintall, J. (2007) An Assessment of the Southern Ocean Mixed Layer Heat Budget. J. Clim. 20, 4425-4442, doi:10.1175/JCLI4259.1.

Dong, S., Sprintall, J., & Gille, S. T. (2006), Location of the Antarctic Polar Front from AMSR-E Satellite Sea Surface Temperature Measurements. J. Phys. Oceanogr., 36, 2075-2089, doi:10.1175/JPO2973.1.

Donohue, K. A., Tracey, K. L., Watts, D. R., Chidichimo, M. P. & Chereskin, T. K. (2016), Mean Antarctic Circumpolar Current transport measured in Drake Passage, Geophys. Res. Lett., 43, 11, 760–11, 767, doi:10.1002/2016GL070319.

Downes, S. M., Budnick, A. S., Sarmiento, J. L., & Farneti, R. (2011). Impacts of wind stress on the Antarctic Circumpolar Current fronts and associated subduction. Geophysical Research Letters, 38(11), doi:10.1029/2011GL047668.

Drucker, R. & Riser, S. C. (2014), Validation of Aquarius sea surface salinity with Argo: analysis of error due to depth of measurement and vertical salinity stratification. J. Geophys. Res. Oceans, 119, 4626–4637, doi:10.1002/2014JC010045.

Durack, P. J. & Wijffels, S.E. (2010), Fifty-year trends in global ocean salinities and their relationship to broad-scale warming, J. Clim., 23, 4342–4362, doi:10.1175/2010JCLI3377.1.

Durbin, J. & Watson, G. S. (1950), Testing for serial correlation in least squares regression: I. Biometrika, 37(3/4), 409-428, doi:10.2307/2332391.

Dytham, C. (2011), Choosing and Using Statistics: A Biologist's Guide (3rd ed.). Wiley-Blackwell, Malden, MA (ISBN 978-1-4051-9839-4).

The ECCO Consortium (M. Buckley, J.-M. Campin A. Chaudhuri, I. Fenty, G. Forget, I. Fukumori, P. Heimbach, C. Hill, C.King, X. Liang, A. Nguyen, C. Piecuch, R. Ponte, K. Quinn, M. Sonnewald, D. Spiegel, N. Vinogradova, O. Wang, C. Wunsch) (2017a), A Twenty-Year Dynamical Oceanic Climatology: 1994-2013. Part 1: Active Scalar Fields: Temperature, Salinity, Dynamic Topography, Mixed-Layer Depth, Bottom Pressure. The ECCO Consortium, 1.2, http://hdl.handle.net/1721.1/107613.

The ECCO Consortium (M. Buckley, J.-M. Campin A. Chaudhuri, I. Fenty, G. Forget, I. Fukumori, P. Heimbach, C. Hill, C.King, X. Liang, A. Nguyen, C. Piecuch, R. Ponte, K. Quinn, M. Sonnewald, D. Spiegel, N. Vinogradova, O. Wang, C. Wunsch) (2017b), A Twenty-Year Dynamical Oceanic Climatology: 1994-2013. Part 2: Velocities, Property Transports, Meteorological Variables, Mixing Coefficients. The ECCO Consortium, 1.3, http://hdl.handle.net/1721.1/109847.

Farneti, R., Downes, S. M., Griffies, S. M., et al. (2015), An assessment of Antarctic Circumpolar Current and Southern Ocean meridional overturning circulation during 1958–2007 in a suite of interannual CORE-II simulations, Ocean Modelling, 93, 84-120, doi:10.1016/j.ocemod.2015.07.009.

Ferster, B.S., Subrahmanyam, B. & Macdonald, A. M. (2018), Confirmation of ENSO-Southern Ocean Teleconnections using Satellite Derived SST, Remote Sens., 10, 331; doi:10.3390/rs10020331.

Fogt, R.L. & Bromwich, D. H. (2006), Decadal variability of the ENSO teleconnection to the high-latitude South Pacific governed by coupling with the southern annular mode. J. Clim., 19, 979–997, doi:10.1175/JCLI3671.1.

Forget, G., Campin, J. M., Heimbach, P., Hill, C. N., Ponte, R. M. & Wunsch, C. (2015), ECCO version 4: an integrated framework for non-linear inverse modeling and global ocean state estimation, Geosci. Model Dev., 8(10), 3071-3104, doi:10.5194/gmd-8-3071-2015.

Forget, G., Campin, J.-M., Heimbach, P., Hill, C. N., Ponte, R. M. & Wunsch, C. (2016), ECCO version 4: Second Release, http://hdl.handle.net/1721.1/102062

Freeman, N. M. & Lovenduski, N. S. (2016a), Mapping the Antarctic Polar Front: weekly realizations from 2002 to 2014. Earth System Science Data, 8(1), 191-198, doi:10.5194/essd-8-191-2016.

Freeman, N. M. & Lovenduski, N. S. (2016b), Mapping the Antarctic Polar Front: Weekly realizations from 2002 to 2014, links to NetCDF file and MPEG4 movie. PANGAEA, https://doi.org/10.1594/PANGAEA.855640.

Freeman, N. M., Lovenduski, N. S. & Gent, P. R. (2016), Temporal variability in the Antarctic polar front (2002–2014). J. Geophys. Res. Oceans, 121(10), 7263-7276, doi:10.1002/2016JC012145.

Fukumori, I., Wang, O., Fenty, I., Forget, G., Heimbach, P., & Ponte, R. M. (2017), ECCO Version 4 Release 3, JPL/NASA, ftp://ecco.jpl.nasa.gov/Version4/Release3/doc/v4r3_summary.pdf.

Ganachaud, A., & Wunsch, C. (2000), Improved estimates of global ocean circulation, heat transport, and mixing from hydrographic data, Nature, 408, 453-457, doi:10.1038/35044048.

Ganachaud, A., Wunsch, C., Marotzke, J. & Toole, J. (2000), Meridional overturning and large scale circulation of the Indian Ocean, J. Geophys. Res., 105(C11), 26117–26134, doi:10.1029/2000JC900122.

Gille, S. T. (2002), Warming of the Southern Ocean Since the 1950's, Science, 295, 1275–1277, doi:10.1126/science.1065863.

Gille, S. T. (2008), Decadal-scale temperature trends in the Southern Hemisphere ocean. J. Clim., 21(18), 4749-4765, doi:10.1175/2008JCLI2131.1.

Gille, S. T. (2014), Meridional displacement of the Antarctic Circumpolar Current. Phil. Trans. R. Soc. A, 372(2019), 20130273, doi:10.1098/rsta.2013.0273.

Hackert, E., Busalacchi, A. J., Ballabrera–Poy, J. (2014), Impact of Aquarius sea surface salinity observations on coupled forecasts for the tropical Indo–Pacific Ocean, J. Geophys. Res. Oceans, 119, 4045–4067, doi:10.1002/2013JC009697.

Hallberg, R., & Gnanadesikan, A. (2006), The role of eddies in determining the structure and response of the wind-driven Southern Hemisphere overturning: Results from

the Modeling Eddies in the Southern Ocean (MESO) project. Journal of Physical Oceanography, 36(12), 2232-2252, doi:10.1175/JPO2980.1.

Hall, A., & Visbeck, M. (2002), Synchronous variability in the Southern Hemisphere atmosphere, sea ice, and ocean resulting from the annular mode, J. Climate, 15, 3043–3057, doi:10.1175/1520-0442(2002)015<3043:SVITSH>2.0.CO;2.

Hendon, H.H., Lim E.-P., & Nguyen, H. (2014), Seasonal variations of subtropical precipitation associated with the Southern Annular Mode. J. Clim., 27, 3446–3460, doi:10.1175/JCLI-D-13-00550.1.

Hendon, H.H., Thompson, D.W.J., & Wheeler, M. (2006), Australian rainfall and surface temperature variations associated with the Southern Hemisphere Annular Mode. J. Clim., 20, 2452–2467, doi:10.1175/JCLI4134.1.

Hogg, A. McC., Meredith, M. P. Chambers, D. P., Abrahamsen, E. P., Hughes, C. W. & Morrison, A. K. (2015), Recent trends in the Southern Ocean eddy field, J. Geophys. Res. Oceans, 120, 257-267, doi:10.1002/2014JC010470.

Jackett, D. R., & McDougall, T. J. (1997) A Neutral Density Variable for the World's Oceans. J. Phys. Oceanogr., 27, 237–263, doi:10.1175/1520-0485(1997)0272.0.CO;2

Jayne, S. R., Wahr, J. M., & Bryan, F. O. (2003). Observing ocean heat content using satellite gravity and altimetry. Journal of Geophysical Research: Oceans, 108(C2), doi: 10.1029/2002JC001619.

Johnson, E. S., Lagerloef, G. S., Gunn, J. T., Bonjean, F. (2002), Surface salinity advection in the tropical oceans compared with atmospheric freshwater forcing: A trial balance. J. Geophys. Res. Oceans., 107(C12), doi:10.1029/2001JC001122.

Kalnay, E., et al. (1996), The NCEP/NCAR 40-Year Reanalysis Project. Bull. Am. Meteorol. Soc., 77, 437–471, doi:10.1175/1520-0477(1996)077<0437:TNYRP>2.0.CO;2.

Kao, H.–Y., Lagerloef, G., T., Lee, T., Melnichenko, O., & Hacker, P. (2017), Aquarius Salinity Validation Analysis, Data Version 5.0. Aquarius Science Team Technology Document, http://podaac.jpl.nasa.gov/aquarius.

Kim, Y. S., & Orsi, A. H. (2014), On the variability of Antarctic Circumpolar Current fronts inferred from 1992–2011 altimetry. J. Phys. Oceanogr., 44(12), 3054-3071, doi:10.1175/JPO-D-13-0217.1.

Köhl, A., Martins, M. S., & Stammer, D. (2014), Impact of assimilating surface salinity from SMOS on ocean circulation estimates, J. Geophys. Res. Oceans, 119, 5449–5464, doi:10.1002/2014JC010040.

Kwok, R., Comiso, J. C., Lee, T., & Holland, P. R. (2016). Linked trends in the South Pacific sea ice edge and Southern Oscillation Index. Geophysical Research Letters, 43(19), 10-295, doi:10.1002/2016GL070655.

Lagerloef, G., Kao, H.–Y., Meissner, T., Vazquez, J. (2015), Aquarius Salinity Validation Analysis, Data Version 4.0. Aquarius Science Team Technology Document, http://podaac.jpl.nasa.gov/aquarius.

Landschützer, P., Gruber, N., Haumann, F. A., Rödenbeck, C., Bakker, D. C., Van Heuven, S., et al. (2015). The reinvigoration of the Southern Ocean carbon sink. Science, 349(6253), 1221-1224, doi:10.1126/science.aab2620.

Le Vine, D. M., Dinnat, E. P., Meissner, T., Yueh, S. H., Wentz, F. J., Torrusio, S. E & Lagerloef, G. (2015), Status of Aquarius/SAC–D and Aquarius Salinity Retrievals.

IEEE Journal of Selected Topics in Applied Earth Observations and Remote Sensing, 8(12), 5401–5415, doi:10.1109/JSTARS.2015.2427159.

Lee, T. (2016) Consistency of Aquarius sea surface salinity with Argo products on various spatial and temporal scales. Geophys. Res. Lett., 43(8), 3857–3864, doi:10.1002/2016GL068822.

Lee, M.M. & Coward, A. (2003), Eddy mass transport for the Southern Ocean in an eddy-permitting global ocean model. Ocean Modelling, 5(3), 249-266, doi:10.1016/S1463-5003(02)00044-6.

Lenton, A., & Matear, R. J. (2007), Role of the southern annular mode (SAM) in Southern Ocean CO2 uptake. Global Biogeochemical Cycles, 21(2), doi: 10.1029/2006GB002714.

Levitus, S., R. Burgett, & T. P. Boyer (1994), World Ocean Atlas 1994, vol. 3, Salinity, NOAA Atlas NESDIS 3, 111 pp., Natl. Oceanic and Atmos. Admin., Silver Spring, Md.

Lilliefors, H. W. (1967), On the Kolmogorov-Smirnov test for normality with mean and variance unknown. J. Amer. Statist. Assoc., 62(318), 399-402.

Liu, J., & Curry, J. A. (2010). Accelerated warming of the Southern Ocean and its impacts on the hydrological cycle and sea ice. Proceedings of the National Academy of Sciences, 107(34), 14987-14992, doi:10.1073/pnas.1003336107.

Losch, M., Menemenlis, D., Campin, J.-M., Heimbach, P., & Hill, C. (2010), On the formulation of sea-ice models. Part 1: Effects of different solver implementations and parameterizations. Ocean Modelling, 33(1), 129-144, doi:10.1016/j.ocemod.2009.12.008.

Lovenduski, N. S., & Gruber, N. (2005), Impact of the Southern Annular Mode on Southern Ocean circulation and biology. Geophysical Research Letters, 32(11), doi:10.1029/2005GL022727.

Lumpkin, R. & Speer, K. (2007), Global ocean meridional overturning. J. Phys. Oceanogr, 37(10), 2550-2562, doi:10.1175/JPO3130.1.

Lyman, J.M. & Johnson, G.C. (2008), Estimating annual global upper-ocean heat content anomalies despite irregular in situ ocean sampling. J. Clim., 21, 5629–5641, doi:10.1175/2008JCLI2259.1.

Lyman, J. M., & Johnson, G. C. (2014). Estimating global ocean heat content changes in the upper 1800 m since 1950 and the influence of climatology choice. Journal of Climate, 27(5), 1945-1957, doi:10.1175/JCLI–D–12–00752.1.

MacDonald, A. M., & Wunsch, C. (1996), An estimate of global ocean circulation and heat fluxes, Nature, 382, 436-439, doi:10.1038/382436a0.

Marshall, G. J. (2003), Trends in the Southern Annular Mode from observations and reanalyses, J. of Climate, 16(24) 4134-4143, doi:10.1175/1520-0442(2003)016<4134:TITSAM>2.0.CO;2.

Marshall, J. & Speer, K. (2012), Closure of the meridional overturning circulation through Southern Ocean upwelling, Nat. Geosci., 5, 171–180, doi:10.1038/ngeo1391.

Mazloff, M. R., Heimbach, P. & Wunsch, C. (2010), An Eddy-Permitting Southern Ocean State Estimate, J. Phys. Oceanogr., 40, 880–899, doi:10.1175/2009JPO4236.1.

Mazloff, M.R., Ferrari, R. & Schneider, T. (2013), The force balance of the Southern Ocean meridional overturning circulation. J. Phys. Oceanogr., 43(6), 1193-1208, doi:10.1175/JPO-D-12-069.1.

McNeil, B. I., & Matear, R. J. (2008). Southern Ocean acidification: A tipping point at 450-ppm atmospheric CO2. Proceedings of the National Academy of Sciences, 105(48), 18860-18864, doi:10.1073/pnas.0806318105.

Meissner, T. & Wentz, F. J. (2016), Remote Sensing Systems SMAP Ocean Surface Salinities [Level 2C, Level 3 Running 8–day, Level 3 Monthly], Version 2.0 validated release. Remote Sensing Systems, Santa Rosa, CA., USA. doi:10.5067/SMP20–3SMCS.

Meissner, T., Wentz, F. & Scott, J. (2015), Remote sensing systems SMAP Level 3 Ocean Surface Salinities [running 8–day, monthly] on 0.25 deg grid, version 1.0 (BETA). Technical report, Remote Sensing Systems, Santa Rosa, CA., USA. (http://www–remss.com/missions/smap).

Meredith, M. P. & Hogg, A. M. (2006), Circumpolar response of Southern Ocean eddy activity to a change in the Southern Annular Mode, Geophys. Res. Lett., 33, L16608, doi:10.1029/2006GL026499.

Meyer, A., Sloyan, B. M., Polzin, K. L., Phillips, H. E. & Bindoff, N. L. (2015), Mixing variability in the Southern Ocean. J. Phys. Oceanogr., 45(4), 966–987, doi:10.1175/JPO–D–14–0110.1.

Miller, R. L., Schmidt, G. A., & Shindell, D. T. (2006), Forced annular variations in the 20th century Intergovernmental Panel on Climate Change Fourth Assessment Report models, J. Geophys. Res., 111, D18101, doi:10.1029/2005JD006323.

Mitsudera, H., Miyama, T., Nishigaki, H., Nakanowatari, T., Nishikawa, H., Nakamura, T. Wagawa, T., Furue, R., Fujii, Y., & Ito, S. (2018), Low ocean-floor rises regulate

subpolar sea surface temperature by forming baroclinic jets. Nature communications, 9(1), 1190, http:doi.org/10.1038/s41467-018-03526-z.

Mo, K.C. (2000), Relationships between low-frequency variability in the Southern Hemisphere and sea surface temperature anomalies. J. Clim., 13, 3599–3610, doi:10.1175/1520-0442(2000)013<3599:RBLFVI>2.0.CO;2.

Montes-Hugo, M., Doney, S. C., Ducklow, H. W., Fraser, W., Martinson, D., Stammerjohn, S. E., & Schofield, O. (2009). Recent changes in phytoplankton communities associated with rapid regional climate change along the western Antarctic Peninsula. Science, 323(5920), 1470-1473, doi:10.1126/science.1164533.

Moon, J.–H. & Song, Y. T. (2014), Seasonal salinity stratifications in the near–surface layer from Aquarius, Argo, and an ocean model: Focusing on the tropical Atlantic/Indian Oceans, J. Geophys. Res. Oceans, 119, 6066–6077, doi:10.1002/2014JC009969.

Moore, J. K., Abbott, M. R., Richman, G., & Nelson, D. M. (2000), The Southern Ocean at the Last Glacial Maximum: A strong sink for atmospheric carbon dioxide, Global Biogeochem. Cycles, 14(1), 455–475, doi:10.1029/1999GB900051.

Naveira Garabato, A. C., Ferrari, R. & Polzin, K. L. (2011), Eddy stirring in the Southern Ocean. J. Geophys. Res. Oceans, 116, C09019, doi:10.1029/2010JC006818.

Nyadjro, E. S., Subrahmanyam, B. & Shriver, J. (2011), Seasonal variability of salt transport during the Indian Ocean monsoons, J. Geophys. Res., 116, C08036, doi:10.1029/2011JC006993.

Olmedo, E., Martínez, J., Umbert, M., Hoareau, N., Portabella, M., Ballabrera, J. & Turiel, A. (2016), Improving time and space resolution of SMOS salinity maps using multifractal fusion. Remote Sensing of Environment, 180, 246–263, doi:10.1016/j.rse.2016.02.038.

Orsi, A. H., Whitworth III, T. & Nowlin Jr, W. D. (1995), On the meridional extent and fronts of the Antarctic Circumpolar Current. Deep Sea Research Part I: Oceanographic Research Papers, 42(5), 641-673, doi:10.1016/0967-0637(95)00021-W.

Peng, G., Zhang, H. M., Frank, H. P., Bidlot, J. R., Higaki, M., Stevens, S., & Hankins, W. R. (2013). Evaluation of various surface wind products with OceanSITES buoy measurements. Weather and Forecasting, 28(6), 1281-1303, doi:10.1175/WAF–D–12–00086.1.

Piecuch, C. G. (2017), A Note on Practical Evaluation of Budgets in ECCO Version 4 Release 3, ftp://ecco.jpl.nasa.gov/Version4/Release3/doc/evaluating_budgets_in_eccov4r3.pdf

Purich, A., Cai, W., England, M. H., & Cowan, T. (2016), Evidence for link between modelled trends in Antarctic sea ice and underestimated westerly wind changes. Nature communications, 7, 10409.

Reager, J. T., Gardner, A. S., Famiglietti, J. S., Wiese, D. N., Eicker, A., & Lo, M. H. (2016), A decade of sea level rise slowed by climate-driven hydrology. Science, 351(6274), 699-703, doi:10.1126/science.aad8386.

Ren, L., Speer, K. & Chassignet, E. P. (2011), The mixed layer salinity budget and sea ice in the Southern Ocean. J. Geophys. Res., 116, C08031, doi:10.1029/2010JC006634.

Reul, N., Tenerelli, J., Boutin, J., Chapron, B., Paul, F., Brion, E., Gaillard, F. & Archer, O. (2012), Overview of the first SMOS sea surface salinity products. Part I: Quality assessment for the second half of 2010. IEEE Trans. Geosci. Remote Sens., 50(5), 1636–1647, doi:10.1109/LGRS.2012.2207943.

Reynolds, R.W., Smith, T.M., Liu, C., Chelton, D.B., Casey, K.S., & Schlax, M.G. (2007), Daily High-Resolution-Blended analyses for sea surface temperature. J. Clim., 20, 5473–5496, doi:10.1175/2007JCLI1824.1.

Roemmich, D., Church, J., Gilson, J., Monselesan, D., Sutton, P., & Wijffels, S. (2015), Unabated planetary warming and its ocean structure since 2006. Nature climate change, 5(3), 240.

Roemmich, D., Gilson, J., Davis, R., Sutton, P., Wijffels, S. & Riser, S. (2007), Decadal spinup of the South Pacific subtropical gyre, J. Phys. Oceanogr., 37(2), 162-173, doi:10.1175/JPO3004.1.

Roemmich, D., Gilson, J., Sutton, P. & Zilberman, N. (2016), Multidecadal change of the South Pacific gyre circulation, J. Phys. Oceanogr., 46(6), 1871-1883, doi:10.1175/JPO-D-15-0237.1.

Rintoul, S. R. & Naveira Garabato, A. C. (2013), Dynamics of the Southern Ocean Circulation, in: Siedler, G., Griffies, S. M., Gould, J, and Church, J. A. (Eds.), Ocean Circulation and Climate, Elsevier Ltd., 103, 471-492.

Rye, C. D., Garabato, A. C. N., Holland, P. R., Meredith, M. P., Nurser, A. G., Hughes, C. W., et al. (2014). Rapid sea-level rise along the Antarctic margins in response to increased glacial discharge. Nature Geoscience, 7(10), 732, doi:10.1038/ngeo2230.

Sabine, C. L., Feely, R. A., Gruber, N., Key, R. M., Lee, K., Bullister, J. L., et al. (2004), The oceanic sink for anthropogenic CO2. Science, 305(5682), 367-371, doi:10.1126/science.1097403.

Sallée, J. B., Speer, K. & Morrow, R. (2008), Response of the Antarctic Circumpolar Current to atmospheric variability. Journal of Climate, 21(12), 3020-3039, doi:10.1175/2007JCLI1702.1

Sarmiento, J. L., Hughes, T. M., Stouffer, R. J., & Manabe, S. (1998). Simulated response of the ocean carbon cycle to anthropogenic climate warming. Nature, 393(6682), 245, doi:10.1038/30455.

Sen, P. K. (1968), Estimates of the regression coefficient based on Kendall's tau. J. Amer. Statist. Assoc., 63(324), 1379-1389.

Sen Gupta, A., & England, M.H. (2006), Coupled ocean atmosphere-ice response to variations in the Southern Annular Mode, J. Climate, 19, 4457–4486, doi:10.1175/JCLI3843.1.

Sheen, K.L., Naveira Garabato, A.C., Brearley, J.A., Meredith, M.P., Polzin, K.L., Smeed, D.A., Forryan, A., King, B.A., Sallée, J.B., Laurent, L.S. & Thurnherr, A.M. (2014), Eddy–induced variability in Southern Ocean abyssal mixing on climatic timescales. Nature Geoscience, 7(8), 577–582, doi:10.1038/ngeo2200.

Simmonds, I. & King, J.C. (2004), Global and hemispheric climate variations affecting the Southern Ocean. Antarct. Science. 16, 401–413, doi:10.1017/S0954102004002226.

Sloyan, B. M. & Rintoul, S. R. (2001), Circulation, renewal, and modification of the Antarctic Mode and Intermediate Water, J. Phys. Oceanogr., 31, 1005-1030, doi:10.1175/1520-0485(2001)031<1005:CRAMOA>2.0.CO;2.

Sokolov, S. & Rintoul, S. R. (2009a), Circumpolar structure and distribution of the Antarctic Circumpolar Current fronts: 1. Mean circumpolar paths, J. Geophys. Res. Oceans., 114, C11018, doi:10.1029/2008JC005108.

Sokolov, S. & Rintoul, S. R. (2009b), Circumpolar structure and distribution of the Antarctic Circumpolar Current fronts: 2. Variability and relationship to sea surface height, J. Geophys. Res. Oceans, 114, C11018, doi:10.1029/2008JC005248.

Song, Y. T., Lee, T., Moon, J.–H., Qu, T. & Yueh, S. (2015), Modeling skin–layer salinity with an extended surface–salinity layer, J. Geophys. Res. Oceans, 120, 1079–1095, doi:10.1002/2014JC010346.

Sun, C. & Watts, D.R. (2002), Heat flux carried by the Antarctic Circumpolar Current mean flow. J. Geophys. Res., 107, doi:10.1029/2001JC001187.

Swart, N. C., Gille, S. T., Fyfe, J. C. & Gillett, N. P. (2018), Recent Southern Ocean warming and freshening driven by greenhouse gas emissions and ozone depletion. Nat. Geosci., 1, doi:10.1038/s41561-018-0226-1.

Stammer, D., Wunsch, C., Giering, R., et al. (2003), Volume, heat, and freshwater transports of the global ocean circulation 1993–2000, estimated from a general

circulation model constrained by World Ocean Circulation Experiment (WOCE) data, J. Geophys. Res., 108(C1), 3007, doi:10.1029/2001JC001115.

Talley, L.D. (2003), Shallow, intermediate, and deep overturning components of the global heat budget. J. Phys. Oceanogr., 33(3), 530-560, doi:10.1175/1520-0485(2003)033<0530:SIADOC>2.0.CO;2.

Talley, L. D. (2008), Freshwater transport estimates and the global overturning circulation: Shallow, deep and throughflow components. Progress in Oceanography, 78(4), 257–303, doi:10.1016/j.pocean.2008.05.001.

Talley, L.D. (2013), Closure of the global overturning circulation through the Indian, Pacific, and Southern Oceans: Schematics and transports, Oceanography, 26(1), 80–97, doi:10.5670/oceanog.2013.07.

Talley, L.D., Feely, R.A., Sloyan, B.M., Wanninkhof, R., Baringer, M.O., Bullister, J.L., Carlson, C.A., Doney, S.C., Fine, R.A., Firing, E., et al. (2016), Changes in Ocean Heat, Carbon Content, and Ventilation: A Review of the First Decade of GO-SHIP Global Repeat Hydrography. Annu. Rev. Mar. Sci., 8, 185–215, doi:10.1146/annurev-marine-052915-100829.

Trenberth, K.E. & Caron, J. M. (2000), The Southern Oscillation revisited: Sea level pressures, surface temperatures, and precipitation. J. Clim., 13, 4358–4365, doi:10.1175/1520-0442(2000)013<4358:TSORSL>2.0.CO;2.

Thompson, A. F. (2010), Jet formation and evolution in baroclinic turbulence with simple topography, J. Phys. Oceanogr., 40(2), 257–278, doi:10.1175/2009JPO4218.1.

Thompson, D. W. J. & Solomon, S. (2002), Interpretation of Recent Southern Hemisphere Climate Change. Science, 296(5569), 895-899, doi:10.1126/science.1069270.

Thompson, D. W. J., Solomon, S., Kushner, P. J., England, M. H., Grise, K. M., Karoly, D. J. (2011), Signatures of the Antarctic ozone hole in Southern Hemisphere surface climate change. Nature Geosci. 4, 741-749, doi:10.1038/ngeo1296.

Thompson, D. W., & Wallace, J. M. (2000). Annular modes in the extratropical circulation. Part I: Month-to-month variability. J. Clim., 13(5), 1000-1016, doi:10.1175/1520-0442(2000)013<1000:AMITEC>2.0.CO;2.

Toggweiler, J. R., & Samuels, B. L. (1995), Effect of sea ice on the salinity of Antarctic bottom waters, J. Phys. Oceanogr., 25, 1980-1997, doi:10.1175/15200485(1995)025<1980:EOSIOT>2.0.CO;2.

Toyoda, T., Fujii, Y., Kuragano, T., Matthews, J. P., Abe, H., Ebuchi, N., Usui, N., Ogawa, K. & Kamachi, M. (2015), Improvements to a global ocean data assimilation system through the incorporation of Aquarius surface salinity data, Q. J. R. Meteorol. Soc., 141(692), 2750–2759, doi:10.1002/qj.2561.

Turner, J. (2004), The El Niño–Southern Oscillation and Antarctica. Int. J. Climatol., 24, 1–31, doi:10.1002/joc.965.

Verdy, A. & Mazloff, M. (2017), A data assimilating model for estimating Southern Ocean biogeochemistry. J. Geophys. Res. Oceans., 122, doi:10.1002/2016JC012650.

Vianna, M.L. & Menezes, V.V. (2011), Double-celled subtropical gyre in the South Atlantic Ocean: Means, trends, and interannual changes, J. Geophys. Res: Oceans, 116(C3), doi:10.1029/2010JC006574.

Vinogradova, N. T., Ponte, R. M., Fukumori, I. & Wang, O. (2014), Estimating satellite salinity errors for assimilation of Aquarius SMOS data into climate models, J. Geophys. Res. Oceans, 119, 4732–4744, doi:10.1002/2014JC009906.

Wang, Z., T. Kuhlbrodt, and M. P. Meredith, 2011: On the response of the Antarctic Circumpolar Current transport to climate change in coupled climate models, J. Geophys. Res., 116, C08011, http://doi.org/10.1029/2010JC006757.

Watson, G.S. (1967), Linear least squares regression. The Annals of Mathematical Statistics, 38(6), 1679-1699, doi:10.1214/aoms/1177698603.

Waugh, D. W., Primeau, F., DeVries, T. & Holzer, M. (2013), Recent Changes in the Ventilation of the Southern Oceans, Science, 339 (6119), 568-570, doi:10.1126science.1225411.

Welhouse, L.J., Lazzara, M. A., Keller, L. M., Tripoli, G. J., & Hitchman, M. H. (2016), Composite analysis of the effects of ENSO events on Antarctica. J. Clim., 29, 1797–1808, doi:10.1175/JCLI-D-15-0108.1.

Wentz, F. & Le Vine, D.M. (2012), Aquarius Salinity Retrieval Algorithm, ATBD. RSS Technical Report 082912, ftp://podaac–ftp.jpl.nasa.gov/allData/aquarius/docs.

Wentz, F., Ricciardulli, L., Gentemann, C., Meissner, T., Hilburn, K. A. & Scott, J. (2013), Remote Sensing Systems Coriolis WindSat [Daily] Environmental Suite on 0.25 deg grid, Version 7.0.1, [WSPD_LF]. RSS Technical Report 091316 19, Remote Sensing Systems, Santa Rosa, CA, USA. www.remss.com/missions/windsat.

Willis, J. K., Roemmich, D., & Cornuelle, B. (2004). Interannual variability in upper ocean heat content, temperature, and thermosteric expansion on global scales. J. Geophys. Res. Oceans, 109, C12, doi:10.1029/2003JC002260.

Wunsch, C. & Heimbach, P. (2009), The global zonally integrated ocean circulation, 1992–2006: Seasonal and decadal variability. J. Phys. Oceanogr., 39(2), 351-368, doi:10.1175/2008JPO42012.1.

Xiao, B., Zhang, Y., Yang, X.Q., & Nie, Y. (2016), On the role of extratropical air-sea interaction in the persistence of the Southern Annular Mode. Geophys. Res. Lett., 43, 8806–8814, doi:10.1002/2016GL070255.

Yin, X., Boutin, J., Martin, N., Spurgeon, P., Vergely, J.–L. & Gaillard, F. (2014), Errors in SMOS Sea Surface Salinity and their dependency on priori wind speed. Remote Sensing of Environment, 146, 159–171, doi:10.1016/j.rse.2013.09.008.

Yu, L. (2011), A global relationship between the ocean water cycle and near-surface salinity. J. Geophys. Res. Oceans, 116(C10), doi:10.1029/2010JC006937.

Zhang, H. M., Bates, J. J., & Reynolds, R. W. (2006), Assessment of composite global sampling: Sea surface wind speed. Geophysical Research Letters, 33(17), doi:10.1029/2006GL027086.

Zheng, Y. & Giese, B. S. (2009), Ocean heat transport in Simple Ocean Data Assimilation: Structure and mechanisms, J. Geophys. Res., 114, C11009, doi:10.1029/2008JC005190.

APPENDIX A

COPYRIGHT PERMISIONS

A.1 CHAPTER 2 COPYRIGHT PERMISIONS

Dear Brady,

Thank you for your email. As an author, you are welcome to reuse this content in other works created by yourself. We usually ask that authors get an official license, but this journal has not been added to our online system so we will grant you permission over email on this occasion.

Please accept this email as an official permission to reuse the article in a thesis/dissertation. Please note: we allow the use of the final accepted manuscript version of the article in the thesis/dissertation, not the published version.

The dissertation can be uploaded to the university repository/put in the university library and you can print up to 100 copies of the dissertation.

Best wishes,

Oda

Oda Siqveland

Permissions Assistant

SpringerNature

The Campus, 4 Crinan Street, London N1 9XW,

United Kingdom

T +44 (0) 207 014 6851

A.2 CHAPTER 3 COPYRIGHT PERMISIONS

Dear Mr. Ferster,

Thank you for your email. This signed message constitutes permission to use the material requested below.

You may use your article as part of your dissertation with the following conditions:

1. Include the complete bibliographic citation of the original source for each.

2. Include the following statement with that citation for each: © American Meteorological Society. Used with permission.

If you have any questions or need additional information, please let me know.

Best,

Andrea Herbst

Peer Review Support Associate

American Meteorological Society

617.226.3982

www.ametsoc.org

A.3 CHAPTER 5 COPYRIGHT PERMISIONS

Dear Dr. Ferster,

Thank you very much for your message. Since Remote Sensing is an open access Journal, you are free to re-use the published material in your PhD Dissertation if proper accreditation/citation of the original publication is given. The detailed information can be accessed at: http://www.mdpi.com/about/openaccess

Hope the above information helps.

Best regards,

Ms. Scarlett Min, Msc

Assistant Editor

E-Mail: scarlett.min@mdpi.com

http://www.mdpi.com/journal/remotesensing

A.4 CHAPTER 6 COPYRIGHT PERMISIONS

Dear Brady Ferster,

Your request has been forwarded to me for response. Please retain this mail for your records.

The IEEE does not require individuals working on a dissertation/thesis to obtain a formal reuse license however, you must follow the requirements listed below:

Textual Material

Using short quotes or referring to the work within these papers) users must give full credit to the original source (author, paper, publication) followed by the IEEE copyright line © [Year of publication] IEEE.

In the case of illustrations or tabular material, we require that the copyright line © [Year of original publication] IEEE appear prominently with each reprinted figure and/or table.

If a substantial portion of the original paper is to be used, and if you are not the senior author, also obtain the senior author's approval.

Full-Text Article

If you are using the entire IEEE copyright owned article, the following IEEE copyright/credit notice should be placed prominently in the references: © [year of original publication] IEEE. Reprinted, with permission, from [author names, paper title, IEEE publication title, and month/year of publication]

Only the accepted version of an IEEE copyrighted paper can be used when posting the paper or your thesis on-line. You may not use the final published version

In placing the thesis on the author's university website, please display the following message in a prominent place on the website: In reference to IEEE copyrighted material which is used with permission in this thesis, the IEEE does not endorse any of the University of South Carolina's products or services. Internal or personal use of this material is permitted. If interested in reprinting/republishing IEEE copyrighted material for advertising or promotional purposes or for creating new collective works for resale or redistribution, please go to

http://www.ieee.org/publications_standards/publications/rights/rights_link.html

to learn how to obtain a License from Rights Link.

If applicable, University Microfilms and/or ProQuest Library, or the Archives of Canada may supply single copies of the dissertation.

Good luck with your dissertation.

Best regards,

ME Brennan

Ms M.E. Brennan

IEEE

501 Hoes Lane

Piscataway, NJ 08854-4141 USA

me.brennan@ieee.org

+1 (732) 562-2660